

Detailed Report upon project completion

Printed Electrocatalyst layer for PEMFC/DMFC

Submitted to

ONGC Energy Centre Trust

by

Venugopal Santhanam

Associate Professor,

Department of Chemical Engineering

Indian Institute of Science

Bangalore 560 012



Executive Summary

Hydrogen is considered a fuel for the future, and fuel cells can use the chemical energy of the hydrogen to create electrical energy through the electrochemical pathway, leading to enhanced efficiency than the internal combustion route. The Oil and Gas industry faces a formidable task of meeting increasing energy demands while committing to significant reductions in gas emissions to combat global climate change. The most significant emitter of greenhouse gasses on offshore installations is gas turbines accounting for 81% of total greenhouse gas emissions. Fuel cells are being considered as potential alternatives for such off-grid power supply applications. A recently undertaken SWOT analysis of fuel cell technology finds it competitive with gas turbines in terms of efficiency, emission, maintenance and downtime. But significantly lagging in terms of cost[1]. Significant advances have been made in fuel cell system design over the last three decades concerning cost-reduction and structural design. But cost and durability problems associated with carbon support corrosion and loss of active surface area under PEMFC working conditions, especially during start-up or shut down cycles, have led to renewed interest in carbon-free nanostructured electrodes. In this context, there is scope for developing additive manufacturing processes, as well as novel electrocatalyst designs to further reduce platinum/PGM loading. *Our research aims to develop a cost-effective, additive process for manufacturing membrane electrode assemblies with ultralow platinum loading for low-temperature fuel cells.*

References:

- [1] C. B. Nyberg, “Fuel Cells in Offshore Oil and Gas Production,” NTNU, 2017.
- [2] S. K. Parmar and V. Santhanam, “In situ formation of silver nanowire networks on paper,” *Curr. Sci.*, vol. 107, no. 2, pp. 262–268, 2014, doi: 10.18520/cs/v107/i2/262-269.
- [3] Y. Liu, D. Gokcen, U. Bertocci, and T. P. Moffat, “Self-Terminating Growth of Platinum Films by Electrochemical Deposition,” *Science*, vol. 338, no. 6112, pp. 1327–1330, Dec. 2012, doi: 10.1126/science.1228925.
- [4] K. Agrawal, “Printed Electrodes for Poly Electrolyte Membrane Fuel Cell (PEMFC),” IISc Bangalore, 2018.

Table of Contents

Chapter 1.....	1
Introduction	1
1.1 Introduction	1
1.2 Polymer Electrolyte (or Proton Exchange) Membrane Fuel Cell.....	3
1.2.1 History of PEMFC.....	3
1.2.2 State of the art PEMFC design	4
1.3 Motivation	8
1.4 References:	10
Chapter 2.....	15
Literature Review.....	15
Chapter 3.....	25
Prudent Practices in Ex-Situ Durability Analysis for Platinum-based Electrocatalysts	25
3.1 Introduction	25
3.2 Durability analysis for electrocatalysts	27
3.3 Essentials of cyclic voltammetry	28
3.4 Effective practices during ex-situ durability analysis	36
3.4.1 Electrochemical setup and selection of electrodes	36
3.4.2 Cleaning/Pre-treatment protocols for electrochemical setup and electrodes	38
3.4.3. Electrolyte preparation	45
3.5 Analysis of Pt CV and calculation of ECSA.....	46
3.5.1 H_{upd} region (from ~ 0.05 V to $\sim 0.3-0.5$ V).....	48
3.5.2 Double layer charging (or capacitance) region	56
3.5.3 Pt surface oxidation and reduction ($> \sim 0.7-0.8$ V)	57
3.6 Precautions to be undertaken while conducting durability experiments ..	58
3.6.1 Importance of using a fresh electrolyte for each sample synthesis	58

3.6.2 Importance of a proper inert gas purging setup	59
3.7 Anticipated improvement in skillset	63
3.8 Summary and outlook	64
3.9 References	65
Chapter 4	77
The durability of Platinum Overlayers formed by Self-Terminating Electrodeposition	77
4.1 Introduction	77
4.2 Experimental	80
4.2.1 Synthesis of platinum atomic overlayers on gold (Au):.....	80
4.2.2 Platinum overlayer formation using STED.....	84
4.2.3 Ex-situ durability analysis of Pt overlayers on Au:	85
Chapter 5	97
Platinum atomic overlayer deposition on silver, gold and silver-gold alloy thin film 97	
5.1 Introduction	97
5.2 Experimental	97
5.2.1 Platinum deposition on e-beam evaporated silver.....	97
5.2.2 Platinum deposition on commercial gold and silver thin film	98
5.3 Summary	112
5.4 References	114
Chapter 6	115
Platinum atomic overlayer deposition on silver nanostructures	115
6.1 Introduction	115
6.2 Inkjet printing of silver nanostructures on Nafion membrane	117
6.2.1 Nafion membrane structure.....	117
6.2.2 Preparation of Nafion membrane substrate	118
6.2.3 Inkjet printing.....	119
6.3 Platinum overlayer deposition using STED on Ag nanowire.....	122
6.4 Summary	126

6.5 References:.....	127
Appendix A: Fuel Cell station operation.....	131
Appendix B: Inkjet printing of Ag nanowire network on plastic substrate with different bilayers of PEL coating:.....	141

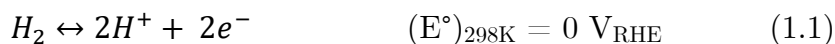
Chapter 1

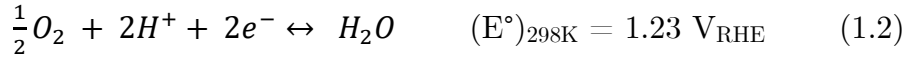
Introduction

1.1 Introduction

Hydrogen is the most abundant element in the universe and is considered a clean fuel for the future[1]. It can be produced from varieties of sources ranging from natural gas reforming to water electrolysis[2]. There are two ways energy can be generated from hydrogen; the first one is in the conventional combustion engine route, where hydrogen is burnt, and electrons are transferred at the molecular level by the collision between hydrogen and oxygen molecules. The combustion reaction is fast, in the matter of picoseconds, the hydrogen-hydrogen bonds and oxygen-oxygen bonds are broken and hydrogen-oxygen bonds are formed and therefore, the released energy can only be recovered in the form of heat. It must be converted to electrical power through mechanical energy conversion to produce electricity out of this. Going through these steps leads to inefficiency[3]. Contrary to this, in the electrochemical pathway, the potential energy of the electrons is extracted as they move from high-energy bonds to low-energy product bonds. Essentially the electrons that reconfigure in picoseconds at subatomic length scales in the combustion route are forced to reconfigure over greatly extended lengths by spatially separating the hydrogen and oxygen reactants.

In a fuel cell, hydrogen ‘combustion’ is split into two electrochemical half-cell reactions as equations 1.1 and 1.2





The spatial separation of the above reactions forces the electron transfer through an external circuit to complete the reaction, leading to an electric current. The spatial separation in the fuel cell happens by the electrolyte, which only allows the ions to flow, not electrons.

Fuel cells offer advantages over both combustion engines and batteries. Fuel Cells can directly convert chemical energy into electrical energy. They can be all solid state, with no moving part and silent operation. Various fuels can be used over a wide temperature range in fuel cells. If the required hydrogen for fuel cells is generated from renewable methods, it can significantly reduce NO_x, SO_x, and particulate emissions. Unlike batteries, fuel cells have independent scaling between power (determined by the fuel cell size) and capacity (determined by hydrogen storage size). Batteries often have power and capacities convoluted, and they scale poorly at large sizes. Fuel cells have potentially higher energy densities than batteries and can quickly be refuelled for recharging.

Fuel cells also have some limitations, beginning with a high cost, a significant impediment in mass adaptation. The low power densities compared to combustion engines and batteries; makes their application challenging for portable and automotive applications.

Depending on the electrolyte, fuel cells can be categorized into five types:

- I. Phosphoric acid fuel cell (PAFC)
- II. Polymer electrolyte membrane fuel cell (PEMFC)
- III. Alkaline fuel cell (AFC)

IV. Molten carbonate fuel cell (MCFC)

V. Solid-oxide fuel cell (SOFC)

The underlying electrochemical principles remain the same for all the five fuel cell types, but they operate at different temperature regimens with different materials.

Amongst these, PEMFCs capitalizes on the essential simplicity of fuel cell. PEMFCs work at low temperatures and, therefore, can start very quickly. The solid electrolyte makes it durable and robust, not prone to mechanical shocks and vibration. The thinness of MEAs helps make compact fuel cells. They operate at a lower temperature (80 °C), which is conducive for quick start-up in an automotive application.

1.2 Polymer Electrolyte (or Proton Exchange) Membrane Fuel Cell

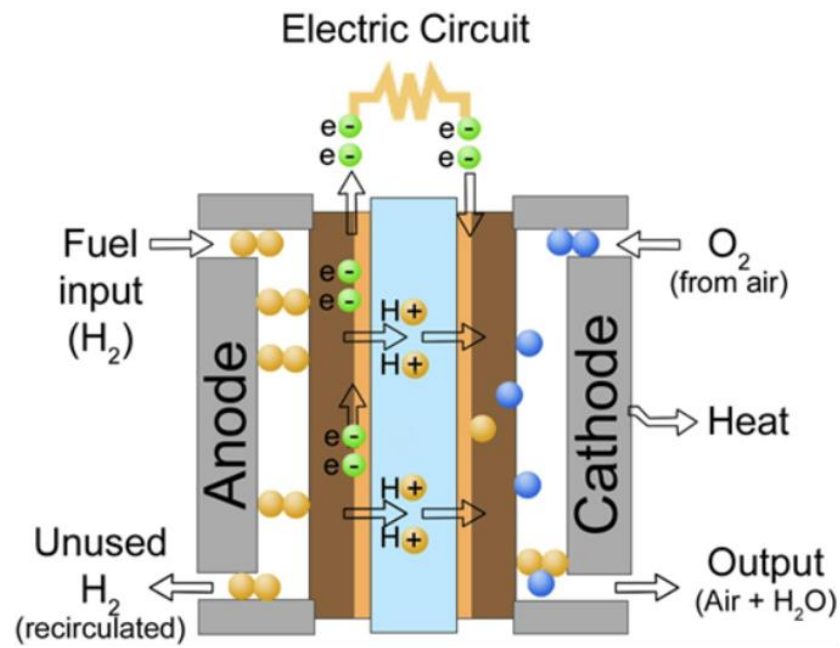
1.2.1 History of PEMFC

The first PEMFC was developed by General Electric by NASA in the 1960s for use on their first manned space vehicle. But, due to water management issues in the electrolyte, NASA used an alkaline fuel cell [4]. General Electric also did not pursue further development of PEMFCs because the costs of PEMFCs were higher than other fuel cells [5]. In the latter half of the 1980s and the early 1990s, the interest in PEMFCs has revived again [6].

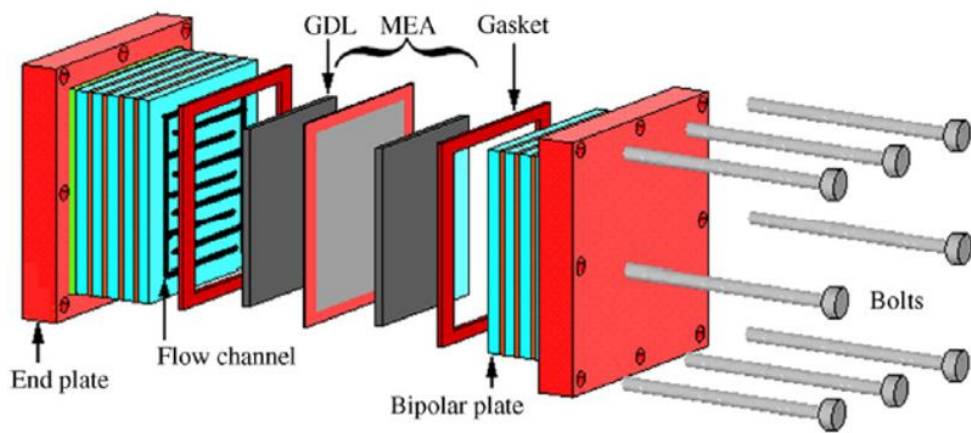
1.2.2 State of the art PEMFC design

The overall schematic of PEMFC is shown in Figure 1.1(a). The hydrogen gas is fed on the anode side, which gets oxidized to release electrons. The released protons traverse through a selective membrane, called a proton exchange membrane, to the cathode side. In contrast, the released electrons travel through the external circuit to reduce oxygen on the cathode side.

The central part of the PEMFC consists of anodic and cathodic Gas Diffusion Layers (GDL), which act as a showerhead for reactants to get uniformly distributed over the electrode surface. It comprises teflonized carbon cloth or carbon paper (TorayTM paper). This assembly is called the Membrane Electrode Assembly (MEA) and is considered the ‘heart’ of PEMFC. The MEA is inserted between bipolar plates, with flow channels grooved within them. The bipolar plates also act as a current collector and ensure continuity and integrity when cells are stacked in series (Figure 1.1(b)). GDL also removes liquid water from the catalyst layer to the flow channels and conducts electrons between the catalyst layer and the flow channel. GDL conducts heat to avoid hot spot formation on the catalyst layer.



(a)



(b)

Figure 1.1: (a) Schematic of PEMFC[27] (b) Schematic of PEMFC stack[28]

The oxygen on the cathode, protons from the PEM and electrons from the external circuit meet at a triple phase boundary; therefore, the ideal catalyst layer has to be porous (for gaseous reactant transport), conducting (for electron transport), and conducive for proton transport. The conventional electrocatalyst design consists of platinum nanoparticles dispersed on carbon black microspheres. The electronic conductivity is achieved by a randomly connected network of dispersed carbon particles in the matrix. The protonic conductivity is achieved by proton hopping from hydrated sulfonate groups in the Nafion solution in the interstices of the matrix. The catalyst layer is 10 μm to 30 μm thick. The Hydrogen Oxidation Reaction (HOR) and Oxygen Reduction Reaction (ORR) occur on the anode and cathode, respectively and are shown in equations (1.1) and (1.2), respectively. The difference in thermodynamic potentials of these two reactions gives the maximum theoretical potential achievable from a fuel cell, which is 1.23 V. Because the kinetics of the HOR is faster than ORR by 6 to 7 orders of magnitude, more than 50% of the overall cell voltage loss is due to ORR[7] and is therefore considered as the bottleneck of improving PEMFC performance[8].

The performance of a fuel cell is characterized by its polarization curve, which shows potential variation with current density. Figure 1.2 represents the polarization curve of a 5 cm² MEA of Toyota Mirai. The obtained potentials are lower than the thermodynamic potential because of the three losses:

- I. Activation overpotential losses: Activation loss arises from the slow reactions on the electrode surface.
- II. Fuel crossover losses: It is associated with waste of fuel passing through the electrolyte. Ideally, only protons should pass through, but rather some fuel diffusion and electron flow are also possible.

- III. Ohmic losses: It is a resistance to the flow of electrons through the electrode material/ interconnections and the flow of ions through the electrolyte. This drop is linearly related to the current density and therefore called ohmic loss.
- IV. Mass transport losses: These losses come from the change in concentration of the reactants at the electrode. At high current density, a lot of H_2O is produced, which impedes further diffusion of oxygen to the electrocatalytic sites, leading to a sudden drop in the current.

Therefore, the overall cell voltage is defined as equation (1.3)

$$E_{\text{cell}} = E_{\text{thermodynamic}} - \eta_{\text{activation}} - \Delta E_{\text{ohmic}} - \eta_{\text{mass transport}} \quad (1.3)$$

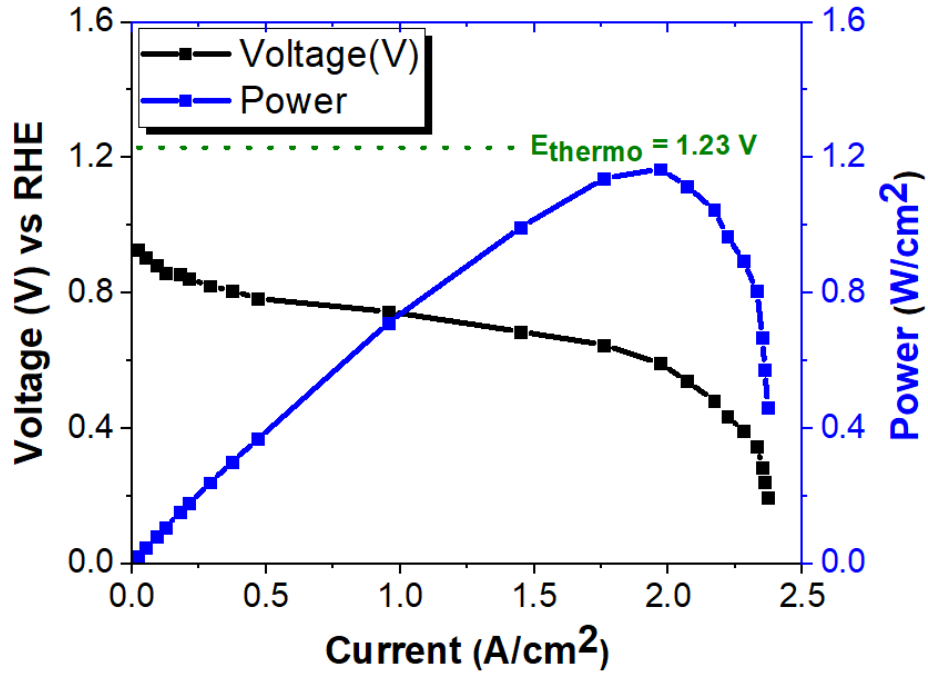


Figure 1.2: Polarization curve of 5 cm² MEA from Toyota Mirai [26]

1.3 Motivation

Significant advances have been made in PEMFC system design over the last three decades regarding cost-reduction and structural design.[9] The membrane electrode assembly (MEA), especially the electrode, is considered ‘the heart of a fuel cell and is designed to accommodate constraints imposed by the cost of platinum used for electrocatalysis and the need for efficient transport of electrons, reactants and heat. Consequently, the electrocatalyst structure and composition have evolved over the years, starting from platinum black having $4 \text{ mg}_{\text{Pt}}/\text{cm}^2$ [10] to nanoparticle coated carbon-black particles (Pt/C) using $<0.4 \text{ mg}_{\text{Pt}}/\text{cm}^2$ [11] and have a substantial gain in specific surface area. However, during fuel cell operation, the conducting carbon support corrodes due to high potentials experienced during start-up/shutdown[12]. Subsequently, the platinum nanoparticles dissolve and redeposit on other fuel cell parts [13]. These issues associated with the Pt/C catalyst have driven the search for carbon-free electrodes, having thin platinum or PGM-based catalytic layer on mesostructured conductive supports [14], [15]. The thin-film architectures can reduce the platinum loading to $0.05 \text{ mg}/\text{cm}^2$ [16] and reduce the surface area loss associated with the nanoparticle agglomeration while preventing corrosion of the underlying substrate [17]. Despite these advancements, there is ample scope for developing simpler and cost-effective additive fabrication processes and novel designs of the electrocatalyst layer to further reduce platinum/PGM loading of thin film nanostructured electrodes.

Electrodeposition is a simple, rapid and one-step fabrication method involving a low cost of the instrumentation and its maintenance for platinum-based electrocatalyst under ambient conditions [18], [19]. A recently reported Self-Terminating Electrodeposition(STED) method [20] has opened up an avenue for wet atomic layer electrodeposition under ambient conditions, which

combines basic electrochemistry and surface science. As such, STED has been a topic of interest for Fuel Cell vehicle catalysts [21], but there hasn't been a deep dive with respect to its performance evaluation for durability.

The present method for MEA preparation involves synthesizing carbon-supported catalyst slurry via solution-phase route and transferring it by decal transfer method onto either the membrane or gas diffusion layer (GDL)[22]. The transfer technique uses heat and pressure, brush painting, screen printing, doctor blade deposition or spraying[23]. But, these ink-based methods require tailoring of the rheology to the size of the doctor blades or nozzles[24]. They also suffer from uniformity issues and high platinum loading and thickness [23]. In this context, we synthesized porous, conducting and high surface area silver nanostructures on Nafion membranes using the salt-solution-based innovative *print-expose-develop* technique developed in our group [25]. We have been working on utilizing a self-terminating process for platinum monolayer deposition[20] onto inkjet-printed silver nanostructures to form conductive, porous, electrocatalytically active catalyst layers for PEMFC/DMFC applications. The ability to prepare ultra-low platinum loading electrodes for PEMFC/DMFC applications using an additive, roll-to-roll compatible process will be a significant impetus for enabling the widespread adaptation of fuel cells. Although a few groups have reported the use of inkjet printers to fabricate MEAs using inks formulated from ionomer containing slurries of Pt/C particles, our proposed methodology will eliminate the need for colloidal ink formulation and can also enhance platinum utilization while lowering platinum loading by forming overlayers onto inkjet printed conductive, nanoporous thin film substrates.

In the context of OECT, lowering the cost of PEMFC will enable the "Hydrogen" economy and provide a source for using natural gas. With Methanol being a

lightweight energy carrier, DMFCs are actively pursued as an energy-efficient and quiet alternative to supply off-grid power for months – without any user intervention, e.g. for powering automatic control systems and fulfilling the electrical power demand for safety and security control aspects on off-shore oil rigs or other remote locations (<https://www.efoy-pro.com/en/applications/oil-gas/>).

1.4 References:

- [1] E. Rignot, R. Thomas, and T. A. Report, “Cleaning the Air and Improving Health with Hydrogen Fuel-Cell Vehicles,” no. June, pp. 1901–1906, 2005.
- [2] M. G. Sürer and H. T. Arat, “State of the art of hydrogen usage as a fuel on aviation,” vol. 2, no. 1, pp. 20–30, 2018, doi: 10.26701/ems.364286.
- [3] F. B. P. Ryan O’Hayre, Suk-Won Cha, Whitney G. Colella, *Fuel cell fundamentals*, 3rd ed. New Jersey, US: John Wiley & Sons.
- [4] M. Warshay and P. R. Prokopius, “The fuel cell in space: yesterday, today and tomorrow,” *J. Power Sources*, vol. 29, no. 1–2, pp. 193–200, Jan. 1990, doi: 10.1016/0378-7753(90)80019-A.
- [5] D. A. J. R. Andrew L. Dicks, *Fuel Cell Systems Explained*, 2nd ed. John Wiley & Sons Ltd., 2003.
- [6] K. Prater, “The renaissance of the solid polymer fuel cell,” *J. Power Sources*, vol. 29, no. 1–2, pp. 239–250, Jan. 1990, doi: 10.1016/0378-7753(90)80023-7.
- [7] W. Sheng, H. A. Gasteiger, and Y. Shao-Horn, “Hydrogen Oxidation and Evolution Reaction Kinetics on Platinum: Acid vs Alkaline Electrolytes,” *J. Electrochem. Soc.*, vol. 157, no. 11, p. B1529, 2010, doi: 10.1149/1.3483106.
- [8] W. Chen *et al.*, “Origins of high onset overpotential of oxygen reduction reaction at Pt-based electrocatalysts: A mini review,” *Electrochem.*

- commun.*, vol. 96, pp. 71–76, Nov. 2018, doi: 10.1016/j.elecom.2018.09.011.
- [9] H. A. Gasteiger, S. S. Kocha, B. Sompalli, and F. T. Wagner, “Activity benchmarks and requirements for Pt, Pt-alloy, and non-Pt oxygen reduction catalysts for PEMFCs,” *Appl. Catal. B Environ.*, vol. 56, no. 1–2, pp. 9–35, Mar. 2005, doi: 10.1016/j.apcatb.2004.06.021.
 - [10] P. Costamagna and S. Srinivasan, “Quantum jumps in the PEMFC science and technology from the 1960s to the year 2000. Part I. Fundamental scientific aspects,” *J. Power Sources*, vol. 102, no. 1–2, pp. 242–252, Dec. 2001, doi: 10.1016/S0378-7753(01)00807-2.
 - [11] R. L. Borup *et al.*, “Recent developments in catalyst-related PEM fuel cell durability,” *Current Opinion in Electrochemistry*, vol. 21. Elsevier B.V., pp. 192–200, Jun. 01, 2020, doi: 10.1016/j.coelec.2020.02.007.
 - [12] C. A. Reiser *et al.*, “A reverse-current decay mechanism for fuel cells,” *Electrochem. Solid-State Lett.*, vol. 8, no. 6, pp. 273–276, 2005, doi: 10.1149/1.1896466.
 - [13] S. Chen, J. E. Soc, S. Chen, H. A. Gasteiger, K. Hayakawa, and T. Tada, “Platinum-Alloy Cathode Catalyst Degradation in Proton Exchange Membrane Fuel Cells: Nanometer-Scale Compositional and Morphological Changes Platinum-Alloy Cathode Catalyst Degradation in Proton Exchange Membrane Fuel Cells: Nanometer-Scale Compositional,” 2010, doi: 10.1149/1.3258275.
 - [14] M. Inaba, T. Suzuki, T. Hatanaka, and Y. Morimoto, “Fabrication and Cell Analysis of a Pt/SiO₂ Platinum Thin Film Electrode,” *J. Electrochem. Soc.*, vol. 162, no. 7, pp. F634–F638, Mar. 2015, doi: 10.1149/2.0201507jes.
 - [15] C.-F. Cheng *et al.*, “Nanoporous gyroid platinum with high catalytic activity from block copolymer templates via electroless plating,” *NPG Asia Mater.*, vol. 7, no. 4, p. e170, Apr. 2015, doi: 10.1038/am.2015.13.
 - [16] J. N. Tiwari *et al.*, “Multicomponent electrocatalyst with ultralow Pt loading and high hydrogen evolution activity,” *Nat. Energy*, vol. 3, no. 9, pp. 773–782, 2018, doi: 10.1038/s41560-018-0209-x.
 - [17] M. K. Debe, “Tutorial on the Fundamental Characteristics and Practical

- Properties of Nanostructured Thin Film (NSTF) Catalysts,” vol. 160, no. 6, pp. 522–534, 2013, doi: 10.1149/2.049306jes.
- [18] H. Park *et al.*, “Direct fabrication of gas diffusion cathode by pulse electrodeposition for proton exchange membrane water electrolysis,” *Appl. Surf. Sci.*, vol. 444, pp. 303–311, 2018, doi: 10.1016/j.apsusc.2018.03.071.
 - [19] N. Dimitrov, I. Achari, and S. Ambrozik, “Palladium ultrathin film growth by surface-limited redox replacement of Cu and H UPD monolayers: Approaches, pros, cons, and comparison,” *Electrochem. Soc. Interface*, vol. 27, no. 2, pp. 65–69, 2018, doi: 10.1149/2.f06182if.
 - [20] Y. Liu, D. Gokcen, U. Bertocci, and T. P. Moffat, “Self-Terminating Growth of Platinum Films by Electrochemical Deposition,” *Science*, vol. 338, no. 6112, pp. 1327–1330, Dec. 2012, doi: 10.1126/science.1228925.
 - [21] S. Proch *et al.*, “Iodide as Terminating Agent for Platinum Electrodeposition,” *Electrocatalysis*, vol. 11, no. 1, pp. 14–24, Jan. 2020, doi: 10.1007/s12678-019-00562-1.
 - [22] C. Kunusch, P. Puleston, and M. Mayosky, *Sliding-Mode Control of PEM Fuel Cells*. Springer Science & Business Media, 2012.
 - [23] S. Shukla, K. Domican, K. Karan, S. Bhattacharjee, and M. Secanell, “Analysis of low platinum loading thin polymer electrolyte fuel cell electrodes prepared by inkjet printing,” *Electrochim. Acta*, vol. 156, no. February, pp. 289–300, 2014, doi: 10.1016/j.electacta.2015.01.028.
 - [24] M. S. Saha, D. Malevich, E. Halliop, J. G. Pharoah, B. A. Peppley, and K. Karan, “Electrochemical Activity and Catalyst Utilization of Low Pt and Thickness Controlled Membrane Electrode Assemblies,” *J. Electrochem. Soc.*, vol. 158, no. 5, p. B562, 2011, doi: 10.1149/1.3559188.
 - [25] S. K. Parmar and V. Santhanam, “In situ formation of silver nanowire networks on paper,” *Curr. Sci.*, vol. 107, no. 2, pp. 262–268, 2014, doi: 10.18520/cs/v107/i2/262-269.
 - [26] D. J. Borup, Rodney L. More, Karren L. Myers, “FC-PAD: Fuel Cell Performance and Durability Consortium Update to USCAR Analysis of Toyota Mirai Components Provided by USCAR,” 2018, vol. 11.
 - [27] “More about Fuel Cells.” <https://www.spinam.eu/fc.html> (accessed Aug.

14, 2022).

- [28] E. Okel, B. Schaar, and O. Kanoun, “Simultaneous Measurement of Bulk and Contact Resistance of Conductive Materials for Fuel Cells,” in *2008 IEEE Instrumentation and Measurement Technology Conference*, May 2008, no. February 2014, pp. 1462–1465, doi: 10.1109/IMTC.2008.4547273.

Chapter 2

Literature Review

The hydrogen-based economy is crucial for sustainable energy development [1], [2]. The hydrogen-powered fuel cell can be advantageous in high-power mobile applications like automotive vehicles, which require a certain driving range. Polymer Electrolyte Membrane Fuel Cells (PEMFC) based vehicles (FCVs) can replace combustion engine-based vehicles as source-to-wheel greenhouse gas emissions are lower by 15-45% [3]–[5]. However, considerable innovations are required to achieve targets of cost (platinum group metal loading $< 100 \mu\text{g}/\text{cm}^2$), durability ($< 40\%$ loss of activity after 30k cycles), and performance ($0.44 \text{ A}/\text{mg}_{\text{Pt}}$ @ 0.9V)[6]. This challenge, along with the lack of hydrogen infrastructure, is a significant hindrance in the mass adaptation of FCVs despite demonstrating a technology readiness level (TRL) as high as TRL 9[7]. Currently, an FCV uses $\sim 6\text{x}$ platinum ($\sim 30 \text{ g}$ for the FC stack) compared to the amount present in the catalytic converters of ICE vehicles[8]. As per the US DOE guidelines, a potential electrocatalyst should be durable for at least 8,000 hours (corresponding to the 150,000 miles of driving on a lower average-speed drive cycle) with $< 10\%$ loss in performance[9]. The durability of the electrocatalyst layers is reduced in the harsh conditions present in the fuel cells, such as low pH, high potentials and dissolved oxygen[10]. So, there is ample scope for reducing platinum loading in FCVs to make durable electrocatalysts along the path to a hydrogen-based economy.

The DOE Merit Review meeting, 2018, provides an excellent overview of the current status of research directions aimed at reducing the cost and improving

the durability of catalysts while maintaining high specific activity. The multi-pronged approach being pursued in catalyst development includes theoretical computations aimed at understanding and providing material leads for circumventing the sluggishness of ORR kinetics, [11] developing strategies for synthesizing nanomaterials with tailored morphology, such as nanoframes, core-shell etc. to enhance intrinsic activity.[12], [13] Interestingly, Nanostructured thin film catalysts exhibited an x8 fold increase in activity over polycrystalline platinum facets. These approaches can address some of the DOE targets in terms of durability, activity, or PGM content at the lab scale (<https://www.energy.gov/eere/vehicles/annual-merit-review-presentations>). Still, several obstacles need to be surmounted before scaling up these findings.

Amongst the several approaches, nanostructured thin film architecture for the electrocatalyst layer is a promising route for cost-effective scaling up to the manufacturing scale. Nanostructured Metallic Thin Films(NSTF) find applications in various fields ranging from catalysis, electronics, and energy conversion to sensing. Typically, NSTFs are fabricated from substrates prepared by physical deposition onto nanostructured templates or by dealloying thin films. Recently, there have been developments in using additive technologies such as printing to form NSTF from nanoparticles as building blocks.

An effective way to reduce platinum loading while maintaining its performance is to coat the platinum only as an ultrathin skin, a few atomic layers thick, wherein the platinum utilization is maximized. However, control of platinum formation as atomic layers at room temperature and ambient pressure is difficult. Surface limited redox replacement reaction (SLRR) is one method for obtaining an atomic monolayer under ambient conditions. It comprises two steps: an underpotential deposition (UPD) of Cu [14] or Pb [15] followed by

galvanic displacement. The reversible nature of the UPD reactions[16] and the contamination by the residual UPD metals[17] limit the controllability of this step. Electrodeposition is a simple, additive, rapid and one-step fabrication method involving the low cost of the instrumentation and its maintenance for platinum-based electrocatalyst under ambient conditions [18], [19]. A recently reported Self-Terminating Electrodeposition(STED) method [20] has opened up an avenue for wet atomic layer electrodeposition under ambient conditions, which combines basic electrochemistry and surface science.

Platinum monolayer electrodeposition is challenging because a direct approach typically gives 3-D Pt growth.[21], [22] However, STED can grow Pt atomic layered film from a liquid electrolyte simply by cycling the potential between two values, equivalent to a wet atomic layer deposition. At the first potential value, the Pt deposition is quenched at potentials just negative of proton reduction via alteration of the double-layer structure induced by a saturated coverage of underpotential deposited hydrogen (H_{upd}). At a second potential value, the surface is reactivated for Pt deposition by stepping the potential to more positive values where the underpotential deposited hydrogen is oxidized and fresh sites for absorption of Pt salt are available. Unlike vapour-based methods like Atomic Layer Deposition (ALD) used in electrocatalyst synthesis, this method requires only a single plating bath. It does not incur energy-intensive setups or costly infrastructure. Moreover, this method is orders of magnitude faster than the vapour-phase ALD because each layer is produced by cycling the electrode potential rather than exchanging reactants. The applied electrode potential is the only parameter that controls the rate of reaction, and despite overpotential being more than 1 volt, Pt deposition gets quenched due to blocking of the additional deposition of Pt by H_{upd} . This also leads to less carryover of contaminants compared to the processes where reactants are

exchanged. Several studies report the application of platinum atomic overlayers formed using STED for hydrogen evolution reaction (HER)[16], [23]–[27], hydrogen oxidation reaction(HOR)[28], oxygen reduction reaction(ORR)[29], methanol/formic acid oxidation(FAO)[17], [30], [31], high temperature in-situ phosphoric acid fuel cell testing[32], pH sensing[33] etc. However, the durability performance evaluation of platinum overlayers in the context of FCV applications remains unexplored.

The present fabrication method for electrocatalyst preparation requires making a dispersion of carbon-based slurry and applying it on the substrate by decal printing, catalyst slurry or dry powder spreading, spraying or brush painting[34]. But these methods give catalyst layers with more than 3-5 μm [35] and lack sufficient control in uniformity. Since carbon is the major constituent, even a significant platinum reduction will result in only a slight volume change. Sophisticated thin film deposition methods like sputtering, pulsed electrodeposition, or ion-beam assisted deposition directly deposit the catalyst material on the substrate (either on PEM or GDL)[36]. Although platinum thin-film electrocatalysts synthesized using these methods give good initial activity, they are anticipated to be susceptible to rapid performance loss[37]. More so, the sophisticated and costly instrumentation employed in these techniques becomes a challenge for scale-up.

Inkjet printing doesn't have the usual limitations of conventional or ultra-thin deposition methods. Inkjet printing works on drop-on-demand technology, so transfer losses are significantly reduced compared to traditional methods like spraying, and it also provides controlled deposition. Because of its relatively low cost, it can easily be scaled up by increasing the number of nozzles in the printer head. Due to its high reproducibility, it maintains its adaptability and

versatility when scaled up[38]. Printing printed electronics is becoming a mature industry [39].

References:

- [1] K. Ehelebe *et al.*, “Platinum Dissolution in Realistic Fuel Cell Catalyst Layers,” *Angew. Chemie*, vol. 133, no. 16, pp. 8964–8970, Apr. 2021, doi: 10.1002/ange.202014711.
- [2] I. Gunnarsdottir, B. Davidsdottir, E. Worrell, and S. Sigurgeirsdottir, “Sustainable energy development: History of the concept and emerging themes,” *Renew. Sustain. Energy Rev.*, vol. 141, no. February, p. 110770, May 2021, doi: 10.1016/j.rser.2021.110770.
- [3] P. Joghee, J. N. Malik, S. Pylypenko, and R. O’Hayre, “A review on direct methanol fuel cells – In the perspective of energy and sustainability,” *MRS Energy Sustain.*, vol. 2, p. E3, Jan. 2015.
- [4] S. Sundarrajan, S. I. Allakhverdiev, and S. Ramakrishna, “Progress and perspectives in micro direct methanol fuel cell,” *Int. J. Hydrogen Energy*, vol. 37, no. 10, pp. 8765–8786, May 2012, doi: 10.1016/j.ijhydene.2011.12.017.
- [5] X. Liu, K. Reddi, A. Elgowainy, H. Lohse-Busch, M. Wang, and N. Rustagi, “Comparison of well-to-wheels energy use and emissions of a hydrogen fuel cell electric vehicle relative to a conventional gasoline-powered internal combustion engine vehicle,” *Int. J. Hydrogen Energy*, vol. 45, no. 1, pp. 972–983, Jan. 2020, doi: 10.1016/j.ijhydene.2019.10.192.
- [6] USDRIVE, “Fuel Cell Technical Team Roadmap,” 2017.
- [7] T. Mittermeier, A. Weiß, F. Hasché, G. Hübner, and H. A. Gasteiger, “PEM Fuel Cell Start-up/Shut-down Losses vs Temperature for Non-Graphitized and Graphitized Cathode Carbon Supports,” *J. Electrochem. Soc.*, vol. 164, no. 2, pp. F127–F137, 2017, doi: 10.1149/2.1061702jes.
- [8] A. Kongkanand, W. Gu, and M. F. Mathias, “Proton-Exchange Membrane Fuel Cells with Low-Pt Content,” *Fuel Cells Hydrog. Prod.*, pp. 323–342, 2019, doi: 10.1007/978-1-4939-7789-5_1022.

- [9] The US Department of Energy (DOE) Energy Efficiency and Renewable Energy, “Fuel Cell Multi-Year Research, Development and Demonstration Plan,” *Fuel Cell Technol. Off.*, vol. 2015, pp. 3.4.1-3.4.58, 2017, [Online]. Available: http://www.eere.energy.gov/hydrogenandfuelcells/mypp/pdfs/fuel_cells.pdf.
- [10] K. Sasaki, K. A. Kuttiyiel, and R. R. Adzic, “Designing high performance Pt monolayer core-shell electrocatalysts for fuel cells,” *Curr. Opin. Electrochem.*, vol. 21, pp. 368–375, Jun. 2020, doi: 10.1016/j.coelec.2020.03.020.
- [11] E. I. Solomon and S. S. Stahl, “Introduction: Oxygen Reduction and Activation in Catalysis,” *Chem. Rev.*, vol. 118, no. 5, pp. 2299–2301, 2018, doi: 10.1021/acs.chemrev.8b00046.
- [12] V. R. Stamenkovic, D. Strmcnik, P. P. Lopes, and N. M. Markovic, “Energy and fuels from electrochemical interfaces,” *Nat. Mater.*, vol. 16, no. 1, pp. 57–69, Jan. 2017, doi: 10.1038/nmat4738.
- [13] D. Li, H. Lv, Y. Kang, N. M. Markovic, and V. R. Stamenkovic, “Progress in the Development of Oxygen Reduction Reaction Catalysts for Low-Temperature Fuel Cells,” *Annu. Rev. Chem. Biomol. Eng.*, vol. 7, no. 1, pp. 509–532, Jun. 2016, doi: 10.1146/annurev-chembioeng-080615-034526.
- [14] J. Rossmeisl *et al.*, “Bifunctional anode catalysts for direct methanol fuel cells,” *Energy Environ. Sci.*, vol. 5, no. 8, pp. 8335–8342, 2012, doi: 10.1039/c2ee21455e.
- [15] S.-M. Hwang, J. E. Bonevich, J. J. Kim, and T. P. Moffat, “Electrodeposition of Pt₁₀₀-xPbx Metastable Alloys and Intermetallics,” *Journal of The Electrochemical Society*, vol. 158, no. 6, p. D307, 2011, doi: 10.1149/1.3572049.
- [16] Y. Liu, C. M. Hangarter, D. Garcia, and T. P. Moffat, “Self-terminating electrodeposition of ultrathin Pt films on Ni: An active, low-cost electrode for H₂ production,” *Surf. Sci.*, vol. 631, pp. 141–154, Jan. 2015, doi: 10.1016/j.susc.2014.06.002.
- [17] J. Byun, S. H. Ahn, and J. J. Kim, “Self-terminated electrodeposition of platinum on titanium nitride for methanol oxidation reaction in acidic electrolyte,” *Int. J. Hydrogen Energy*, vol. 45, no. 16, pp. 9603–9611, Mar.

2020, doi: 10.1016/j.ijhydene.2020.01.204.

- [18] H. Park *et al.*, “Direct fabrication of gas diffusion cathode by pulse electrodeposition for proton exchange membrane water electrolysis,” *Appl. Surf. Sci.*, vol. 444, pp. 303–311, 2018, doi: 10.1016/j.apsusc.2018.03.071.
- [19] N. Dimitrov, I. Achari, and S. Ambrozik, “Palladium ultrathin film growth by surface-limited redox replacement of Cu and H UPD monolayers: Approaches, pros, cons, and comparison,” *Electrochem. Soc. Interface*, vol. 27, no. 2, pp. 65–69, 2018, doi: 10.1149/2.f06182if.
- [20] Y. Liu, D. Gokcen, U. Bertocci, and T. P. Moffat, “Self-Terminating Growth of Platinum Films by Electrochemical Deposition,” *Science*, vol. 338, no. 6112, pp. 1327–1330, Dec. 2012, doi: 10.1126/science.1228925.
- [21] M. Liu, Z. Lyu, Y. Zhang, R. Chen, M. Xie, and Y. Xia, “Twin-Directed Deposition of Pt on Pd Icosahedral Nanocrystals for Catalysts with Enhanced Activity and Durability toward Oxygen Reduction,” *Nano Lett.*, vol. 21, no. 5, pp. 2248–2254, Mar. 2021, doi: 10.1021/acs.nanolett.1c00007.
- [22] S. Brimaud and R. J. Behm, “Electrodeposition of a Pt Monolayer Film: Using Kinetic Limitations for Atomic Layer Epitaxy,” *J. Am. Chem. Soc.*, vol. 135, no. 32, pp. 11716–11719, Aug. 2013, doi: 10.1021/ja4051795.
- [23] M. Li, Q. Ma, W. Zi, X. Liu, X. Zhu, and S. Liu, “Pt monolayer coating on complex network substrate with high catalytic activity for the hydrogen evolution reaction,” *Sci. Adv.*, vol. 1, no. 8, pp. e1400268–e1400268, 2015, doi: 10.1126/sciadv.1400268.
- [24] L. Pang *et al.*, “Controlled Pt Monolayer Fabrication on Complex Carbon Fiber Structures for Superior Catalytic Applications,” *Electrochim. Acta*, vol. 222, pp. 1522–1527, 2016, doi: 10.1016/j.electacta.2016.11.134.
- [25] L. Pang, Y. Zhang, and S. (Frank) Liu, “Monolayer-by-monolayer growth of platinum films on complex carbon fiber paper structure,” *Appl. Surf. Sci.*, vol. 407, pp. 386–390, 2017, doi: 10.1016/j.apsusc.2017.02.144.
- [26] H. Kim, J. Kim, G. H. Han, H. W. Jang, S. Y. Kim, and S. H. Ahn, “Hydrogen evolving electrode with low Pt loading fabricated by repeated pulse electrodeposition,” *Korean J. Chem. Eng.*, vol. 37, no. 8, pp. 1340–1345, 2020, doi: 10.1007/s11814-020-0617-z.

- [27] H. Kim, S. Choe, H. Park, J. H. Jang, S. H. Ahn, and S. K. Kim, “An extremely low Pt loading cathode for a highly efficient proton exchange membrane water electrolyzer,” *Nanoscale*, vol. 9, no. 48, pp. 19045–19049, 2017, doi: 10.1039/c7nr07224d.
- [28] Y. Liu, H. You, Y. C. Kimmel, D. V Esposito, J. G. Chen, and T. P. Moffat, “Self-terminating electrodeposition of Pt on WC electrocatalysts,” *Appl. Surf. Sci.*, vol. 504, no. June 2019, p. 144472, Feb. 2020, doi: 10.1016/j.apsusc.2019.144472.
- [29] Y.-J. Deng, V. Tripkovic, J. Rossmeisl, and M. Arenz, “Oxygen Reduction Reaction on Pt Overlayers Deposited onto a Gold Film: Ligand, Strain, and Ensemble Effect,” *ACS Catal.*, vol. 6, no. 2, pp. 671–676, Feb. 2016, doi: 10.1021/acscatal.5b02409.
- [30] S. H. Ahn, Y. Liu, and T. P. Moffat, “Ultrathin Platinum Films for Methanol and Formic Acid Oxidation: Activity as a Function of Film Thickness and Coverage,” *ACS Catal.*, vol. 5, no. 4, pp. 2124–2136, Apr. 2015, doi: 10.1021/cs501228j.
- [31] A. S. Lapp and R. M. Crooks, “Multilayer electrodeposition of Pt onto 1–2 nm Au nanoparticles using a hydride-termination approach,” *Nanoscale*, vol. 12, no. 20, pp. 11026–11039, 2020, doi: 10.1039/D0NR02929G.
- [32] D. K. Kim *et al.*, “Performance enhancement of high-temperature polymer electrolyte membrane fuel cells using Pt pulse electrodeposition,” *J. Power Sources*, vol. 438, no. November 2018, p. 227022, 2019, doi: 10.1016/j.jpowsour.2019.227022.
- [33] E. Lee, M. Sung, Y. Wang, and J. Kim, “Atomic Layer Electrodeposition of Pt on Nanoporous Au and its Application in pH Sensing,” *Electroanalysis*, vol. 30, no. 9, pp. 2028–2034, 2018, doi: 10.1002/elan.201800252.
- [34] M. S. Saha, D. Malevich, E. Halliop, J. G. Pharoah, B. A. Peppley, and K. Karan, “Electrochemical Activity and Catalyst Utilization of Low Pt and Thickness Controlled Membrane Electrode Assemblies,” *J. Electrochem. Soc.*, vol. 158, no. 5, p. B562, 2011, doi: 10.1149/1.3559188.
- [35] N. Wagner, T. KazK., and A. Friedrich, “Investigation of electrode composition of polymer fuel cells by electrochemical impedance spectroscopy,” *Electrochim. Acta*, vol. 53, no. 25, pp. 7475–7482, 2008,

doi: 10.1016/j.electacta.2008.01.084.

- [36] S. Shukla, K. Domican, K. Karan, S. Bhattacharjee, and M. Secanell, “Analysis of low platinum loading thin polymer electrolyte fuel cell electrodes prepared by inkjet printing,” *Electrochim. Acta*, vol. 156, pp. 289–300, 2014, doi: 10.1016/j.electacta.2015.01.028.
- [37] M. S. Saha, D. Malevich, E. Halliop, J. G. Pharoah, B. A. Peppley, and K. Karan, “Electrochemical Activity and Catalyst Utilization of Low Pt and Thickness Controlled Membrane Electrode Assemblies,” *J. Electrochem. Soc.*, vol. 158, no. 5, p. B562, 2011, doi: 10.1149/1.3559188.
- [38] and P. R. Towne, Silas, Vish Viswanathan, James Holbery, “Fabrication of polymer electrolyte membrane fuel cell MEAs utilizing inkjet print technology,” *J. Power Sources*, vol. 171, no. 2, pp. 575–584, 2007, doi: 10.1016/j.jpowsour.2007.07.017.
- [39] A. Lesch, F. Cortés-Salazar, V. C. Bassetto, V. Amstutz, and H. H. Girault, “Inkjet Printing Meets Electrochemical Energy Conversion,” *Chim. Int. J. Chem.*, vol. 69, no. 5, pp. 284–289, May 2015, doi: 10.2533/chimia.2015.284.

Chapter 3

Prudent Practices in Ex-Situ Durability Analysis for Platinum-based Electrocatalysts

3.1 Introduction

For ease of understanding and comparison, all the potentials in this article are converted to potential against the Reversible Hydrogen Electrode (RHE)[48]. All the currents are reported as density (currents per unit geometric area in A cm^{-2}). The promise of PEMFC technology to meet future transportation needs using renewable resources has spurred multifaceted research efforts on electrocatalyst development. An interdisciplinary approach aids rapid technological development, with researchers from different backgrounds, spanning science and engineering disciplines, participating. Performance characterization of a catalyst using electrochemical techniques requires a thorough understanding of various parameters involved. Following inappropriate protocols during electrochemical characterization of nanostructured materials leads to incomplete leverage or misinterpretation of the data.[1]

Typically, a newly developed electrocatalyst is available in small quantities ($<0.5 \text{ g}$)[2] and is characterized using ex-situ techniques before scaling up the synthesis for in-situ testing. The in-situ characterization of a new PEMFC catalyst involves high capital and operational costs, which can be prohibitive, especially in academic research labs.[3] Furthermore, in-situ protocols suffer from confounding issues as the performance losses due to Pt electrocatalytic

activity degradation and transport limitations are difficult to decouple. Laboratory-scale testing using half-cell liquid electrolyte setups has emerged as the method of choice for initial screening and rapid evaluation of electrocatalyst activity and durability. In certain configurations, such setups can minimize transport limitations. Durability testing entails the determination of ElectroChemically active Surface Area (ECSA) using cyclic voltammetry (CV) after stipulated number of cycles consisting of potential transients, which simulate the effects of varying power demand of a typical drive cycle in a fuel cell vehicle.[4] The ECSA is a widely accepted descriptor of electrocatalyst activity that links the measured currents with per-site turnover.[5] and also helps in quantifying the durability of the electrocatalyst.[6] Such a normalized measure is necessary to compare different morphologies of Pt electrocatalysts (e.g., nanoparticles,[7],[8] nanostructures,[9] alloy[10], [11]) to replicate potential breakthroughs and to compare with commercial standards.

The ex-situ durability tests simulating 30,000 automotive drive cycles of a fuel cell vehicle can last more than a day and require careful handling during data acquisition and analysis, but the requisite precautions are seldom highlighted. In our experience, even minor deviations in the experimental protocol can significantly impact the ECSA values computed during durability tests. To share the lessons learned, effective practices are demonstrated using exemplar data from our research on Pt films formed by atomic layer electrodeposition (refer to section S1 of supporting information for fabrication details). Herein, we emphasize the protocols to be followed during CV measurement and data analysis for ex-situ durability characterization of nanostructured Pt electrocatalysts. This chapter has a training manual format, anticipating that a nonelectrochemist will find the explanations presented here more approachable while functioning as a gateway to the in-depth analysis found in different literature sources.[2], [12]–[16]

3.2 Durability analysis for electrocatalysts

As per the US Fuel Cell Technology Office (FCTO) guidelines, a potential electrocatalyst must be durable for a minimum of 8,000 hours (equally reliable as IC engines, translating to roughly 1,50,000 miles of driving[17]) with less than 10% loss in performance.[18] To evaluate these commercial-scale fuel cell stack requirements, accelerated durability testing protocols for electrocatalysts use square wave potential sweeps, where successive cycles of oxidation and reductions cause accelerated catalyst degradation at the lower test time, but maintaining the degradation pathway[19]. Typically, this involves cycling between 0.6 V (3 s hold) and 0.95 V (3 s hold) (vs RHE) with a ramp time of ~ 0.5 s for 30,000 cycles.[18] Such rapid potential cycles replicate the Pt dissolution caused by voltage transients during vehicle start-up and shutdown; similarly, rapid triangular wave voltage cycling between 1.0 V and 1.5 V at 500 mV s⁻¹ for 5,000 cycles mimics corrosion of the support.[4] However, these protocols are performed at the level of a complete fuel cell stack (termed in-situ characterizations). Apart from requiring a relatively high amount of catalyst, the risk of electrical discontinuities confounding electrocatalyst activity determination also arises. Therefore, accelerated evaluation tests based on liquid electrolyte setups are highly desirable. The durability analysis employed in the present study uses linear scan cycles between 0.66 V to 1.01 V at 700 mV s⁻¹ while intermittently measuring ECSA to closely map the US DRIVE load-cycling protocol[4] and ex-situ testing protocols[20] outlined by the Department of Energy (DOE), USA.

3.3 Essentials of cyclic voltammetry

Electrochemistry deals with the coupling of heterogeneous electron transfer with chemical processes. Figure 3.1 illustrates the critical difference in electron transfer-based chemical reactions as compared to an electrochemical reaction —

(i) In a chemical reaction, homogeneous electron transfer occurs between the reducing and oxidizing couples. The Fermi level of electrons[21] pertaining to the reducing couple in solution (i.e., the redox potential of $\text{Fe}^{+3}/\text{Fe}^{+2}$ in . Figure 3.1 is higher than that of the Fermi level of electrons pertaining to the oxidizing couple (i.e. the redox potential of HA/A^- in Figure 3.1). This potential difference acts as a driving force for electron transfer. It is pertinent to note that the redox potentials are ensemble properties that consider complex solvation structures and hence do not correlate with the energy levels of molecular orbitals of constituent ions present in the electrolyte.[22] Instead, it is helpful to visualize this reaction as electron transfer between two electron reservoirs at different potentials. Also, as the reaction proceeds towards equilibrium, the concentration changes decrease the difference in the electron Fermi levels, and this difference vanishes upon attaining equilibrium composition,

(ii) In electrochemical reduction, the heterogeneous electron transfer to/from the electrode from/to an adsorbed ion occurs via the surface of the electrodes. It is mediated by the potential applied to the electrode. The applied potential alters the Fermi energy level of the electrode (a descriptor for free-electron energy levels in solids). It thereby controls the driving force for reduction (oxidation) of the oxidizing (reducing) species present in the electrolyte.[23] The facile control of the driving force (just by varying the applied voltage) makes electrochemistry a powerful tool.

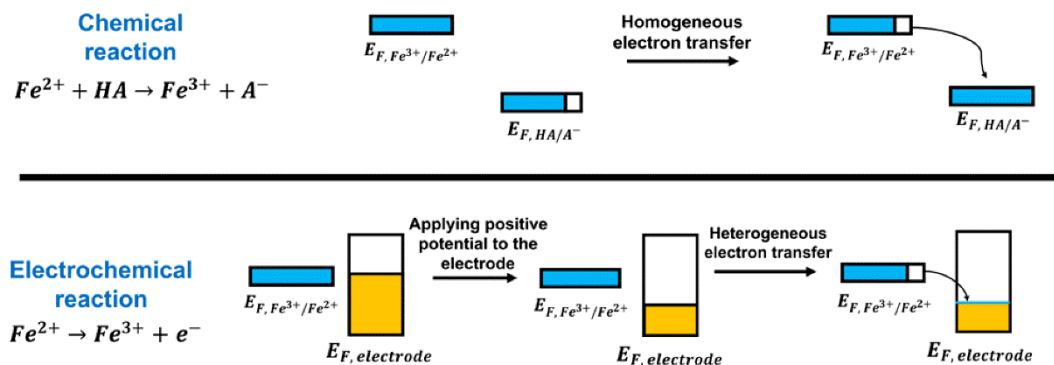


Figure 3.1: Schematic of electron Fermi levels (E_F) illustrating differences between a chemical and an electrochemical reaction. The electron Fermi levels in the solution of the Ferro/Ferri cyanide couple and Ascorbic acid/ Ascorbate couple are depicted as filled/partially filled reservoirs.

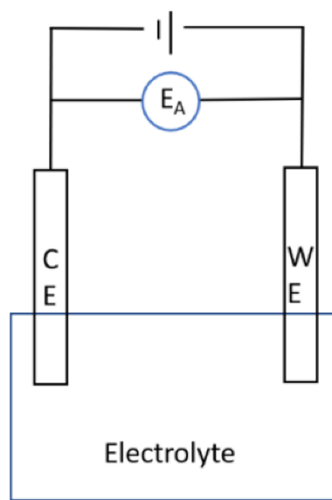
CV is considered “spectroscopy of the electrochemists”[1] and reflects the steady-state response of electron transfer initiated chemical reactions. It involves measuring the current response as the working electrode's potential is scanned over a specified range. The CV is a combined effect of the electroactive species’ mass transport to/from the electrode surface and the kinetics of the reaction at the electrode surface. For reversible redox couples, the peak separation gives essential information about electrochemical kinetics. It should be $59/n$ mV at room temperature, where n is the number of electrons transferred in the reaction.[24] Peak separations greater than $59/n$ mV denote slower electron-transfer kinetics than the time scale of potential sweep.[25] Each peak in the CV represents a Faradaic process governed by Faraday’s law and corresponds to the electron transfer process across the electrode-electrolyte interface. The area under the peak is a measure of the conversion of the reactants. Positive or negative charges adsorbed on the electrode surface leads to the Coulombic attraction of counterions from the electrolyte, resulting in an interfacial region with ionic characteristics between solid and liquid. This interfacial region is

visualized as two layers: The Stern layer comprising immobile ions adsorbed on the electrode surface and the diffuse layer comprising an extended layer of relatively mobile ions close to the electrode interface. The component of current related to capacitive charging of electrical double layer is known as non-Faradaic current.

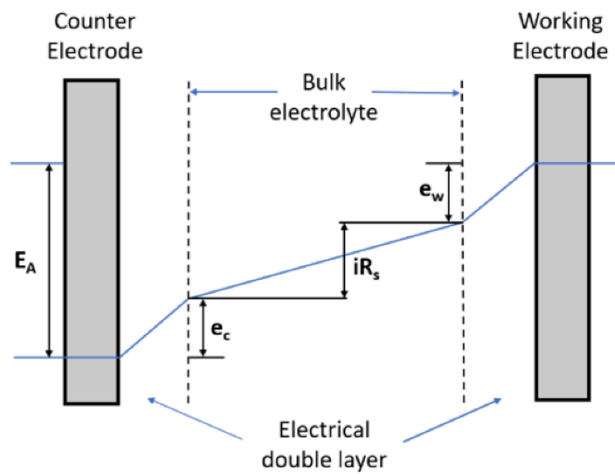
CV is executed in either a two or a three-electrode configuration for applying a potential across the working electrode/electrolyte interface using a potentiostat. The expected potential profiles across the electrodes, for these two configurations, are depicted in Figure 3.2a to Figure 3.2d; where E_A represents the potential applied by the potentiostat, e_r , e_c , and e_w are the potential drops within the double layers of the reference, counter, and the working electrode respectively. R_s refers to the solution resistance for the migration of ions, R_c and R_u refer to the compensated and uncompensated solution resistance (vide infra). iR_s , $i_w R_c$, and $i_w R_u$ denote potential drops due to solution resistance based on the total current (i), compensated solution resistance (R_c) based on the current flowing between working and the counter electrodes (i_w), and uncompensated solution resistance (R_u) based on the current flowing between the working and the reference electrodes (i_w) respectively.

In a two-electrode configuration, the counter electrode must serve two functions – to complete the electrical path of the circuit by allowing charge to flow through the cell and maintaining the constant interfacial potential, irrespective of current flow (Figure 3.2a). But it is challenging to maintain a constant counter electrode potential while significant current flows through the same terminal. Moreover, the lack of compensation for the solution resistance (potential drop across the solution, iR_s) also leads to difficulty controlling the working electrode potential in a two-electrode configuration (Figure 3.2b). Therefore, the roles of measuring current and maintaining constant interfacial

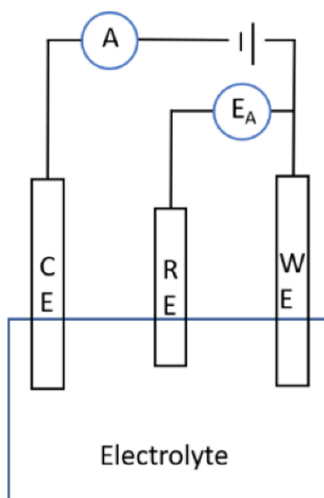
potential are better served by two separate electrodes. Thus, a three-electrode configuration has working, reference, and counter electrodes. The potentiostat controls the working electrode's potential against the reference electrode. The current flowing between the counter and the working electrode is measured (i_{WC} in Figure 3.2c). Since negligible current passes through the reference electrode (i_{WR}), the potential drop due to solution resistance between the reference and the working electrode ($i_{WR}R_u$) is minimal (Figure 3.2d). The solution resistance can be further minimized by decreasing the distance between working and reference electrodes. As the reference electrode cannot be placed infinitesimally close to the working electrode, uncompensated solution resistance (R_u) is unavoidable. The counter electrode's role in a three-electrode configuration is to complete the circuit by accepting/donating electrons (reversing the reaction that occurred at the working electrode) on its surface. For this purpose, its potential can even go to extreme values.



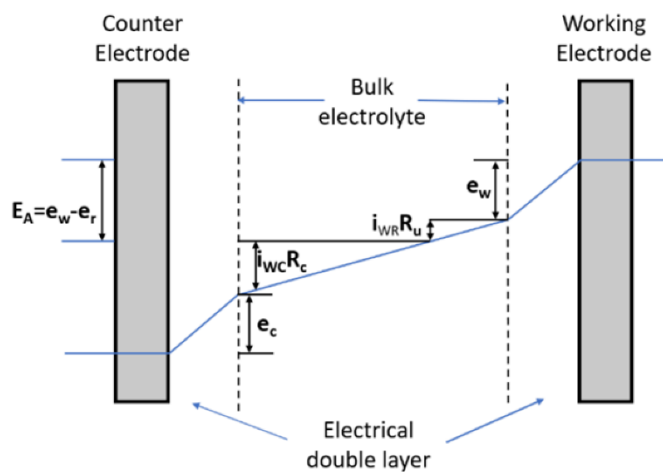
(a)



(b)



(c)



(d)

Figure 3.2: Schematic of (a) a two-electrode configuration and (c) a three-electrode configuration for CV measurements. E_A denotes applied potential, while CE, WE and RE refer to counter, working and reference electrode, respectively. (b) and (d) represent expected potential profiles in a two and a three-electrode configuration.[118] Note: RE is not shown in (d)

There are two main ways of representing CV data, depending on the axis orientation, i.e., IUPAC or US convention (Figure 3.3a and Figure 3.3b). In the IUPAC convention, the oxidation (anodic) currents are denoted as positive

values, whereas in the US convention, reduction (cathodic) currents are represented as positive values. In the IUPAC convention, the potential increases from left to right, while in the US convention, the potential increases from right to left. The IUPAC convention is followed throughout this article unless specified otherwise.

The shape of a CV curve for a reversible redox couple is discussed using data from potassium Ferro/Ferricyanide couple with illustrative snapshots of the double layer composition and associated mass transfer film (inset panels A to G in Figure 3.3). Typically, the potential scan begins where no electrochemical reaction (Faradaic process) is expected to occur (i.e., only signals from the non-faradaic process are present), represented by point A in the graph. Upon scanning the potential towards B, as the oxidation potential of Ferrocyanide is approached, a sudden rise in the current occurs due to the onset of the Faradaic reaction (governed by the Butler-Volmer equation.[26]) Upon further increase in potential, the current signal peaks at point C, representing a balance between diffusive flux (i.e., transport of ions from the bulk liquid through the mass transfer film region to the Debye layer on the electrode's surface) and the reaction flux on the electrode.[27] Beyond point C, the current decreases, despite having a higher overpotential (driving force) for surface reaction. The current declines because diffusion of Ferrocyanide is hindered by the widening of the mass transfer film, which contains the converted Ferricyanide ions. This widening leads to a lower concentration gradient for further conversion of Ferrocyanide ions and so, the current has a gradual fall-off with $t^{-1/2}$ dependence between point C to D.[28] Theoretically, if the potential scan is maintained for infinite time, all the reactants would oxidize. Then, there will be a zero slope at point D, corresponding to the electrode surface and the mass

transfer film having only Ferricyanide ions. But practically, the potential is reversed after a finite time, and so the mass transfer film has some Ferrocyanide at the potential reversal point D.

Upon potential scan reversal, similar phenomena occur for Ferricyanide reduction with nonzero current at potential reversal (at the point G). During the reverse voltage scan, the reduction peak has a similar qualitative nature but appears inverted because of the reversed current direction. It is interesting to note that for the first cycle, the last point of the first cycle (A') has sufficient negative currents than that of the starting point of the first cycle (A) because, at point A, the electrode surface is devoid of Ferricyanide ions. However, at the starting point of the next cycle, i.e., point A', some Ferricyanide is present in the mass transfer film near the electrode due to potential reversal within a finite time from point G. As seen in Figure 3.3a, for the 5th cycle, the starting and the ending points match reasonably with each other, both having a negative current – indicating a steady state. The standard practice in the electrochemistry literature is to report the CVs after the system has achieved the steady state. Therefore, the negative/positive currents should not be conceptualized as reduction/oxidation currents, especially near the potential reversal region. Thus, the zero current for a CV graph does not hold much significance for the steady state; and therefore, some researchers also use the scalebar for current axis instead of absolute values.

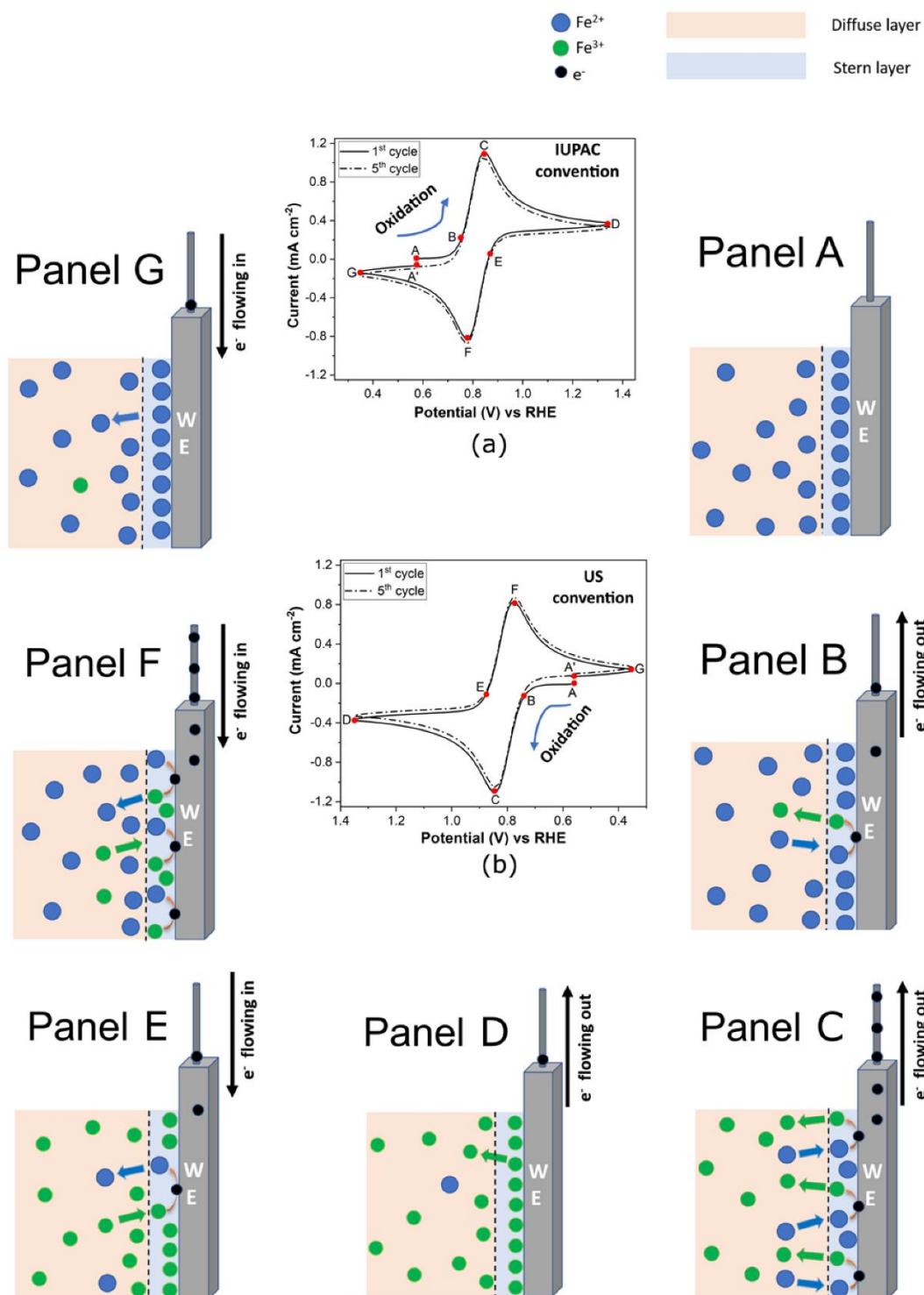


Figure 3.3: (a) IUPAC and (b) US convention for reporting CV data using the example of potassium Ferro/Ferricyanide redox couple in 1M KNO_3 + 10 mM $\text{K}_4\text{Fe}(\text{CN})_6$ at 25 mV s^{-1} scan rate. Panels A to G represent Illustrative snapshots of double layer at the electrode- electrolyte interface corresponding to points labelled in CV.

For reversible redox couples, the electron transfer step is much faster than the diffusion of the reactant to the electrode, so the diffusion of the reactant decides the shape of the curve. Moreover, the diffusivities of oxidants and reductants are different. Therefore, the “duck” shape for a reversible redox couple is attributable to differences in diffusion rates of the oxidants and reductants to and from the electrode surface through the mass transfer film. It is pertinent to note that the current signal in a CV is proportional to the area of the electrode immersed inside the electrolyte; therefore, it is good practice to report current as density (Current per unit electrode area).

3.4 Effective practices during ex-situ durability analysis

3.4.1 Electrochemical setup and selection of electrodes

A schematic of a lab-scale electrochemical setup for a three-electrode CV is shown in Figure 3.4a. The working electrode should directly face the counter electrode to experience a uniform electric field. The counter electrode area is ~ 10 higher[29] than that of the working electrode to avoid electron transport limitations for the working electrode reaction. The counter electrode is designed to act as a source/sink of electrons and ensure no additional charge build-up at the working electrode affecting its potential. The reference electrode is chosen such that its potential is stable in the electrolyte pH and the potential window used while allowing negligible current to flow through it (i.e., non-polarizable). There are several options for choosing a reference electrode[26] for PEMFC electrocatalyst ex-situ durability analysis in acidic conditions. Silver-Silver Chloride ($\text{Ag}_{(s)}/\text{AgCl}_{(s)}/\text{Cl}^{-}_{(aq)}$) or Saturated Calomel Electrode ($\text{Hg}_{(l)}/\text{Hg}_2\text{Cl}_{2(s)}/\text{Cl}^{-}_{(aq)}$) are the most widely used; however, for the ease of comparison and reproducibility, all the potential should be converted to a

standard scale like reversible hydrogen electrode (RHE). The commercially procured reference electrodes are often calibrated against the standard hydrogen electrode (SHE). However, the SHE scale doesn't account for changes in the temperature or the pH effect of the solution. So, RHE scale ($V_{\text{RHE}} = V_{\text{SHE}} - 0.0059 \cdot \text{pH}$ at 298 K) is widely used as 0 V corresponds, by definition, to the onset of Hydrogen Evolution Reaction (HER) under the experimental conditions used.[30] The reference electrode should be placed close to the working electrode to minimize the solution resistance. Increased solution resistance can, apart from shifting the working electrode potential, decrease the peak currents, broaden the peaks and increase the peak separation than predicted theoretically for reversible systems.[28]

Commercially available cells like the one shown (Figure 3.4b), where the cell cap has openings to hold all three electrodes in place conveniently, are helpful for beginners. The working electrode should be immersed such that it remains undisturbed by the perturbations on the free surface and edges of the wall. A needle (inserted via a small hole on the electrochemical cell cap) is used to create a blanket of inert gas on top of the electrolyte, which minimizes O_2 diffusion into the electrolyte due to the concentration difference between the ambient atmosphere and the electrolyte. An external pre-bubbler is also added before the electrochemical setup (Figure 3.4a) to saturate the inert gas fed to the electrochemical cell. Saturated inert gas helps minimize electrolyte evaporation during the day-long ex-situ durability analysis, which could otherwise lead to electrolyte height variations.

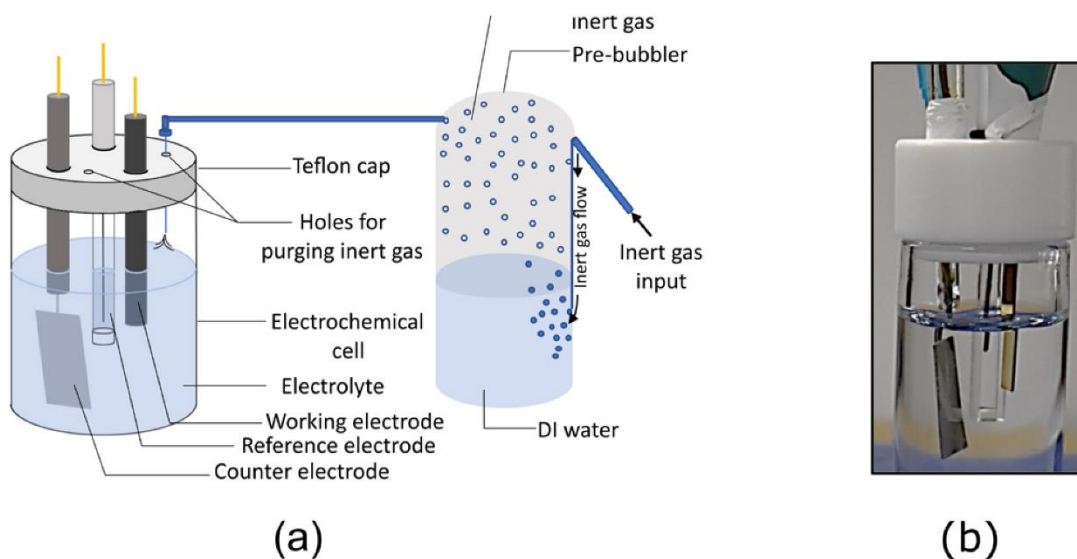


Figure 3.4: (a) Schematic of an electrochemical setup for three electrode CV measurement (b) photograph of a lab-scale three-electrode setup.

The electrode connections should be cleaned with sandpaper regularly to remove rust- which might form due to reaction with the acidic vapours from the electrolyte. The electrical connectors should be insulated with Teflon tape while experimenting. The integrity of the insulation on the clips should be checked with a multimeter. A Faraday cage should be used to prevent electrical interferences, especially during low current measurements. It is good practice to start the electronic equipment used in the lab at least half an hour before using them to minimize noise from the thermal fluctuations due to the warming up of the internal circuitry components.

3.4.2 Cleaning/Pre-treatment protocols for electrochemical setup and electrodes

The presence of uncontrolled impurities would cause irreproducibility in CV measurements. So, it is essential to have a robust cleaning procedure for the

electrochemical cell, glassware, electrodes, and electrolyte, which the following section discusses.

3.4.2.1 Glassware cleaning

A variety of acid soak cleaning procedures are reported, including the use of piranha solution[31] (3:1: H₂SO₄: H₂O₂, CAUTION: Care should be taken to add H₂O₂ in a drop-by-drop manner; otherwise, it may cause detonation. Piranha solution should not be sealed to gas evolutions. It should be disposed off with appropriate care after it cools down), hot concentrated nitric/[32] sulphuric acid,[33]–[35] aqua regia[36] (3:1:: HCl: HNO₃, CAUTION: Aqua regia is highly corrosive and can result in explosion or skin burns if not handled with care), acidified KMnO₄[37] to remove organic and inorganic impurities from the glassware. After acid soaking, the electrochemical cell should be washed with DI water thoroughly and boiled/sonicated in DI water repeatedly, replacing DI water each time. When glassware is not in use, it must be stored carefully to prevent dust or other particulate matter from entering the cell. Alternatively, they can be kept in a cleaned evacuated vessel or submerged inside a closed DI water container to avoid contamination from the air[38] or covered with an airtight film if queued on the workbench.

3.4.2.2 Pre-treatment of the working electrode

Often, the working electrodes are synthesized with the help of some stabilizing agents, which need to be removed from the surface, as reproducible measurements would be possible only on a “clean” surface. Post-synthesis cleaning or pre-treatment can activate the electrode by metal dissolution and partial redeposition, resulting in surface reconstruction and removal of the adsorbed species.[39] A stable and reorganized surface is formed by such activation, on which electrochemical experiments can be conducted[40]–[42]

with enhanced repeatability.[43] But it is difficult to correlate the extent of activation with surface change. Therefore, only experiments can suggest an optimal pre-treatment for a given application.

Apart from mechanical polishing to clean the working electrode,[44] electrochemical methods like CV can activate the working electrode. For over four decades of research in Pt electrocatalysis, the way to readily evaluate the Pt electrocatalyst surface cleanliness is simply by analyzing the hydrogen adsorption/desorption region in a CV.[45] This includes potential cycling until a stable CV is obtained.[15], [16], [46]–[53] Generally, such activation CV cycles are carried out till the CV profile retraces itself (as shown in Fig. xxxyy), a sign of steady state at the electrode/electrolyte interface.[46] To minimize the voltage loss due to iR drop,[54] a smaller-sized working electrode, which leads to a lower current, is preferable. The size of the working electrode should be decided by considering the practical issues with handling the electrode (feasibility of making connections in small-sized electrodes etc.)

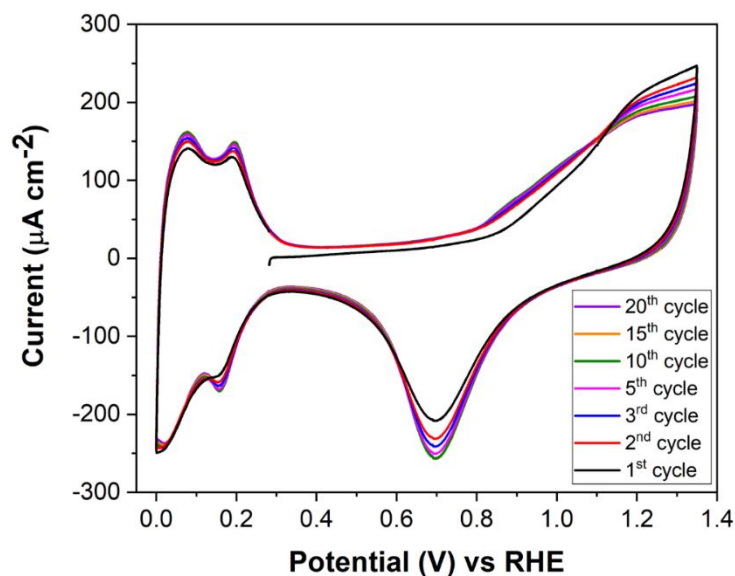


Figure 3.5 : CV profile for pre-treatment of working electrode showing retraining of the CVs after the steady state is attained in 15 cycles

3.4.2.3 Pre-treatment of Reference Electrode

In this section, characterization and cleaning protocols are provided for the Silver-Silver Chloride ($\text{Ag}_{(s)}/\text{AgCl}_{(s)}/\text{Cl}^{-}_{(\text{aq})}$) reference electrode, on account of its environmental compatibility. Ag-AgCl reference electrode has a stable voltage at the interfaces of Ag-AgCl and AgCl-KCl. Sometimes, the AgCl layer on the electrode turns black due to tarnishing after light exposure, which usually does not affect the performance adversely and can be removed by sanding with fine non-metallic sandpaper. The Ag-AgCl electrode should not be directly placed under sunlight or exposed to UV-visible light as Ag^{+1} will be reduced to Ag^0 . Over prolonged usage of the Ag-AgCl reference electrode, one can notice that the coating of AgCl has partially come out due to the accumulative effect of the negligible current that flows through the reference electrode. This current converts the AgCl into silver atoms and Cl^{-} ions, which are hydrated. The AgCl can be recoated by anodizing (applying a positive voltage as compared to the reduction potential of Ag) in 1 M HCl or KCl for a minute; so that the silver

atoms from the wire give up their electrons and combine with the Cl^- in the solution to make insoluble AgCl coating.

In the Ag-AgCl electrode, a VycorTM (porous glass) frit is used to ensure electrical contact of the reference electrode with the electrolyte by allowing ionic transport into the electrode while minimizing solution mixing (Figure 3.6a). The $\text{Ag}_{(s)}/\text{AgCl}_{(s)}/\text{Cl}^-_{(\text{aq})}$ electrode should be stored in a KCl solution having a concentration just slightly less than saturated KCl . Keeping the solution just below saturation and replacing the storage solution of KCl at regular intervals helps to maintain sufficient ionic flow to prevent salt crystallization in the glass pores. While refilling the KCl solution, sometimes air bubbles become entrapped next to the frit, which should be removed by a gentle tap on the bottom part of the electrode. Crystallization in the Vycor frit damages the reference electrode by increasing the impedance and changing the liquid junction potential, leading to a drift of the reference potential with time (Note: Liquid junction potential drops exists at the interface of two solutions of electrolyte having different concentrations.[26]) The discoloration of the Vycor frit is due to salt precipitation inside the pores, and it hinders ionic transport. A reference electrode should be checked against a master electrode through an open circuit potential (OCP) test before use. A stable reference electrode should not have a potential difference of more than ± 5 mV against a master electrode in the OCP test at steady state.[55] As an illustration, we compare two reference electrodes in Figure 3.6b, one with a regular (colorless) frit and the other with a discolored frit. Though the discolored frit gives a high initial OCP against a master Ag-AgCl electrode (Figure 3.6c), it eventually stabilizes to the same value as that of the normal frit. Initial high departure from the equilibrium potential is due to partial blockage of the frit by salt precipitation, which doesn't entirely hinder the movement of the ions. Instead, it achieves equilibrium after a long time.

Such reference electrodes with partially/completely blocked frit can be reused after cleaning the frit in a strong oxidizing agent[56] or replacing the frit. A more involved way to characterize the reference electrode is through impedance measurement, where the high impedance of the reference electrode is attributed to a blocked frit.

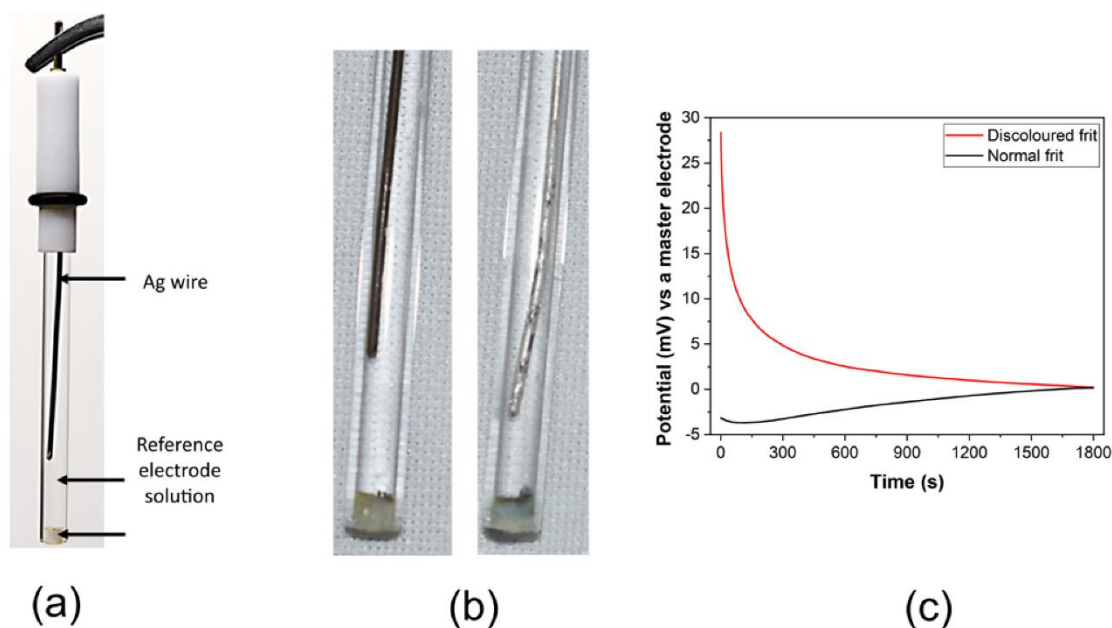


Figure 3.6: (a) Photograph of an Ag/AgCl reference electrode (b) Photograph showing tarnishing(left) and discolouration of the Vycor™ frit(right) in used Ag/AgCl reference electrodes (c) Comparison of Ag/AgCl reference electrodes' OCP profiles in 0.1M HClO₄.

3.4.2.4 Pre-treatment of Counter Electrode

The most frequently used counter electrode is Pt due to the rapid electron transfer requirement. One must make sure that the Pt counter electrode is free from organic and inorganic contaminants. To remove inorganic contaminants, one can boil it in concentrated HNO_3 for ~ 1 minute[57] or dip it in aqua regia for a second or two. The reaction with aqua regia is rapid, and it leaches the top layer of Pt.[58] One can dip Pt counter electrode in piranha solution, which oxidizes organic contaminants present on the Pt surface to remove organic impurities. One can place the Pt counter electrode over a Bunsen burner's flame until it turns red hot to oxidize all the organic contaminants. For quick daily cleaning purposes, one can clean the Pt electrode by sonicating it in acetone followed by isopropyl alcohol (IPA) and drying it under a nitrogen (N_2) stream. Finally, one must electrochemically clean the counter electrode by performing CV in a wider potential window than the working electrode pre-treatment. The cleaned Pt foil has more prominent features corresponding to the electrochemical activity of Pt than the uncleaned one, as shown in Figure 3.7. The cleaning protocol followed in this thesis is 1 min dipping in piranha, followed by sonication in DI water three times for 2 min each to remove the residual piranha while ensuring to change DI water every time. It was further electrochemically cleaned by cycling the potential between 0 to 1.35 V for 20 cycles at 100 mV s^{-1} . The current densities are reported at the steady state (i.e., the current value is within 1% of the preceding cycle[59]).

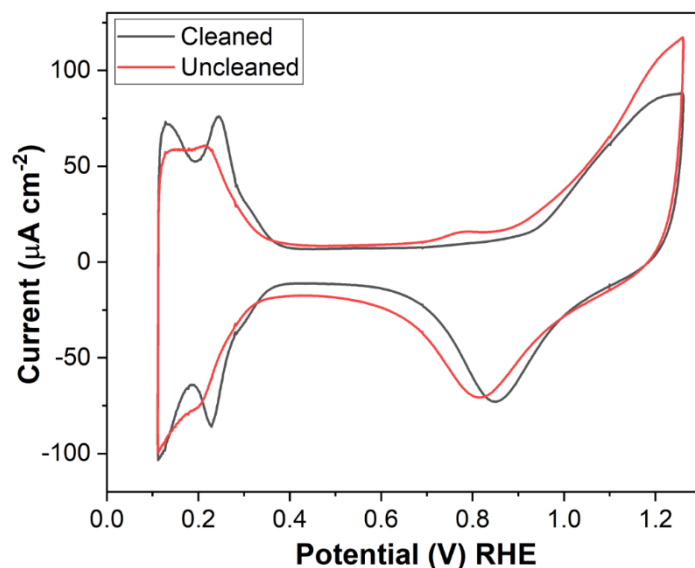


Figure 3.7: CV comparison of a cleaned and an uncleaned Pt counter electrode

3.4.3. Electrolyte preparation

The electrolyte should be purged with an inert gas (N_2 or Ar) to remove the dissolved oxygen. In voltammetric experiments, overall charge and species transport by convection can disturb the mass transport and lead to difficulty interpreting the CV data. So, to suppress migration of the electroactive species, supporting electrolyte is added, usually at 10-50 times the concentration of species of interest. Typically, alkali metal salts are used as supporting electrolytes in a concentration between 0.1 to 1 M, which enhances the ionic strength and conductivity of the electrolyte. To avoid interference, supporting electrolytes should not have any electroactive species within the potential range used but should have a common ion with the primary electrolyte. Deionized (DI) water should be used to prepare electrolytes to avoid trace metal impurities

and dissolved ionic impurities like Na^+ , K^+ , Ca^{2+} , NO_3^- , Cl^- etc. The quality of DI water is determined by the resistance and should have at least $18 \text{ M}\Omega\text{-cm}$ resistivity at 25°C .

3.5 Analysis of Pt CV and calculation of ECSA

Hydrogen underpotential deposition (H_{upd}) is the most frequently used method to determine ECSA for monometallic Pt[52], [60] amongst alternatives such as Ag_{upd} [52]/ Sn_{upd} [61], [62] /CO stripping[63]/ Cu stripping,[64], [65] etc. H_{upd} refers to the hydrogen adsorption/desorption that occurs at potentials that are positive with respect to the reduction potential for hydrogen evolution. The Pt CV is a strong function of the morphology, microenvironment at the electrode-electrolyte interface,[66] crystal orientation,[5], [67] and electrolyte composition.[2], [66] Typically, Pt CV is performed in an acidic solution to mimic the electrode-membrane interface environment during fuel cell operating conditions.[11] Figure 3.8a shows a typical CV of a polycrystalline Pt electrode in 0.1 M HClO_4 . The electrochemical signature of a Pt electrode consists of three major regions, which will be discussed in the following sections :1) H_{upd} region from $\sim 0.05 \text{ V}$ to $\sim 0.4\text{-}0.5 \text{ V}$, where protons from the electrolyte are adsorbed and desorbed on the Pt surface. 2) A double layer charging (capacitance) region between $\sim 0.3\text{-}0.5 \text{ V}$ to $\sim 0.7\text{-}0.8 \text{ V}$. 3) Pt surface oxidation and reduction currents in the region $> \sim 0.7\text{-}0.8 \text{ V}$ till the upper potential limit of CV.

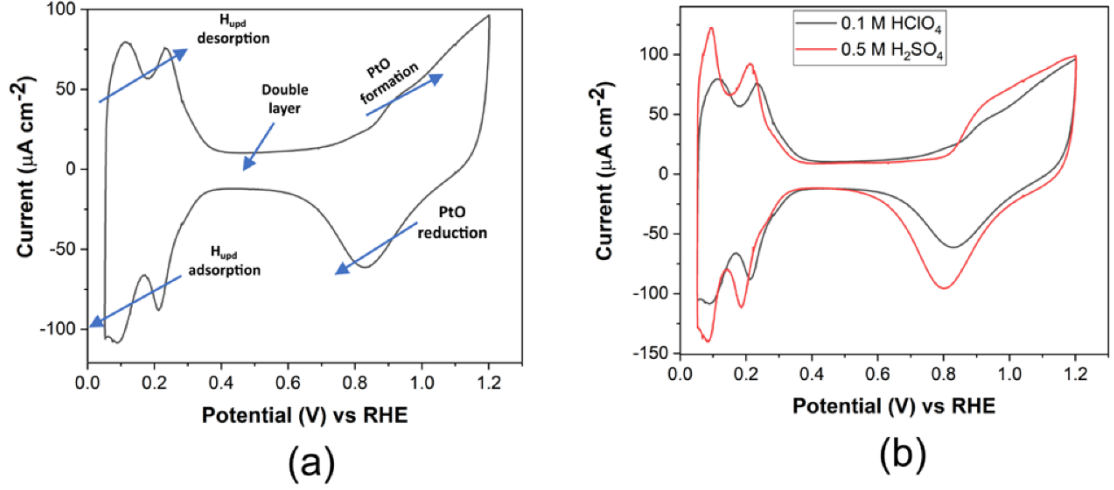


Figure 3.8: CV of polycrystalline Pt foil (a) using 0.1 M HClO₄ electrolyte, (b) comparison of CV in 0.1 M HClO₄ with CV in 0.5 M H₂SO₄ at 50 mV s⁻¹ scan

The choice of appropriate electrolyte has been discussed in literature,[68], [69] and HClO₄,[5], [46], [70], [71] H₂SO₄,[72]–[75] or H₃PO₄[2], [76] are mostly used. The use of HClO₄ is favoured because it exhibits non-adsorbing or weakly adsorbing characteristics on Pt[38], [77]–[80] and simulates the role of the Nafion[™] membrane better than what H₂SO₄ or H₃PO₄ can. But, HClO₄ can have appreciable Cl⁻ impurities[81] and is prone to decomposition during the operation.[2] Therefore, several researchers also use H₂SO₄. [73]–[75], [81], [82] While using the HClO₄ electrolyte, the concentration is decided based on a compromise between higher electrolyte conductivity and lower impurity level. Typically, the concentration of HClO₄ used is 0.1 M[5], [46], [63], [70], [71] to limit the Cl⁻ impurities, while that for H₂SO₄ is 0.5M.[73], [75], [83], [84] However, the Pt electrocatalyst activity is confounded in H₂SO₄ or H₃PO₄ because Pt is highly susceptible to HSO₄⁻, SO₄²⁻ and PO₄³⁻ adsorption.[47], [85]–[87] Such adsorption leads to overestimating H_{upd} values, as anion adsorption coincides with the H_{upd} potential region.[2], [88] Figure 3.8(b) compares the CV

of a polycrystalline Pt foil sample in 0.1 M HClO_4 and 0.5 M H_2SO_4 , where a significant increase in the H_{upd} charge is seen. The sections below discuss in detail three major regions in the CV of a Pt foil. Further, the effects of various missteps that lead to deviations from the standard profile are demonstrated, which can help troubleshoot CV setup and performance.

3.5.1 H_{upd} region (from ~ 0.05 V to ~ 0.3 - 0.5 V)

H_{upd} is observed from ~ 0.05 V to ~ 0.3 V - 0.5 V [15], [63], [73], [75], [83], [84], [89] and observed only in selected metals like Pt, Rhodium (Rh), Palladium (Pd), and Iridium (Ir) amongst all the metals which support Hydrogen Evolution Reaction (HER). [67] H_{upd} is observed when electro-adsorption (adsorption aided by the electrical potential) of H^+ is energetically more favorable than that of O^- containing species (O^{2-} or OH^-). [67] For polycrystalline Pt samples, different crystal facets lead to structure-sensitive adsorption. [90] This difference is attributed to the selective interaction of different exposed facets with H_3O^+ and the extent of OH^- species adsorption. [11] The peak shapes, numbers, and magnitudes in the H_{upd} region correlate to different Pt facets becoming active. Thus, the orientation of the steps and terrace sites on the surface determines the electrocatalytic activity of an electrode. [91] The more positive is the peak potential relative to 0 V, the higher is the free energy of adsorption, corresponding to a stronger Pt-H bond. [54]

The H_{upd} method determines electrochemically active Pt surface area by scanning through the potential range at which H_{upd} protons from the acidic electrolyte can adsorb/desorb on Pt surface. The total charge density Q_{H} (C cm^{-2}) corresponding to the $\text{H}_{\text{ads}}/\text{H}_{\text{des}}$ is calculated by integrating the area under the H_{upd} peak (Eq. (1)).

$$Q_H = A^{-1} \int_{V_1}^{V_2} (I - I_{dl}) dV/v \quad (1)$$

Where:

Q_H : total charge density ($C\ cm^{-2}$) related to H_{ads}/H_{des}

A : Geometric electrode area

I : Measured Current

I_{dl} : Double layer charging current

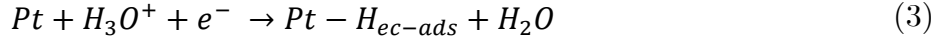
V : Potential (V)

v : Scan rate ($V\ s^{-1}$)

ECSA calculation using the H_{upd} approach is based on the following assumptions: 1) a saturated adlayer of hydrogen is formed in the potential range of ~ 0.05 to $\sim 0.3V-0.5\ V$. 2) The stoichiometric ratio of the adsorbed hydrogen atom to the surface Pt atom is 1:1.[64] 3)The H^* monolayer adsorbed on the Pt surface is unaffected by the anion adsorption. 4) The constant double-layer charge/discharge correction extends to the hydrogen region. The ECSA is calculated by dividing Q_H with the Pt loading and the normalizing factor of $210\ \mu C\ cm^{-2}$, the nominally accepted charge corresponding to a monolayer of H_{upd} adsorption/ desorption on polycrystalline Pt sample. The value of $210\ \mu C\ cm^{-2}$ presumes an equal distribution of (100), (111), and (110) – the three low index planes of Pt.[92] A few research groups use other values such as 200, 220, or $230\ \mu C\ cm^{-2}$. [93]–[95] The most commonly used formula for ECSA calculation is given in Eq. (2):

$$ECSA(m^2 g_{Pt}^{-1}) = \frac{Q_H(\mu C cm^{-2}) * 10^{-4}}{210(\mu C cm^{-2}) * Pt\ loading\ (g_{Pt}\ cm^{-2})} \quad (2)$$

Herein, some details are provided on the mechanism of H-adsorption/desorption and factors affecting their measurements. Applying an external potential difference using a potentiostat creates an electric field at the working electrode interface with the electrolyte. In aqueous solutions, protons cannot exist independently and readily combine with the non-binding electron pair of water molecules to form a hydronium ion (H_3O^+). When the hydronium ion reaches the double layer of the electrode, electro-adsorption of the hydrogen (H_{ec-ads})[96], [97] on the Pt surface happens as per the reaction scheme given in Eq. (3) below.



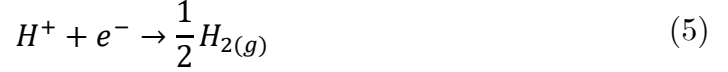
Of the two types of H_{ec-ads} , namely H_{upd} and H_{opd} , the H_{ec-ads} for >0 V charge is attributed to H_{upd} , while that of < 0 V accounts for the H_{opd} (which is a precursor to the HER).

The Nernst equation gives the equilibrium potential at which this reaction occurs (Eq. (4) below):

$$E_e = E^0 + \frac{RT}{zF} \ln (a_{H^+}/a_{H_{ads}}) \quad (4)$$

Where E_e is the equilibrium potential, E^0 is the standard potential, a denotes activity of species, T , R , and F are temperature (K), molar gas constant, and Faraday constant, respectively.

As the potential reaches the equilibrium potential for hydrogen reduction, HER starts. The HER and corresponding Nernst equation is given by Eq. (5) and Eq. (6).



$$E_e = E^0 - \frac{RT}{F} \ln(\sqrt{f_{H_2}}/a_{H^+}) \quad (6)$$

As per Eq. (5), HER is expected to begin at 0.0 V when the f_{H_2} (fugacity) in the compartment is 1 bar. However, when the electrochemical cell is purged with the inert gas, E^0 (H^+/H_2) is displaced to a positive value.[67] Moreover, the scanrate and catalyst can also make the HER shifted to positive potential regime.[16] Therefore, the lower limit for calculating H_{upd} charge in ECSA computations is usually restricted to 0.05 V.[15], [16], [50], [73], [87] This choice ensures that the charges related to competitive HER can be avoided. Unlike hydrogen overpotential deposition (H_{opd}), the onset of H_{upd} is not dependent on f_{H_2} , as it is neither in equilibrium with the dissolved H_2 nor with the $H_{2(g)}$ above the solution. The onset potential of H_{upd} is just related to the proton activity (a_{H^+}) in the electrolyte solution. As such, either H_{upd} adsorption[15], [63], [73], [82] or H_{upd} desorption[50], [74], [98], [99] or the average of the two[7], [72], [84], [100], [101] is considered in the literature for ECSA calculation. The expectation is that the charge adsorbed and desorbed are equivalent at the steady-state.[6] However, a Differential Electrochemical Mass Spectroscopy (DEMS) study[102] carried out to resolve H_{upd} and H_{opd} contributions to the adsorption and desorption region revealed that the adsorption portion of the CV has a significant contribution from both H_{opd}

and H_{upd} . In contrast, the desorption part has a lower contribution as adsorbed H_{opd} is converted to $H_{2(g)}$, which can diffuse out of the system. We compared the charge evaluated from H_{des} (Figure 3.9a) and H_{ads} (Figure 3.9b) to corroborate this. The charge corresponding to H_{ads} part is higher by $>20\%$ than H_{des} part, implying that H_{upd} calculated from H_{ads} region is an overestimate and should be avoided.

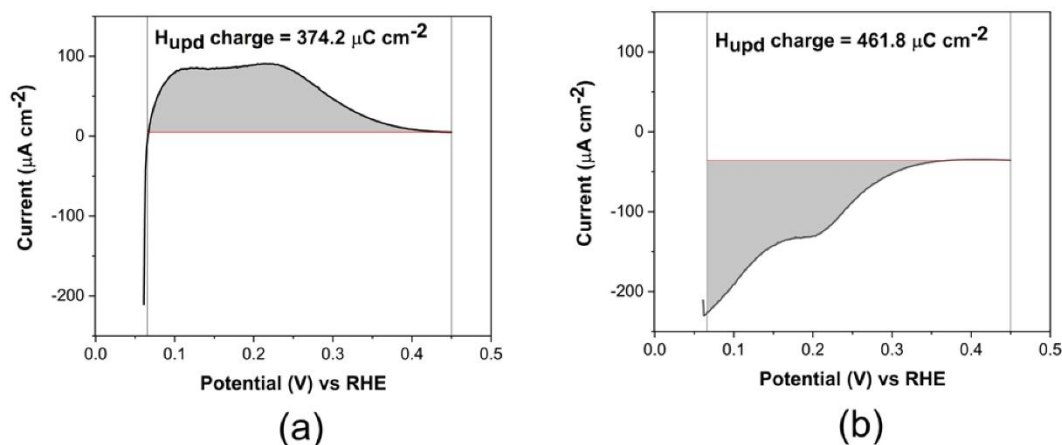


Figure 3.9: Comparison of the H_{upd} charge calculation using (a) H^+ adsorption (b) H^+ desorption regions. CV was carried out in 0.1 M HClO_4 at 50 mV s^{-1} scan rate

Typically, Pt can also leach into the solution at higher potentials,[50] and the extent of leaching varies significantly with the surface structure,[39] which should be taken care of while setting the upper potential limit in the CV. To highlight the effect of scan range, we quantify the effect of increasing the upper potential limit (Figure 3.10(a)) or extending the lower potential limit towards 0 V (Figure 3.10(b)) on H_{upd} charge evaluation (Error! Reference source not found.). The Pt oxide reduction peak shifts towards lower potentials with increased upper potential scan limits, indicating a changed surface composition

comprising several oxides. Such restructuring of the surface by enhanced oxidation and reduction leads to a slightly increased H_{upd} charge, albeit at the cost of increased Pt leaching.[39], [103] Pt forms different oxides at potentials above 1.1 V, and under acidic conditions, these oxides facilitate the dissolution process.[49], [51], [104] Furthermore, Ostwald ripening effect causes larger Pt crystallites to grow further due to the increased dissolution of smaller nanoparticles attributed to their higher surface energy.[57] On the other hand, as the lower potential limit extends towards 0 V, an increase in computed charge is apparent due to H_{opd} .

Table 3.1: Effect of potential limits on computed charge

Potential (V) range vs RHE	Charge between 0.05 V and 0.45 V ($\mu\text{C cm}^{-2}$)
0.06 to 1.26	333.4
0.06 to 1.36	354.9
0.06 to 1.46	366.1
0.03 to 1.26	428.6
0 to 1.26	519.5

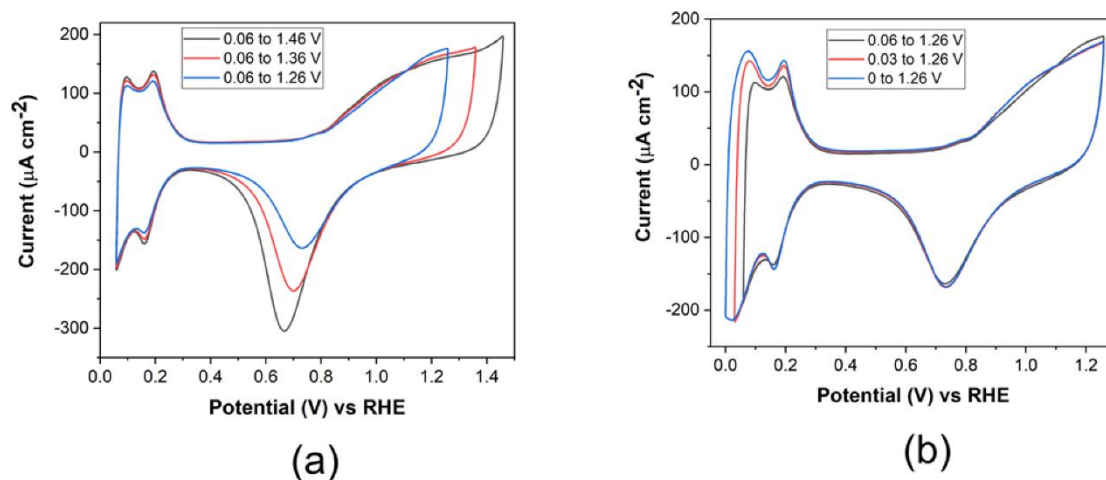


Figure 3.10: Effects of (a) upper and (b) lower potential limits, on H_{upd} region in Pt CV. CVs were carried out in 0.1M HClO_4 at 50 mV s^{-1} scan rate

Scanning to lower potential limits but computing charges by integrating over a smaller range can lead to overestimating H_{upd} by $\sim 10\text{-}30\%$, as shown in Table 3.2. Therefore, this practice is inappropriate as HER contributions will be accounted as H_{upd} .

Table 3.2: Comparison of computed H_{upd} charges for various potential limits and integration limits

Potential and integration limits	H_{upd} charge ($\mu\text{C cm}^{-2}$)
Scanned till 0 V and integrated from 0 V	519.5
Scanned till 0 V and integrated from 0.03 V	498.9
Scanned till 0 V and integrated from 0.06 V	430.6
Scanned till 0.03 V and integrated from 0.03 V	428.8
Scanned till 0.03 V and integrated from 0.06 V	401.0
Scanned till 0.06 V and integrated from 0.06 V	333.4

Scan rates reported in literature[15], [46], [50], [59] for ECSA analysis range from 20 mV s⁻¹ to 100 mV s⁻¹. The peak current height increases with increased scan rate due to reduced diffusion layer thickness[105], and Randle-Sevcik Equation relates peak currents – wherein measured current is proportional to the square root of scan rate. The variation in currents with scan rates can be misconstrued as higher activity at higher scan rates. But, H_{upd} charge is a normalized measure, taking account of scan rate. To illustrate this, we compute H_{upd} charge for different scan rates and show that they have less than 5% variation (Table 3.3). With the increased scan rate, the concentration gradient takes longer to react to the potential change. PtO reduction peak, owing to its irreversible nature, shifts from 0.8 V at lower scan rates towards lower values for higher scan rates (Figure 3.11); thereby, increasing the separation between the onset of oxidation of Pt and the corresponding PtO reduction.

Table 3.3: Effect of scan rate on H_{upd} charge

Scan rate (mV s ⁻¹)	H _{upd} charge (μC cm ⁻²)
200	295.8
100	312.2
50	313.4
20	309.6
10	296.4

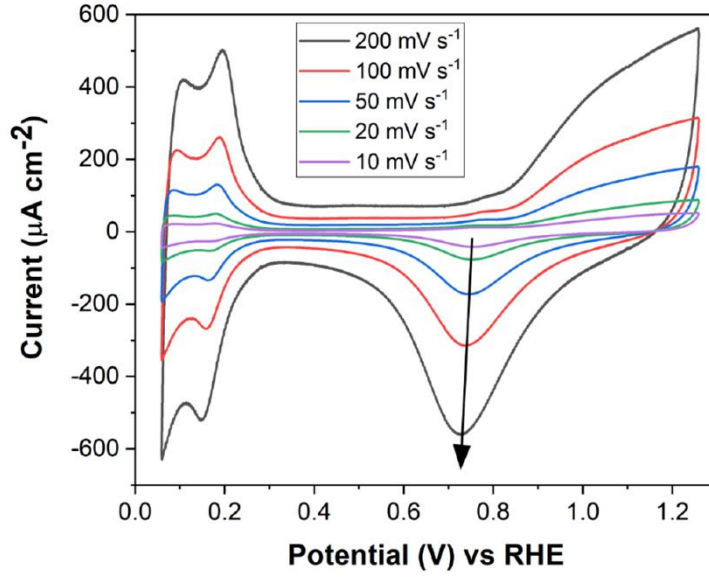


Figure 3.11: Variation in H_{upd} charge with potential scan rates. CVs were carried out in 0.1M HClO_4 at 5 mV s^{-1}

3.5.2 Double layer charging (or capacitance) region

When the working electrode's potential is changed, two kinds of currents can flow: 1) Faradaic current corresponding to oxidation or reduction. 2) Capacitive/non-Faradaic current related to the charge separation due to the ionic layer at the working electrode/electrolyte interfacial region. Capacitive currents are not related to electron transport across the electrode/electrolyte interface but are a transient flow of a balancing current.[106]

The mathematical model of the double layer is (Eq. (7)):

$$C_d = dQ/dV = i \cdot dt/dV = i/(dV/dt) \quad (7)$$

Where i is the measured current and $\frac{dV}{dt}$ is the potential scan rate

The central region in a Pt CV, typically aligned parallel to the voltage-axis, corresponds to a double layer charging regime when the current is almost constant with no electron transfer across the electrode/electrolyte interface (between $\sim 0.3-0.5$ V and $\sim 0.7-0.8$ V. Note: The range of double layer is influenced by the pH and type and concentration of anions in the electrolyte). In the context of Figure 3.1, the raising/lowering of the electrode Fermi level through this region does not lead to overlap with redox potentials of species present in the electrolyte. Several factors like the electrode area, catalyst material,[7] catalyst loading, and scan rate[107] influence the capacitive current.[108] A high background current during double layer charging can also be related to impurities in the electrolyte. As such, this double-layer charging is present across the entire potential range and is frequently, though debatably, taken to be constant in the whole potential range.[108] Usually, the capacitance value for a smooth electrode/electrolyte interface is $\sim 20 \mu\text{F cm}^{-2}$. [109] However, this value increases by orders of magnitude for high- surface-area electrodes,[6], [15], [110] leading to difficulties in characterizing the H_{upd} charge values for ultra-low Pt loaded ($<1\%$ Pt) catalysts, metal oxide supports,[111] and Pt alloys.[112] In these cases, estimations from H_{upd} will be underestimated and CO stripping or Cu_{upd} method can be more accurate.[113]

3.5.3 Pt surface oxidation and reduction ($> \sim 0.7-0.8$ V)

Pt forms various oxides during the positive scan above $\sim 0.7-0.8$ V, which are correspondingly reduced in the negative scan (till ~ 0.65 V). The shapes and the area ratio of the oxide formation and reduction peak are characteristic of irreversible reactions. The Pt oxide formation is a multi-step process ranging

from $\sim 0.7-0.8$ V to 1.4 V,[114] with its main product as PtO and some PtO₂. [115] The oxide formation happens in three steps; [114] the first is the oxidation of the H₂O molecule to OH_{ads} (to form Pt₄OH, Pt₃OH, and Pt₂OH species). The second step is developing a quasi-3-D lattice due to the interfacial place exchange between the surface Pt atoms and OH_{ads}. The last stage represents the oxidation of the OH within the quasi-3D lattice, resulting in Pt-O formation. We speculate that the usual practice to scan up to an upper limit of 1.2 V strikes a balance between Pt restructuring through oxide formation and Pt leaching. Due to the overlap of multiple peaks corresponding to different oxidized Pt species, the CV appears to be a series of ‘shoulders’.

3.6 Precautions to be undertaken while conducting durability experiments

In this section, we share our learning on ex-situ durability analysis from our experiments on atomic layered Pt, synthesized via the self-terminating electrodeposition protocol [116] on e-beam evaporated gold films (The details of the synthesis are included in chapter 4).

3.6.1 Importance of using a fresh electrolyte for each sample synthesis

Although Pt deposited in any run is only a negligible fraction of the electrolyte's total Pt content, the reuse of electrolyte for another sample preparation must be avoided. Since the synthesis conditions such as pH and double layer termination might differ, there can be a drastic change in the electrochemical activities of samples formed by reusing electrolytes. Figure 3.12a compares the electrochemical activity of the samples synthesized using the same electrolyte (sample 1 followed by sample 2) with that of Figure 3.12b, where a fresh

electrolyte was used for each sample. The use of a freshly prepared solution leads to repeatable results. This requirement will adversely impact the suitability of self-terminating electrodeposition as an additive process for large-scale manufacture and is a matter for further investigation.

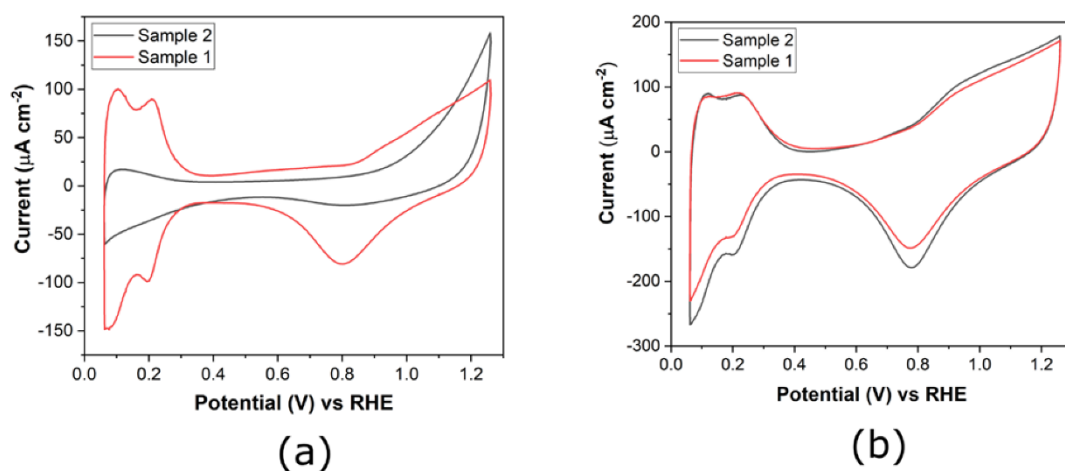


Figure 3.12: CVs of Pt films synthesized by (a) reusing electrolyte and (b) by using fresh electrolyte for the two samples. CVs were carried out in 0.1M HClO₄ at 50 mV s⁻¹

3.6.2 Importance of a proper inert gas purging setup

A proper inert gas atmosphere must be created during the durability analysis apart from thoroughly purging the HClO₄ electrolyte with inert gas for at least 30 min. The electrolyte level should be such that inert gas flow does not perturb it; otherwise, it leads to fluctuations in the CV as shown in Figure 3.13(a) and Figure 3.13(b).

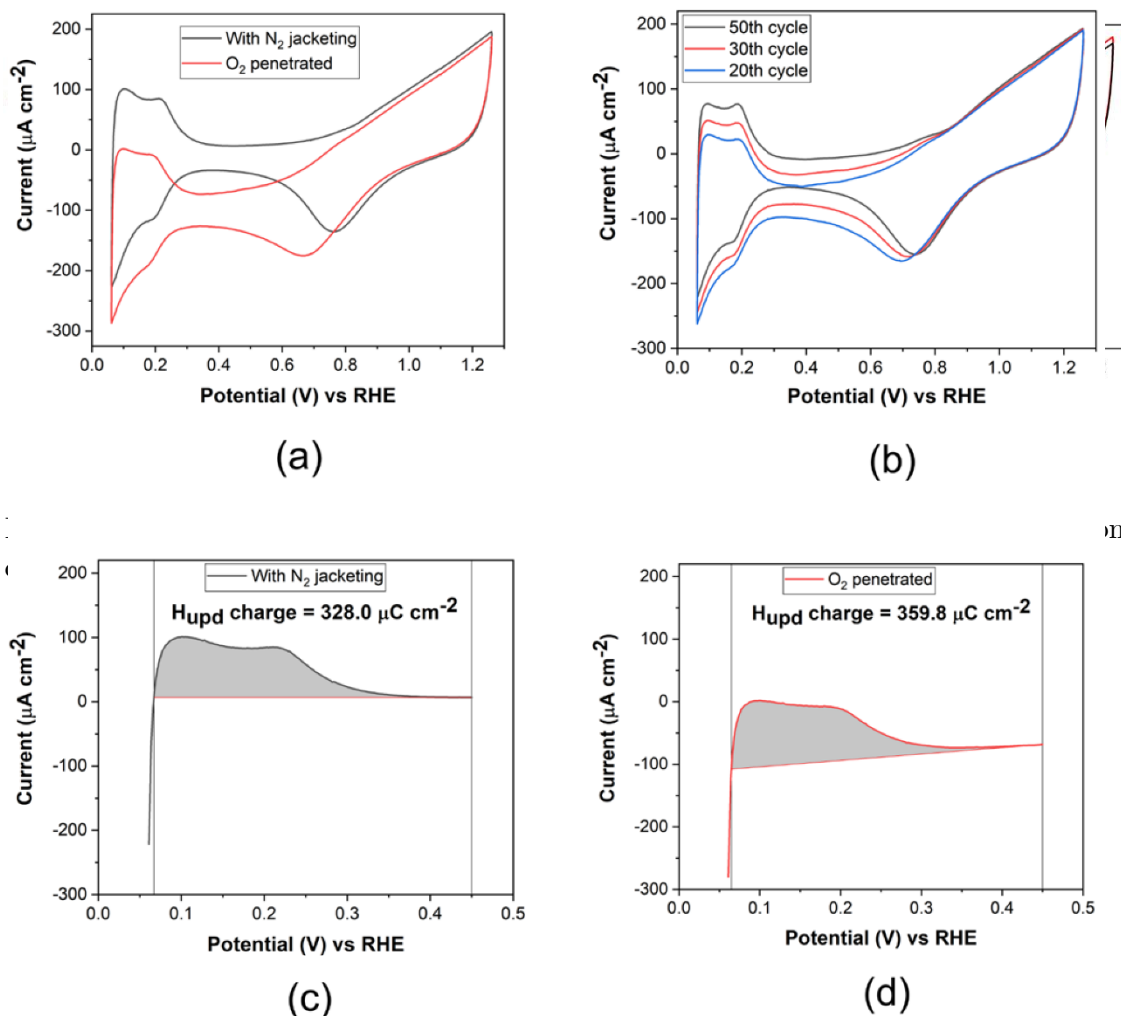


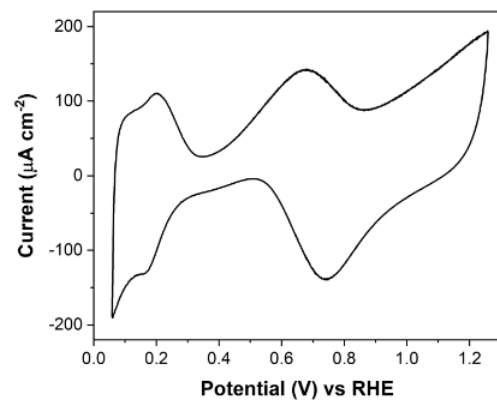
Figure 3.14: Effect of improper inert gas purging on the CV profile: (a) effect of the dissolved O₂ on the CV (b) effect of O₂ in the added electrolyte during ex-situ durability analysis (c and d) Difference in the H_{upd} values for CV with inert gas jacketing (without dissolved O₂) and with dissolved O₂. CVs were carried in 0.1 M HClO₄ at 50 mV s⁻¹ scan rate

Figure 3.14a shows how the disruption of the inert gas blanket can lead to diffusion of atmospheric O₂ inside the electrochemical cell, which changes the shape of the Pt CV due to undesirable current associated with O₂ reduction reaction (ORR).[117] Figure 3.14b shows how adding makeup

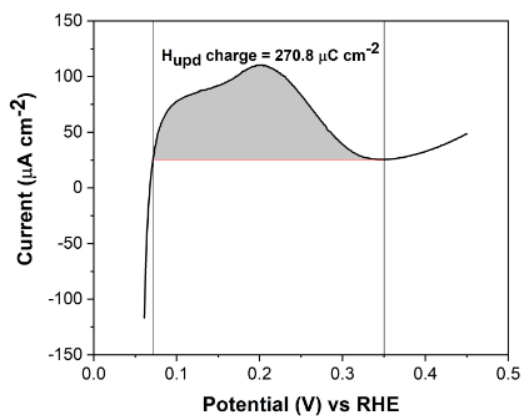
electrolyte without inert gas purging during durability analysis can give additional current corresponding to ORR, which decreases with the number of CV cycles. It is challenging to fix an objective baseline for H_{upd} calculations in such CVs. A comparison of Figure 3.14c and Figure 3.14d indicates that the H_{upd} charge value estimated using a slanted baseline is $\sim 10\%$ more than that for a flat baseline.

As a good practice, marking the working electrode's initial height on the electrochemical cell wall and maintaining the same throughout the durability analysis helps ensure that the electrode's immersed area and electrolyte concentration are constant. The working electrode should fit snugly on the electrochemical cell cap. It should not be dislodged due to pressure rise from the inert gas blanketing. Also, using organic solvents to clean the working electrode before the durability analysis should be performed carefully. Even a trace of leftover organic can alter the CV.

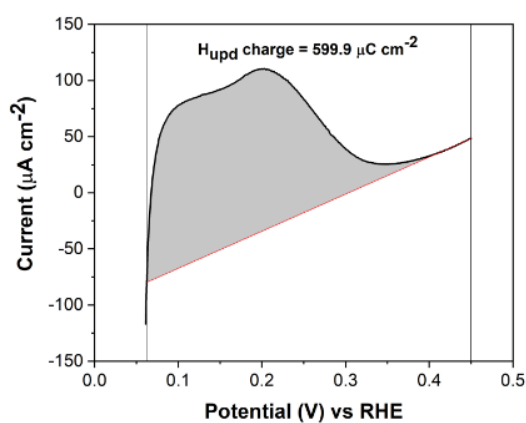
As shown in Figure 3.15a, the oxidation peak in the anodic potential range of 0.6 to 0.8 V is associated with the oxidation of organic solvents (used for cleaning the glassware or the electrodes) into carbon monoxide (CO). Due to CO oxidation, the H_{upd} region has a slant towards the end in the anodic H_{upd} part. Figure 3.15b and Figure 3.15c indicate that the ECSA calculated using a slanted baseline is $\sim 80\%$ more than that calculated using a flat baseline. As such, the H_{upd} values are very sensitive to the choices of the baseline corrections.



(a)



(b)



(c)

Figure 3.15: (a) Effect of organic residues from IPA cleaning before CV, (b) and (c) H_{upd} charge analysis using flat and slanted baseline

3.7 Anticipated improvement in skillset

Following the protocols, guidelines, and safeguards outlined in this article, one can develop the necessary skill set to perform CV and estimate ECSA from *ex-situ* durability analysis. Figure 3.16 is an example of such progress. The aligned CVs can better quantify the trends in degradation of Pt electrocatalyst during the ex-situ durability analysis. In contrast, erroneous H_{upd} trends arise during durability analysis if prudent practices are not followed (compare insets of Figure 3.16a and Figure 3.16b). Moreover, due to reproducible scans across different samples obtained using the prudent practices outlined above, it is possible to compute mean and standard deviations for ECSA values from three different samples.

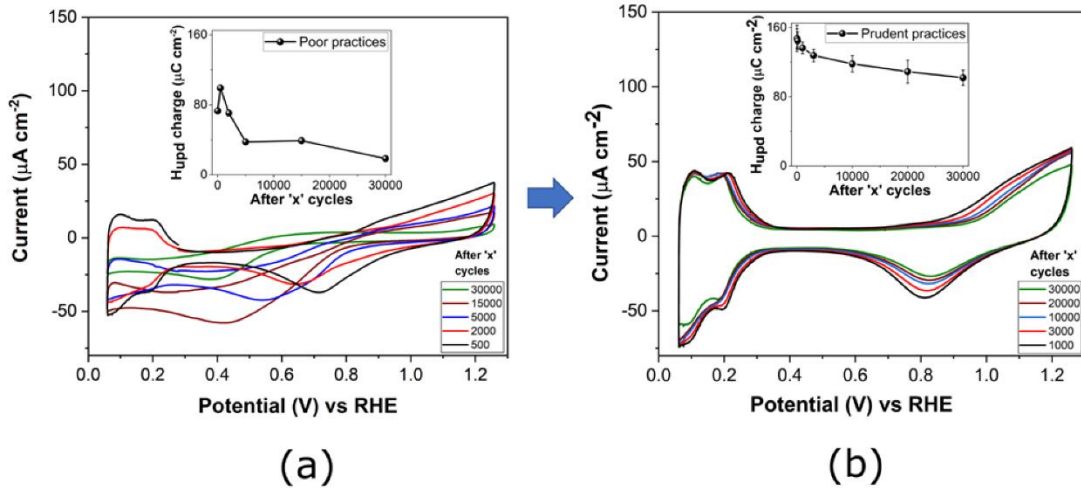


Figure 3.16: Ex-situ durability analysis with (a) poor practices (b) prudent practices. Insets show corresponding trends for computed H_{upd} charges. Note, average values from three samples are used to evaluate the trend in the inset of panel b.

3.8 Summary and outlook

We highlighted the critical experimental details for accurately carrying out ECSA estimation through H_{upd} charge measurement during the lengthy ex-situ durability analysis. We discussed the necessary background concepts from electrochemistry and correlated them to the execution of CV experiments. We described the features in different regions of a Pt CV and analysed the reasons behind the typical profile. We addressed critical yet straightforward issues from a beginner’s perspective, such as the significance of input parameters, the effect of using a fresh electrolyte during the synthesis, and points to be considered while putting together the electrochemical setup. We compiled and demonstrated, through our experiments, the effective practices such as the importance of proper cleaning and pre-treatment protocols for the electrodes, choice of electrolyte, and inert gas purging, the influence of scan range and scan rate on Pt CV profile and H_{upd} values. Finally, by sharing our experience on effective practices for CV measurement, we hope to benefit the wider community involved in electrocatalyst development and testing. By adequately following the protocols, safeguards, and details on data analysis outlined in this article, one can acquire CVs that are repeatable across samples and make a conclusive assessment of electrochemical activity during the lengthy ex-situ durability analysis.

3.9 References

- [1] F. Harnisch and S. Freguia, "A Basic Tutorial on Cyclic Voltammetry for the Investigation of Electroactive Microbial Biofilms," *Chem. - An Asian J.*, vol. 7, no. 3, pp. 466–475, Mar. 2012, doi: 10.1002/asia.201100740.
- [2] I. Takahashi and S. S. Kocha, "Examination of the activity and durability of PEMFC catalysts in liquid electrolytes," *J. Power Sources*, vol. 195, no. 19, pp. 6312–6322, Oct. 2010, doi: 10.1016/j.jpowsour.2010.04.052.
- [3] J. T. H. Kwan, A. Bonakdarpour, G. Afonso, and D. P. Wilkinson, "Bridging Fundamental Electrochemistry with Applied Fuel Cell Testing: A Novel and Economical Rotating Disk Electrode Tip for Electrochemical Assessment of Catalyst-Coated Membranes," *Electrochim. Acta*, vol. 258, pp. 208–219, Dec. 2017, doi: 10.1016/j.electacta.2017.10.087.
- [4] V. Parrondo, J., Han, T., Niangar, E., Wang, C., Dale, N., Adjemian, K., and Ramani, "Platinum supported on titanium-ruthenium oxide is a remarkably stable electrocatalyst for hydrogen fuel cell vehicles," *Proc. Natl. Acad. Sci.*, vol. 111, no. 1, pp. 45–50, Jan. 2014, doi: 10.1073/pnas.1319663111.
- [5] I. T. McCrum and M. J. Janik, "Deconvoluting Cyclic Voltammograms To Accurately Calculate Pt Electrochemically Active Surface Area," *J. Phys. Chem. C*, vol. 121, no. 11, pp. 6237–6245, Mar. 2017, doi: 10.1021/acs.jpcc.7b01617.
- [6] T. Binninger, E. Fabbri, R. Kötz, and T. J. Schmidt, "Determination of the Electrochemically Active Surface Area of Metal-Oxide Supported Platinum Catalyst," *J. Electrochem. Soc.*, vol. 161, no. 3, pp. H121–H128, 2014, doi: 10.1149/2.055403jes.
- [7] Y. Xing, "Synthesis and Electrochemical Characterization of Uniformly-Dispersed High Loading Pt Nanoparticles on Sonochemically-Treated Carbon Nanotubes," *J. Phys. Chem. B*, vol. 108, no. 50, pp. 19255–19259, Dec. 2004, doi: 10.1021/jp046697i.
- [8] H. A. Gasteiger, J. E. Panels, and S. G. Yan, "Dependence of PEM fuel cell performance on catalyst loading," *J. Power Sources*, vol. 127, no. 1–2, pp. 162–171, Mar. 2004, doi: 10.1016/j.jpowsour.2003.09.013.
- [9] N. Tian, Z.-Y. Zhou, S.-G. Sun, Y. Ding, and Z. L. Wang, "Synthesis of Tetrahedral Platinum Nanocrystals with High-Index Facets and High Electro-Oxidation Activity," *Science*, vol. 316, no. 5825, pp. 732–735, May 2007, doi: 10.1126/science.1140484.
- [10] J. Greeley *et al.*, "Alloys of platinum and early transition metals as oxygen reduction electrocatalysts," *Nat. Chem.*, vol. 1, no. 7, pp. 552–556, Oct. 2009, doi: 10.1038/nchem.367.
- [11] H. R. Colón-Mercado, H. Kim, and B. N. Popov, "Durability study of Pt₃Ni₁ catalysts as cathode in PEM fuel cells," *Electrochem. commun.*, vol. 6, no. 8, pp.

- 795–799, Aug. 2004, doi: 10.1016/j.elecom.2004.05.028.
- [12] C. Wei *et al.*, “Recommended Practices and Benchmark Activity for Hydrogen and Oxygen Electrocatalysis in Water Splitting and Fuel Cells,” *Adv. Mater.*, vol. 31, no. 31, p. 1806296, Aug. 2019, doi: 10.1002/adma.201806296.
 - [13] C. Wei, S. Sun, D. Mandler, X. Wang, S. Z. Qiao, and Z. J. Xu, “Approaches for measuring the surface areas of metal oxide electrocatalysts for determining their intrinsic electrocatalytic activity,” *Chem. Soc. Rev.*, vol. 48, no. 9, pp. 2518–2534, 2019, doi: 10.1039/C8CS00848E.
 - [14] S. S. Kocha *et al.*, “Best Practices and Testing Protocols for Benchmarking ORR Activities of Fuel Cell Electrocatalysts Using Rotating Disk Electrode,” *Electrocatalysis*, vol. 8, no. 4, pp. 366–374, 2017, doi: 10.1007/s12678-017-0378-6.
 - [15] K. J. J. Mayrhofer, D. Strmcnik, B. B. Blizanac, V. Stamenkovic, M. Arenz, and N. M. Markovic, “Measurement of oxygen reduction activities via the rotating disc electrode method: From Pt model surfaces to carbon-supported high surface area catalysts,” *Electrochim. Acta*, vol. 53, no. 7, pp. 3181–3188, Feb. 2008, doi: 10.1016/j.electacta.2007.11.057.
 - [16] Y. Garsany, O. A. Baturina, K. E. Swider-Lyons, and S. S. Kocha, “Experimental Methods for Quantifying the Activity of Platinum Electrocatalysts for the Oxygen Reduction Reaction,” *Anal. Chem.*, vol. 82, no. 15, pp. 6321–6328, Aug. 2010, doi: 10.1021/ac100306c.
 - [17] N. Garland, T. Benjamin, and J. Kopasz, “DOE Fuel Cell Program: Durability Technical Targets and Testing Protocols,” *ECS Trans.*, vol. 11, no. 1, pp. 923–931, Sep. 2007, doi: 10.1149/1.2781004.
 - [18] “Fuel Cell Technologies Office, Multi-Year Research, Development, and Demonstration Plan,” 2017. [Online]. Available: https://www.energy.gov/sites/default/files/2017/05/f34/fcto_myrrdd_fuel_cells.pdf (Accessed on 23rd May, 2021).
 - [19] M. M. Mench, E. C. Kumbur, and T. N. Veziroglu, *Polymer Electrolyte Fuel Cell Degradation*. MA, USA, 2012.
 - [20] S. S. Kocha, Y. Garsany, and D. Myers, “Testing Oxygen Reduction Reaction Activity with the Rotating Disc Electrode Technique,” 2013, [Online]. Available: https://www.energy.gov/sites/default/files/2014/03/f12/webinarslides_rde_technique_031213.pdf (Accessed on 21st April, 2021).
 - [21] P. Peljo and H. H. Girault, “Electrochemical potential window of battery electrolytes: the HOMO–LUMO misconception,” *Energy Environ. Sci.*, vol. 11, no. 9, pp. 2306–2309, 2018, doi: 10.1039/C8EE01286E.
 - [22] J. O. Bockris, A. K. N. Reddy, and M. G. Aldeco, *Modern Electrochemistry 2A - Fundamentals of Electrodicts*, 2nd ed. New York, United States: KLUWER

ACADEMIC, 2002.

- [23] N. Elgrishi, K. J. Rountree, B. D. McCarthy, E. S. Rountree, T. T. Eisenhart, and J. L. Dempsey, "A Practical Beginner's Guide to Cyclic Voltammetry," *J. Chem. Educ.*, vol. 95, no. 2, pp. 197–206, Feb. 2018, doi: 10.1021/acs.jchemed.7b00361.
- [24] P. T. Kissinger and W. R. Heineman, *Laboratory Techniques in Electroanalytical Chemistry*, 2nd ed. Marcel Dekkar, New York, US, 1996.
- [25] C. Sandford *et al.*, "A synthetic chemist's guide to electroanalytical tools for studying reaction mechanisms," *Chem. Sci.*, vol. 10, no. 26, pp. 6404–6422, 2019, doi: 10.1039/C9SC01545K.
- [26] A. J. Bard and L. R. Faulkner, *Electrochemical Methods: Fundamentals and Applications*, 2nd ed. New York, US: John Wiley & Sons, Inc., 2001.
- [27] R. E. Treybal, *Mass Transfer Operations*, 3rd ed. McGraw-Hill Book Company, Singapore, 1980.
- [28] C. M. A. Brett and A. M. O. Brett, *Electrochemistry: Principles, Methods, And Applications*, 1st ed. Oxford University Press Inc., New York, US, 1993.
- [29] R. H. Dahm and R. J. Latham, "The Potentiostat and its Applications," *Trans. IMF*, vol. 71, no. 2, pp. 77–79, Jan. 1993, doi: 10.1080/00202967.1993.11870993.
- [30] G. Jerkiewicz, "Standard and Reversible Hydrogen Electrodes: Theory, Design, Operation, and Applications," *ACS Catal.*, vol. 10, no. 15, pp. 8409–8417, Aug. 2020, doi: 10.1021/acscatal.0c02046.
- [31] F. J. Perez-Alonso *et al.*, "The Effect of Size on the Oxygen Electroreduction Activity of Mass-Selected Platinum Nanoparticles," *Angew. Chemie Int. Ed.*, vol. 51, no. 19, pp. 4641–4643, May 2012, doi: 10.1002/anie.201200586.
- [32] K. Ke, K. Hiroshima, Y. Kamitaka, T. Hatanaka, and Y. Morimoto, "An accurate evaluation for the activity of nano-sized electrocatalysts by a thin-film rotating disk electrode: Oxygen reduction on Pt/C," *Electrochim. Acta*, vol. 72, pp. 120–128, 2012, doi: 10.1016/j.electacta.2012.04.004.
- [33] H. Angerstein-Kozłowska, B. E. Conway, and W. B. A. Sharp, "The real condition of electrochemically oxidized platinum surfaces," *J. Electroanal. Chem. Interfacial Electrochem.*, vol. 43, no. 1, pp. 9–36, Apr. 1973, doi: 10.1016/S0022-0728(73)80307-9.
- [34] A. Damjanovic, M. A. Genshaw, and J. O. Bockris, "The Role of Hydrogen Peroxide in Oxygen Reduction at Platinum in H₂SO₄ Solution," *J. Electrochem. Soc.*, vol. 114, no. 5, p. 466, Nov. 1967, doi: 10.1149/1.2426629.
- [35] D. Chu, D. Tryk, D. Gervasio, and E. B. Yeager, "Examination of the ionomer/electrode interface using the ferric/ferrous redox couple," *J. Electroanal. Chem. Interfacial Electrochem.*, vol. 272, no. 1–2, pp. 277–284, Nov. 1989, doi: 10.1016/0022-0728(89)87089-5.

- [36] O. J. Curnick, B. G. Pollet, and P. M. Mendes, "Nafion®-stabilised Pt/C electrocatalysts with efficient catalyst layer ionomer distribution for proton exchange membrane fuel cells," *RSC Adv.*, vol. 2, no. 22, pp. 8368–8374, 2012, doi: 10.1039/c2ra21071a.
- [37] C. M. Zalitis, D. Kramer, and A. R. Kucernak, "Electrocatalytic performance of fuel cell reactions at low catalyst loading and high mass transport," *Phys. Chem. Chem. Phys.*, vol. 15, no. 12, p. 4329, 2013, doi: 10.1039/c3cp44431g.
- [38] K. Shinozaki, J. W. Zack, S. Pylypenko, B. S. Pivovar, and S. S. Kocha, "Oxygen Reduction Reaction Measurements on Platinum Electrocatalysts Utilizing Rotating Disk Electrode Technique. II. Influence of Ink Formulation, Catalyst Layer Uniformity and Thickness," *J. Electrochem. Soc.*, vol. 162, no. 12, pp. F1384–F1396, Sep. 2015, doi: 10.1149/2.0551512jes.
- [39] P. J. Ferreira *et al.*, "Instability of Pt/C Electrocatalysts in Proton Exchange Membrane Fuel Cells," *J. Electrochem. Soc.*, vol. 152, no. 11, p. A2256, Nov. 2005, doi: 10.1149/1.2050347.
- [40] D. Wang *et al.*, "Structurally ordered intermetallic platinum–cobalt core–shell nanoparticles with enhanced activity and stability as oxygen reduction electrocatalysts," *Nat. Mater.*, vol. 12, no. 1, pp. 81–87, Jan. 2013, doi: 10.1038/nmat3458.
- [41] S. D. James, "The Electrochemical Activation of Platinum Electrodes," *J. Electrochem. Soc.*, vol. 114, no. 11, pp. 1113–1119, 1967, doi: 10.1149/1.2426426.
- [42] S. Shibata and M. P. Sumino, "Electrochemical activity of electrodeposited and heat-treated platinum electrodes," *Electrochim. Acta*, vol. 16, no. 9, pp. 1511–1517, 1971, doi: 10.1016/0013-4686(71)80021-X.
- [43] W. G. French and T. Kuwana, "Lifetime of Activated Platinum Surface," *J. Phys. Chem.*, vol. 68, no. 6, pp. 1279–1284, Jun. 1964, doi: 10.1021/j100788a003.
- [44] J. Lee, D. W. M. Arrigan, and D. S. Silvester, "Achievement of Prolonged Oxygen Detection in Room-Temperature Ionic Liquids on Mechanically Polished Platinum Screen-Printed Electrodes," *Anal. Chem.*, vol. 88, no. 10, pp. 5104–5111, May 2016, doi: 10.1021/acs.analchem.5b04782.
- [45] F. J. Vidal-Iglesias, R. M. Arán-Ais, J. Solla-Gullón, E. Herrero, and J. M. Feliu, "Electrochemical Characterization of Shape-Controlled Pt Nanoparticles in Different Supporting Electrolytes," *ACS Catal.*, vol. 2, no. 5, pp. 901–910, May 2012, doi: 10.1021/cs200681x.
- [46] M. Li *et al.*, "Ultrafine jagged platinum nanowires enable ultrahigh mass activity for the oxygen reduction reaction," *Science*, vol. 354, no. 6318, pp. 1414–1419, Dec. 2016, doi: 10.1126/science.aaf9050.
- [47] U. A. Paulus, T. J. Schmidt, H. A. Gasteiger, and R. J. Behm, "Oxygen reduction on a high-surface area Pt/Vulcan carbon catalyst: a thin-film rotating

- ring-disk electrode study,” *J. Electroanal. Chem.*, vol. 495, no. 2, pp. 134–145, Jan. 2001, doi: 10.1016/S0022-0728(00)00407-1.
- [48] J. Durst, C. Simon, F. Hasché, and H. A. Gasteiger, “Hydrogen Oxidation and Evolution Reaction Kinetics on Carbon Supported Pt, Ir, Rh, and Pd Electrocatalysts in Acidic Media,” *J. Electrochem. Soc.*, vol. 162, no. 1, pp. F190–F203, Dec. 2015, doi: 10.1149/2.0981501jes.
- [49] J. N. Schwämmlein, G. S. Harzer, P. Pfändner, A. Blankenship, H. A. El-Sayed, and H. A. Gasteiger, “Activity and Stability of Carbon Supported Pt_xY Alloys for the ORR Determined by RDE and Single-Cell PEMFC Measurements,” *J. Electrochem. Soc.*, vol. 165, no. 15, pp. J3173–J3185, Oct. 2018, doi: 10.1149/2.0221815jes.
- [50] O. A. Baturina, B. D. Gould, Y. Garsany, and K. E. Swider-Lyons, “Insights on the SO₂ poisoning of Pt₃Co/VC and Pt/VC fuel cell catalysts,” *Electrochim. Acta*, vol. 55, no. 22, pp. 6676–6686, Sep. 2010, doi: 10.1016/j.electacta.2010.06.004.
- [51] A. A. Topalov, S. Cherevko, A. R. Zeradjanin, J. C. Meier, I. Katsounaros, and K. J. J. Mayrhofer, “Towards a comprehensive understanding of platinum dissolution in acidic media,” *Chem. Sci.*, vol. 5, no. 2, pp. 631–638, 2014, doi: 10.1039/C3SC52411F.
- [52] M. J. Watt-Smith, J. M. Friedrich, S. P. Rigby, T. R. Ralph, and F. C. Walsh, “Determination of the electrochemically active surface area of Pt/C PEM fuel cell electrodes using different adsorbates,” *J. Phys. D: Appl. Phys.*, vol. 41, no. 17, p. 174004, Sep. 2008, doi: 10.1088/0022-3727/41/17/174004.
- [53] R. Latsuzbaia, E. Negro, and G. Koper, “Synthesis, Stabilization and Activation of Pt Nanoparticles for PEMFC Applications,” *Fuel Cells*, vol. 15, no. 4, pp. 628–638, Aug. 2015, doi: 10.1002/face.201500023.
- [54] J. R. Smith, S. A. Campbell, and F. C. Walsh, “Cyclic Voltammetry at Metal Electrodes,” *Trans. IMF*, vol. 73, no. 2, pp. 72–78, Jan. 1995, doi: 10.1080/00202967.1995.11871062.
- [55] J. W. Burgman, J. A. Leistra, and P. J. Sides, “Aluminum/Cryolite Reference Electrodes for Use in Cryolite-Based Melts,” *J. Electrochem. Soc.*, vol. 133, no. 3, pp. 496–500, Mar. 1986, doi: 10.1149/1.2108608.
- [56] C. G. Zoski, *Handbook of Electrochemistry*, 1st ed. Elsevier: Amsterdam, The Netherlands, 2007.
- [57] K. Kinoshita, J. T. Lundquist, and P. Stonehart, “Potential cycling effects on platinum electrocatalyst surfaces,” *J. Electroanal. Chem. Interfacial Electrochem.*, vol. 48, no. 2, pp. 157–166, Nov. 1973, doi: 10.1016/S0022-0728(73)80257-8.
- [58] J. Clavilier, R. Faure, G. Guinet, and R. Durand, “Preparation of

- monocrystalline Pt microelectrodes and electrochemical study of the plane surfaces cut in the direction of the $\{111\}$ and $\{110\}$ planes,” *J. Electroanal. Chem. Interfacial Electrochem.*, vol. 107, no. 1, pp. 205–209, Feb. 1980, doi: 10.1016/S0022-0728(79)80022-4.
- [59] B. A. Larsen *et al.*, “Platinum Nanoplates as Fuel Cell Electrocatalysts,” *J. Electrochem. Soc.*, vol. 159, no. 10, pp. F622–F627, Jan. 2012, doi: 10.1149/2.029210jes.
- [60] M. . Tavares, S. A. . Machado, and L. . Mazo, “Study of hydrogen evolution reaction in acid medium on Pt microelectrodes,” *Electrochim. Acta*, vol. 46, no. 28, pp. 4359–4369, Aug. 2001, doi: 10.1016/S0013-4686(01)00726-5.
- [61] M. C. Santos and L. O. S. Bulhões, “The underpotential deposition of Sn on Pt in acid media. Cyclic voltammetric and electrochemical quartz crystal microbalance studies,” *Electrochim. Acta*, vol. 48, no. 18, pp. 2607–2614, Aug. 2003, doi: 10.1016/S0013-4686(03)00304-9.
- [62] C. F. Zinola and J. Rodriguez, “Tin underpotential deposition on platinum and its catalytic influence on the kinetics of molecular oxygen electroreduction,” *J. Solid State Electrochem.*, vol. 6, no. 6, pp. 412–419, Aug. 2002, doi: 10.1007/s100080100242.
- [63] S. Rudi, C. Cui, L. Gan, and P. Strasser, “Comparative Study of the Electrocatalytically Active Surface Areas (ECSAs) of Pt Alloy Nanoparticles Evaluated by H_{upd} and CO-stripping voltammetry,” *Electrocatalysis*, vol. 5, no. 4, pp. 408–418, Oct. 2014, doi: 10.1007/s12678-014-0205-2.
- [64] D. Chen, Q. Tao, L. W. Liao, S. X. Liu, Y. X. Chen, and S. Ye, “Determining the Active Surface Area for Various Platinum Electrodes,” *Electrocatalysis*, vol. 2, no. 3, pp. 207–219, Sep. 2011, doi: 10.1007/s12678-011-0054-1.
- [65] C. L. Green and A. Kucernak, “Determination of the Platinum and Ruthenium Surface Areas in Platinum–Ruthenium Alloy Electrocatalysts by Underpotential Deposition of Copper. I. Unsupported Catalysts,” *J. Phys. Chem. B*, vol. 106, no. 5, pp. 1036–1047, Feb. 2002, doi: 10.1021/jp0131931.
- [66] P. Daubinger, J. Kieninger, T. Unmüssig, and G. A. Urban, “Electrochemical characteristics of nanostructured platinum electrodes – a cyclic voltammetry study,” *Phys. Chem. Chem. Phys.*, vol. 16, no. 18, pp. 8392–8399, 2014, doi: 10.1039/C4CP00342J.
- [67] G. Jerkiewicz, “Electrochemical Hydrogen Adsorption and Absorption. Part 1: Under-potential Deposition of Hydrogen,” *Electrocatalysis*, vol. 1, no. 4, pp. 179–199, Dec. 2010, doi: 10.1007/s12678-010-0022-1.
- [68] D. B. Sepa, M. V. Vojnovic, and A. Damjanovic, “Reaction intermediates as a controlling factor in the kinetics and mechanism of oxygen reduction at platinum electrodes,” *Electrochim. Acta*, vol. 26, no. 6, pp. 781–793, Jun. 1981, doi:

- 10.1016/0013-4686(81)90037-2.
- [69] S. L. Gojković, S. K. Zečević, and R. F. Savinell, "O₂ Reduction on an Ink-Type Rotating Disk Electrode Using Pt Supported on High-Area Carbons," *J. Electrochem. Soc.*, vol. 145, no. 11, pp. 3713–3720, Nov. 1998, doi: 10.1149/1.1838864.
 - [70] Z. Yang, T. Fujigaya, and N. Nakashima, "A phosphoric acid-doped electrocatalyst supported on poly(para-pyridine benzimidazole)-wrapped carbon nanotubes shows a high durability and performance," *J. Mater. Chem. A*, vol. 3, no. 27, pp. 14318–14324, 2015, doi: 10.1039/C5TA01650A.
 - [71] D. Wang *et al.*, "Facile Synthesis of Carbon-Supported Pd–Co Core–Shell Nanoparticles as Oxygen Reduction Electrocatalysts and Their Enhanced Activity and Stability with Monolayer Pt Decoration," *Chem. Mater.*, vol. 24, no. 12, pp. 2274–2281, Jun. 2012, doi: 10.1021/cm203863d.
 - [72] Y. Li and Y. Huang, "Morphology-Controlled Synthesis of Platinum Nanocrystals with Specific Peptides," *Adv. Mater.*, vol. 22, no. 17, pp. 1921–1925, May 2010, doi: 10.1002/adma.200903944.
 - [73] F. Fouda-Onana, N. Guillet, and A. M. AlMayouf, "Modified pulse electrodeposition of Pt nanocatalyst as high-performance electrode for PEMFC," *J. Power Sources*, vol. 271, pp. 401–405, Dec. 2014, doi: 10.1016/j.jpowsour.2014.08.031.
 - [74] D. A. Stevens and J. R. Dahn, "Electrochemical Characterization of the Active Surface in Carbon-Supported Platinum Electrocatalysts for PEM Fuel Cells," *J. Electrochem. Soc.*, vol. 150, no. 6, p. A770, 2003, doi: 10.1149/1.1573195.
 - [75] W. Zhu *et al.*, "Buckypaper-based catalytic electrodes for improving platinum utilization and PEMFC's performance," *Electrochim. Acta*, vol. 55, no. 7, pp. 2555–2560, Feb. 2010, doi: 10.1016/j.electacta.2009.12.026.
 - [76] Y. Zhai, H. Zhang, D. Xing, and Z.-G. Shao, "The stability of Pt/C catalyst in H₃PO₄/PBI PEMFC during high temperature life test," *J. Power Sources*, vol. 164, no. 1, pp. 126–133, Jan. 2007, doi: 10.1016/j.jpowsour.2006.09.069.
 - [77] A. Kuzume, E. Herrero, and J. M. Feliu, "Oxygen reduction on stepped platinum surfaces in acidic media," *J. Electroanal. Chem.*, vol. 599, no. 2, pp. 333–343, Jan. 2007, doi: 10.1016/j.jelechem.2006.05.006.
 - [78] P. N. Ross, "Structure Sensitivity in Electrocatalytic Properties of Pt: II . Oxygen Reduction on Low Index Single Crystals and the Role of Steps," *J. Electrochem. Soc.*, vol. 126, no. 1, pp. 78–82, Jan. 1979, doi: 10.1149/1.2128991.
 - [79] N. Markovic, M. Hanson, G. McDougall, and E. Yeager, "The effects of anions on hydrogen electrosorption on platinum single-crystal electrodes," *J. Electroanal. Chem. Interfacial Electrochem.*, vol. 214, no. 1–2, pp. 555–566, Dec. 1986, doi: 10.1016/0022-0728(86)80124-3.

- [80] N. Markovic and P. N. Ross, "The effect of specific adsorption of ions and underpotential deposition of copper on the electro-oxidation of methanol on platinum single-crystal surfaces," *J. Electroanal. Chem.*, vol. 330, no. 1–2, pp. 499–520, Jul. 1992, doi: 10.1016/0022-0728(92)80327-Z.
- [81] W. Chartarrayawadee, S. E. Moulton, D. Li, C. O. Too, and G. G. Wallace, "Novel composite graphene/platinum electro-catalytic electrodes prepared by electrophoretic deposition from colloidal solutions," *Electrochim. Acta*, vol. 60, pp. 213–223, Jan. 2012, doi: 10.1016/j.electacta.2011.11.058.
- [82] B. Seger and P. V. Kamat, "Electrocatalytically Active Graphene-Platinum Nanocomposites. Role of 2-D Carbon Support in PEM Fuel Cells," *J. Phys. Chem. C*, vol. 113, no. 19, pp. 7990–7995, May 2009, doi: 10.1021/jp900360k.
- [83] H. Zhang, W. Zhou, Y. Du, P. Yang, and C. Wang, "One-step electrodeposition of platinum nanoflowers and their high efficient catalytic activity for methanol electro-oxidation," *Electrochem. commun.*, vol. 12, no. 7, pp. 882–885, 2010, doi: 10.1016/j.elecom.2010.04.011.
- [84] T. J. Schmidt, H. A. Gasteiger, G. D. Stäb, P. M. Urban, D. M. Kolb, and R. J. Behm, "Characterization of High-Surface-Area Electrocatalysts Using a Rotating Disk Electrode Configuration," *J. Electrochem. Soc.*, vol. 145, no. 7, pp. 2354–2358, Jul. 1998, doi: 10.1149/1.1838642.
- [85] N. Markovic, H. Gasteiger, and P. N. Ross, "Kinetics of Oxygen Reduction on Pt(hkl) Electrodes: Implications for the Crystallite Size Effect with Supported Pt Electrocatalysts," *J. Electrochem. Soc.*, vol. 144, no. 5, pp. 1591–1597, May 1997, doi: 10.1149/1.1837646.
- [86] M. Nesselberger, S. Ashton, J. C. Meier, I. Katsounaros, K. J. J. Mayrhofer, and M. Arenz, "The Particle Size Effect on the Oxygen Reduction Reaction Activity of Pt Catalysts: Influence of Electrolyte and Relation to Single Crystal Models," *J. Am. Chem. Soc.*, vol. 133, no. 43, pp. 17428–17433, Nov. 2011, doi: 10.1021/ja207016u.
- [87] S. K. Zecevic, J. S. Wainright, M. H. Litt, S. L. Gojkovic, and R. F. Savinell, "Kinetics of O₂ Reduction on a Pt Electrode Covered with a Thin Film of Solid Polymer Electrolyte," *J. Electrochem. Soc.*, vol. 145, no. 9, pp. 3311–3311, Sep. 1998, doi: 10.1149/1.1838802.
- [88] R. Subbaraman, D. Strmcnik, V. Stamenkovic, and N. M. Markovic, "Three Phase Interfaces at Electrified Metal–Solid Electrolyte Systems 1. Study of the Pt(hkl)–Nafion Interface," *J. Phys. Chem. C*, vol. 114, no. 18, pp. 8414–8422, May 2010, doi: 10.1021/jp100814x.
- [89] S. H. Ahn, Y. Liu, and T. P. Moffat, "Ultrathin Platinum Films for Methanol and Formic Acid Oxidation: Activity as a Function of Film Thickness and Coverage," *ACS Catal.*, vol. 5, no. 4, pp. 2124–2136, Apr. 2015, doi:

- 10.1021/cs501228j.
- [90] N. M. Markovića, S. T. Sarraf, H. A. Gasteiger, and P. N. Ross, "Hydrogen electrochemistry on platinum low-index single-crystal surfaces in alkaline solution," *J. Chem. Soc., Faraday Trans.*, vol. 92, no. 20, pp. 3719–3725, 1996, doi: 10.1039/FT9969203719.
 - [91] Y. Bing, H. Liu, L. Zhang, D. Ghosh, and J. Zhang, "Nanostructured Pt-alloy electrocatalysts for PEM fuel cell oxygen reduction reaction," *Chem. Soc. Rev.*, vol. 39, no. 6, p. 2184, 2010, doi: 10.1039/b912552c.
 - [92] T. Biegler, D. A. J. Rand, and R. Woods, "Limiting oxygen coverage on platinized platinum; Relevance to determination of real platinum area by hydrogen adsorption," *J. Electroanal. Chem. Interfacial Electrochem.*, vol. 29, no. 2, pp. 269–277, Feb. 1971, doi: 10.1016/S0022-0728(71)80089-X.
 - [93] Q.-S. Chen, J. Solla-Gullón, S.-G. Sun, and J. M. Feliu, "The potential of zero total charge of Pt nanoparticles and polycrystalline electrodes with different surface structure: The role of anion adsorption in fundamental electrocatalysis," *Electrochim. Acta*, vol. 55, no. 27, pp. 7982–7994, Nov. 2010, doi: 10.1016/j.electacta.2010.03.050.
 - [94] B. E. Conway and H. Angerstein-Kozłowska, "The electrochemical study of multiple-state adsorption in monolayers," *Acc. Chem. Res.*, vol. 14, no. 2, pp. 49–56, Feb. 1981, doi: 10.1021/ar00062a004.
 - [95] G. G. Barna, S. N. Frank, and T. H. Teherani, "A Scan Rate Dependent Determination of Platinum Areas," *J. Electrochem. Soc.*, vol. 129, no. 4, pp. 746–749, Apr. 1982, doi: 10.1149/1.2123963.
 - [96] B. E. Conway and G. Jerkiewicz, "Thermodynamic and electrode kinetic factors in cathodic hydrogen sorption into metals and its relationship to hydrogen adsorption and poisoning," *J. Electroanal. Chem.*, vol. 357, no. 1–2, pp. 47–66, Oct. 1993, doi: 10.1016/0022-0728(93)80373-P.
 - [97] G. Jerkiewicz and A. Zolfaghari, "Comparison of Hydrogen Electroadsorption from the Electrolyte with Hydrogen Adsorption from the Gas Phase," *J. Electrochem. Soc.*, vol. 143, no. 4, pp. 1240–1248, Apr. 1996, doi: 10.1149/1.1836623.
 - [98] A. Essalik, K. Amouzegar, and O. Savadogo, "Quantitative determination of dispersed platinum in carbon by cyclic voltammetry," *J. Appl. Electrochem.*, vol. 25, no. 4, pp. 404–407, Apr. 1995, doi: 10.1007/BF00249660.
 - [99] Y. Garsany, J. Ge, J. St-Pierre, R. Rocheleau, and K. E. Swider-Lyons, "Analytical Procedure for Accurate Comparison of Rotating Disk Electrode Results for the Oxygen Reduction Activity of Pt/C," *J. Electrochem. Soc.*, vol. 161, no. 5, pp. F628–F640, Mar. 2014, doi: 10.1149/2.036405jes.
 - [100] A. Pozio, M. De Francesco, A. Cemmi, F. Cardellini, and L. Giorgi, "Comparison

- of high surface Pt/C catalysts by cyclic voltammetry,” *J. Power Sources*, vol. 105, no. 1, pp. 13–19, Mar. 2002, doi: 10.1016/S0378-7753(01)00921-1.
- [101] W. Zhang, J. Chen, G. F. Swiegers, Z.-F. Ma, and G. G. Wallace, “Microwave-assisted synthesis of Pt/CNT nanocomposite electrocatalysts for PEM fuel cells,” *Nanoscale*, vol. 2, no. 2, pp. 282–286, 2010, doi: 10.1039/B9NR00140A.
- [102] W. Li and A. M. Lane, “Resolving the H_{UPD} and H_{OPD} by DEMS to determine the ECSA of Pt electrodes in PEM fuel cells,” *Electrochem. commun.*, vol. 13, no. 9, pp. 913–916, Sep. 2011, doi: 10.1016/j.elecom.2011.05.028.
- [103] M. Perchthaler *et al.*, “Tungsten materials as durable catalyst supports for fuel cell electrodes,” *J. Power Sources*, vol. 243, pp. 472–480, Dec. 2013, doi: 10.1016/j.jpowsour.2013.06.022.
- [104] E. L. Redmond, B. P. Setzler, F. M. Alamgir, and T. F. Fuller, “Elucidating the oxide growth mechanism on platinum at the cathode in PEM fuel cells,” *Phys. Chem. Chem. Phys.*, vol. 16, no. 11, p. 5301, 2014, doi: 10.1039/c3cp54740j.
- [105] “Linear Sweep and Cyclic Voltammetry: The Principles | Department of Chemical Engineering and Biotechnology,” *14th April*, 2021. <https://www.ceb.cam.ac.uk/research/groups/rg-eme/Edu/linear-sweep-and-cyclic-voltammetry-the-principles>, accessed on 14th April.
- [106] P. R. Unwin, “Introduction to Electroanalytical Techniques and Instrumentation,” in *Encyclopedia of Electrochemistry*, Wiley, 2003.
- [107] K. Kinoshita and P. Stonehart, “Preparation and Characterization of Highly Dispersed Electrocatalytic Materials,” in *Modern Aspects of Electrochemistry*, Boston, MA: Springer US, 1977, pp. 183–266.
- [108] K. Shinozaki, J. W. Zack, R. M. Richards, B. S. Pivovar, and S. S. Kocha, “Oxygen Reduction Reaction Measurements on Platinum Electrocatalysts Utilizing Rotating Disk Electrode Technique. I. Impact of Impurities, Measurement Protocols and Applied Corrections,” *J. Electrochem. Soc.*, vol. 162, no. 10, pp. F1144–F1158, 2015, doi: 10.1149/2.1071509jes.
- [109] D. W. Kumsa, N. Bhadra, E. M. Hudak, S. C. Kelley, D. F. Untereker, and J. T. Mortimer, “Electron transfer processes occurring on platinum neural stimulating electrodes: a tutorial on the $i(V_e)$ profile,” *J. Neural Eng.*, vol. 13, no. 5, p. 052001, Oct. 2016, doi: 10.1088/1741-2560/13/5/052001.
- [110] M. Shao, J. H. Odell, S.-I. Choi, and Y. Xia, “Electrochemical surface area measurements of platinum- and palladium-based nanoparticles,” *Electrochem. commun.*, vol. 31, pp. 46–48, Jun. 2013, doi: 10.1016/j.elecom.2013.03.011.
- [111] S. Moniri, T. Van Cleve, and S. Linic, “Pitfalls and best practices in measurements of the electrochemical surface area of platinum-based nanostructured electro-catalysts,” *J. Catal.*, vol. 345, pp. 1–10, Jan. 2017, doi: 10.1016/j.jcat.2016.11.018.

- [112] D. F. van der Vliet *et al.*, “Unique Electrochemical Adsorption Properties of Pt-Skin Surfaces,” *Angew. Chemie Int. Ed.*, vol. 51, no. 13, pp. 3139–3142, Mar. 2012, doi: 10.1002/anie.201107668.
- [113] M. Shao, Q. Chang, J.-P. Dodelet, and R. Chenitz, “Recent Advances in Electrocatalysts for Oxygen Reduction Reaction,” *Chem. Rev.*, vol. 116, no. 6, pp. 3594–3657, Mar. 2016, doi: 10.1021/acs.chemrev.5b00462.
- [114] G. Jerkiewicz, G. Vatankhah, J. Lessard, M. P. Soriaga, and Y.-S. Park, “Surface-oxide growth at platinum electrodes in aqueous H₂SO₄ Reexamination of its mechanism through combined cyclic-voltammetry, electrochemical quartz-crystal nanobalance, and Auger electron spectroscopy measurements,” *Electrochim. Acta*, vol. 49, no. 9–10, pp. 1451–1459, Apr. 2004, doi: 10.1016/j.electacta.2003.11.008.
- [115] J. Zhang, *PEM Fuel Cell Electrocatalysts and Catalyst Layers*. Springer London, 2008.
- [116] Y. Liu, D. Gokcen, U. Bertocci, and T. P. Moffat, “Self-Terminating Growth of Platinum Films by Electrochemical Deposition,” *Science*, vol. 338, no. 6112, pp. 1327–1330, Dec. 2012, doi: 10.1126/science.1228925.
- [117] E. M. Hudak, J. T. Mortimer, and H. B. Martin, “Platinum for neural stimulation: voltammetry considerations,” *J. Neural Eng.*, vol. 7, no. 2, p. 026005, Apr. 2010, doi: 10.1088/1741-2560/7/2/026005.
- [118] Piero Zanello, *Inorganic Electrochemistry: Theory, Practice and Application*, 1st ed. Royal Society of Chemistry, Cambridge, 2003.

Chapter 4

The durability of Platinum Overlayers formed by Self-Terminating Electrodeposition

4.1 Introduction

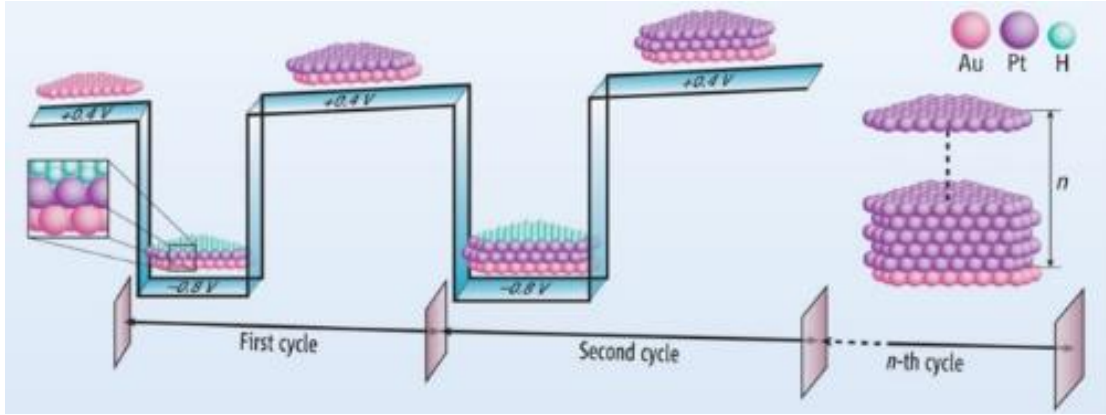
Proton exchange membrane fuel cells (PEMFC) are promising energy-efficient alternatives to combustion engines for automotive applications[1]. Research efforts over the last two decades helped move towards a practical technology that can be mass adopted. Nonetheless, there is still significant scope for innovation to lower costs while meeting the stringent durability targets for FCV applications. The Pt electrocatalyst architecture in the existing FCVs uses Pt alloy nanoparticles coated on carbon black microspheres with $\sim 0.375 \text{ mg}_{\text{Pt}}/\text{cm}^2$ Pt loading[2]. A drawback of this architecture is that the potential transients experienced during vehicle startup and shutdown cycles lead to carbon support corrosion, loss of active surface area, and reduced electrochemical activity. Therefore, carbonless Nanostructured Thin Film (NSTF) electrode designs are presently being explored. One such embodiment utilizes evaporated Pt thin films with sufficient thickness to ensure macroscopic uniformity of coating for electrical connectivity and prevent corrosion of the underlying substrate[3]. However, there is ample scope for developing simpler, cost-effective, additive fabrication processes to further reduce Pt/PGM loading of thin-film nanostructured electrode designs.

An effective way to reduce platinum loading while maintaining its performance is to coat the platinum only as an ultrathin skin, a few atomic layers thick, wherein the platinum utilization is maximized. However, control of platinum formation as atomic layers at room temperature and ambient pressure is difficult. Surface limited redox replacement reaction (SLRR) is one method for obtaining an atomic monolayer under ambient conditions. It comprises two steps: an underpotential deposition (UPD) of Cu [4] or Pb [5] followed by galvanic displacement. The reversible nature of the UPD reactions [6] and the contamination by the residual UPD metals [7] limit the controllability of this step. Electrodeposition is a simple, rapid and one-step fabrication method involving the low cost of the instrumentation and its maintenance for platinum-based electrocatalyst under ambient conditions [8], [9]. A recently reported Self-Terminating Electrodeposition (STED) method [10] has opened up an avenue for wet atomic layer electrodeposition under ambient conditions, which combines basic electrochemistry and surface science.

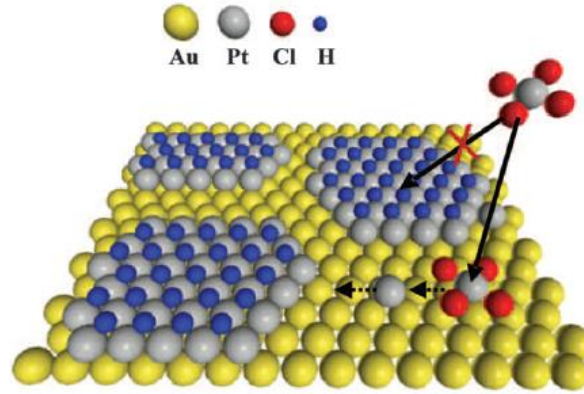
Platinum monolayer electrodeposition is challenging because a direct approach typically gives 3-D Pt growth. [11], [12] However, STED can grow Pt atomic layered film from a liquid electrolyte simply by cycling the potential between two values, equivalent to a wet atomic layer deposition. As shown in Figure 4.1, at the first potential value, the Pt deposition is quenched at potentials just negative of proton reduction via alteration of the double-layer structure induced by a saturated coverage of underpotential deposited hydrogen (H_{upd}). At a second potential value, the surface is reactivated for Pt deposition by stepping the potential to more positive values where the underpotential deposited hydrogen is oxidized and fresh sites for absorption of Pt salt are available. Unlike vapour-based methods like Atomic Layer Deposition (ALD) used in electrocatalyst synthesis, this method requires only a single plating bath. It does

not incur energy-intensive setups or costly infrastructure. Moreover, this method is orders of magnitude faster than the vapour-phase ALD because each layer is produced by cycling the electrode potential rather than exchanging reactants. The applied electrode potential is the only parameter that controls the reaction rate. Despite overpotential being more than 1 volt, Pt deposition gets quenched due to blocking of the additional deposition of Pt by H_{upd} . This also leads to less carryover of contaminants compared to the processes where reactants are exchanged.

Several studies report the application of platinum atomic overlayers formed using STED for hydrogen evolution reaction (HER)[6], [13]–[17], hydrogen oxidation reaction(HOR)[18], oxygen reduction reaction(ORR)[19], methanol/formic acid oxidation(FAO)[7], [20], [21], high temperature in-situ phosphoric acid fuel cell testing[22], pH sensing[23] etc. However, there haven't been any studies to evaluate the durability of these platinum overlayers for FCV application, which is the focus of this part of our research.



(a)



(b)

Figure 4.1: (a) Potential cycling for STED method on evaporated Au substrate (b) schematic for Pt deposition getting blocked by H_{upd} [10]

4.2 Experimental

4.2.1 Synthesis of platinum atomic overlayers on gold (Au):

Platinum atomic overlayers were electrodeposited using the STED method in a standard three-electrode setup. For ease of understanding and comparison, all

the potentials in this article are converted to potential against the Reversible Hydrogen Electrode (RHE)[24]. All the currents are reported as density (currents per unit geometric area in A cm^{-2}). The working electrode was a strip of e-beam evaporated gold with an exposed area of 90 mm^2 . Gold (nominally 150 nm thick) films were deposited on a silicon wafer with an underlying adhesive layer of titanium (nominally 20 nm) using an e-beam evaporation facility on 4" single-side polished silicon wafers at the National nanofabrication centre (NNFC), CeNSE, IISc Bangalore (India). These were then diced into samples of the desired size. $\text{Ag}_{(\text{s})}/\text{AgCl}_{(\text{aq})}/\text{KCL}(1\text{M})$ was used as a reference electrode, while a platinum foil having a surface area of 4 cm^2 was used as a counter electrode. The cleaning and pre-treatment of electrodes, glassware and electrochemical cell are per previously described protocols [25].

The electrolyte used for platinum electrodeposition contained 3 mM K_2PtCl_4 and 0.5 M KCl (supporting electrolyte). The pH of the electrolyte was adjusted to 4 with the help of HClO_4 and NaOH. Briefly, platinum overlayers were synthesized by the periodic pulsing of potential between -0.33 V and 0.87 V for 30 s each. At -0.33 V, an atomically thin platinum layer is deposited from adsorbed PtCl_4^{2-} reduction. Further, a layer of the underpotential deposited hydrogen (H_{upd})[26] is formed on the platinum surface, altering the double-layer structure, which blocks further platinum deposition by inhibiting adsorption of PtCl_4^{2-} [27]. The surface is reactivated for further platinum deposition by stepping the potential to 0.87 V, where the H_{upd} is oxidized. This cycle can be repeated to deposit the desired number of platinum overlayers providing control over platinum thickness and loading. Nitrogen (N_2) was purged for ~ 30 minutes before electrodeposition to remove dissolved O_2 from the electrolyte. N_2 was jacketed during the electrodeposition to avoid evaporation-induced platinum deposition at the interface of electrolyte and air [25]. The working electrode was

removed from the electrochemical cell, rapidly rinsed with DI water, and dried in an N₂ stream after electrodeposition.

Before Pt deposition, the gold substrate was electrochemically cleaned by cycling it between 0 to 1.7 V at 100 mV/s for 20 cycles in 0.1M HClO₄. The electrochemical response of the evaporated Au film is shown in Figure 4.2, which is consistent with the reported in the literature[28], [29]. In the anodic scan, the double layer of Au is present till 1.25V, beyond which AuO forms. In the reverse scan, AuO is reduced ~ 1.15 V as a single sharp peak. The charge corresponding to the gold oxide reduction peak had $< 5\%$ relative variation (303.9 ± 15.1 $\mu\text{C}/\text{cm}^2$) during CVs across three different samples, confirming the repeatability of the evaporated Au samples.

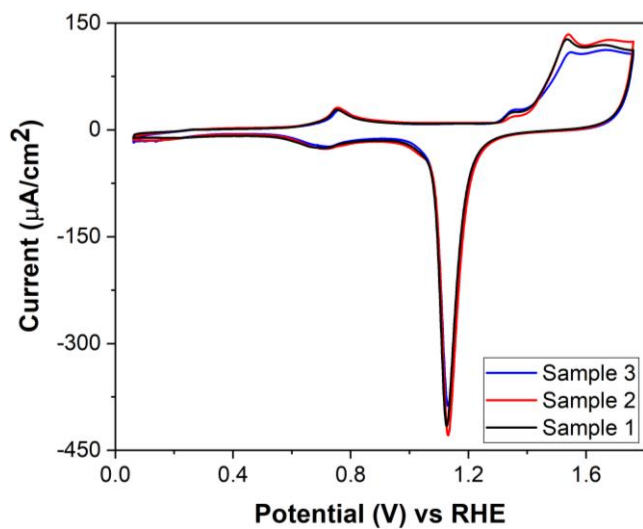


Figure 4.2: CVs of evaporated Au substrate in 0.1 M HClO₄ and 100 mV s⁻¹ to confirm the repeatability

The Pt deposition profile was analyzed by linear sweep voltammetry from 0.956 V to -0.454 V at 2 mV/s (Figure 4.3). Appreciable currents for Pt reduction onto Au surface start to appear below 0.5 V. As the potential scan is continued, there is a substantial increase in the current, to a maximum around 0.1 V, which is related to diffusion-limited PtCl_4^{2-} reduction[10]. Further, the current diminishes because of increased mass transfer layer thickness. This sharp drop culminates in a minimum near -0.25 V, indicating quenching of bulk Pt deposition. The current rise beyond -0.25 V is attributed to the hydrogen evolution reaction (HER). The deposition profile at different potentials was analyzed by potentiostatic experiments for 500 s each at -0.328 V, 0.072 V and 0.872 V, which correspond to faintly visible Pt thin film (corresponding to atomically thin layered Pt), a bulk deposit of Pt film, and no Pt film respectively (see insets of Figure 4.3). Despite having an overpotential of more than 1V, where bulk deposition would have been expected ordinarily, a very thin film corresponding to a Pt monolayer could be synthesized at -0.328 V because of the remarkable alteration of double-layer arising out of H adsorption, as described earlier[10].

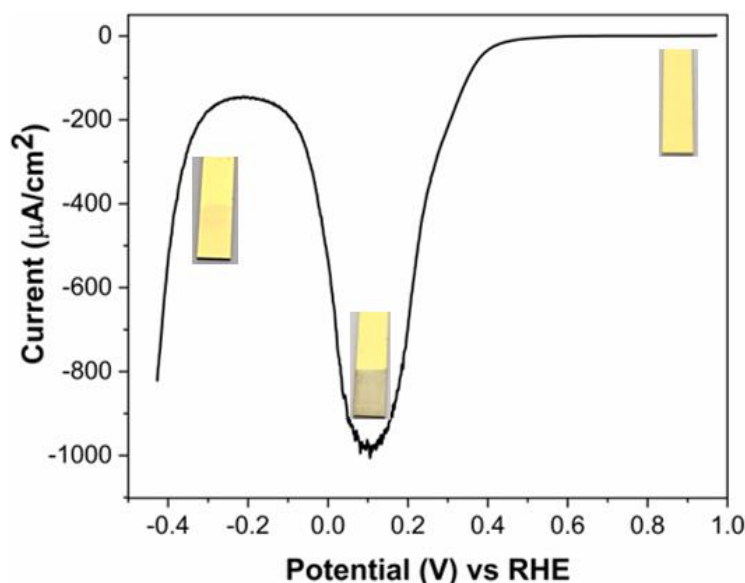


Figure 4.3: LSV profile for Pt deposition on Au substrate from 3.0 mM K_2PtCl_4 solution maintained at pH 4. The insets are digital images of potentiostatic deposition of Pt on Au for 500 s at -0.328 V, 0.072 V and 0.872 V respectively

4.2.2 Platinum overlayer formation using STED

As shown in Figure 4.3(a), the potential scheme was applied to synthesize Pt overlayers on Au. The current corresponding to Pt reduction attenuates to ~ 0 A within a few seconds, denoting how fast deposition quenching happens. The current spikes for electrodeposition with and without K_2PtCl_4 were compared to confirm the Pt deposition. As shown in Figure 4.4(b), the current profile in the case of K_2PtCl_4 is higher with more time to attenuate to 0 A due to the Pt reduction process. The I-t response for the chronoamperometric deposition for 20 cycles of Pt deposition is shown in Figure 4.4(c), where the negative current spikes correspond to Pt deposition. In contrast, positive spikes correspond to H_{upd} desorption (IUPAC convention). The increase in the current maximum with the number of cycles indicates increasing surface coverage with the number

of Pt cycles. It suggests that the deposition is not strictly happening in a layer-by-layer fashion. The area under the I-t curve corresponds to the total charge required for Pt deposition. Using Faraday's law of electrolysis, the mass of Pt was found to be $39.99 \pm 0.84 \mu\text{g}/\text{cm}^2$; which is in close agreement with the value of $41.94 \pm 8.18 \mu\text{g}/\text{cm}^2$ measured using ICP-OES.

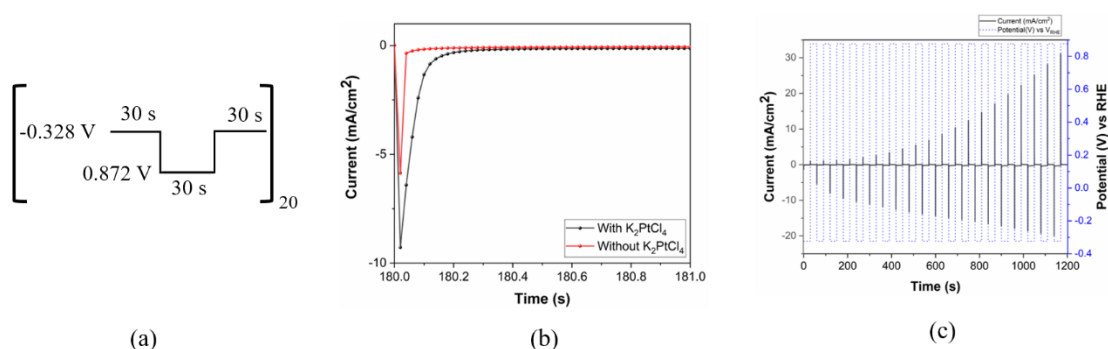


Figure 4.4: (a) Potential scheme applied for STED, (b) Difference in the CA profiles with and without K₂PtCl₄ in the electrolyte, (c) CA profiles for 20 cycles of Pt deposition. The applied potential profile is also shown as dotted lines.

4.2.3 Ex-situ durability analysis of Pt overlayers on Au:

The ex-situ durability analysis provides a quick initial screening for the durability of the newly synthesized electrocatalysts of FCVs[30]. In ex-situ durability analysis, potential transients corresponding to the varying power demand of a fuel cell vehicle are enforced onto the electrocatalyst[31], and corresponding activity loss after the stipulated number of potential cycles is measured. The samples comprising platinum atomic overlayers were subjected to the ex-situ durability analysis in 0.1 M HClO₄. The applied potential transient was at 700 mV/s between 0.66 V and 1.01 V (referred to as load cycling from hereon), and the activity loss was measured by the ECSA using a

CV from 0.06 V to 1.26 V @ 50 mV/s (referred to as ECSA cycles from hereon). The under-potential deposition of hydrogen (H_{upd}) method was used to calculate the ECSA. In this method, the number of reactive sites on an electrocatalyst can be found by integrating the total charge corresponding to hydrogen desorption from the surface of the platinum electrocatalyst [32]. ECSA was measured by integrating the anodic side of the CV curve (corresponding to the H_{upd} desorption) from 0.06 to 0.45 V. The deposited platinum overlayers' roughness (corresponding to the monolayer equivalence) was calculated by normalizing with 210 $\mu\text{C}/\text{cm}^2$, the charge corresponding to a ML of H_{upd} desorption on polycrystalline platinum [50]. The ECSA was calculated by normalising Q_H with the platinum loading and the normalising factor of 210 $\mu\text{C}/\text{cm}^2_{\text{Pt}}$.

The ECSA loss during the ex-situ analysis after the stipulated number of cycles (initially, 10, 100, 1000, 3000, 10000, 20000 and 30000 as per the US DOE protocols) consisting of potential transients (which simulate the effects of vehicle acceleration and deceleration[31]) was measured. N_2 was purged like that during platinum electrodeposition to avoid O_2 diffusion in an electrochemical cell and oxygen reduction reaction, leading to erroneous measurement [25]. Before starting the ex-situ durability analysis, the samples were electrochemically activated by scanning between 0 to 1.35V at 100 mV/s for 20 cycles to obtain a stable and reorganized surface. The ECSA was measured by integrating the H_{upd} desorption area in the 5th ECSA cycle.

The corresponding CVs after the desired numbers of load cycles are shown in Figure 4.5(a). The initial H_{upd} charge was $395.3 \pm 23.9 \mu\text{C}/\text{cm}^2$ (corresponding to ECSA of $4.71 \pm 0.34 \text{ m}^2/\text{g}_{\text{Pt}}$). The < 7% variation in measured H_{upd} activity attests to the excellent repeatability of the deposition protocol followed. The

variation of electrochemical activity (averaged over three different samples) with the number of load cycles is shown in Figure 4.5(b). The charge under the H_{upd} desorption region corresponds to ECSA retention of $62.9 \pm 4.9\%$ after 30,000 durability cycles which meets the DOE criterion of $< 40\%$ loss in ECSA for FCV applications. The ECSA loss is attributed to the particle growth arising from coalescence and dissolution/ redeposition[65], [66]. The particle growth is also confirmed by the increased onset of PtO formation and positive shift in the PtO reduction peak[67], [68] during the anodic scan of platinum CVs, as shown in Figure 4.5(a). The complete coverage of Au substrate by the Pt layer was confirmed by the absence of a cathodic peak around 1.1 V, corresponding to the reduction of gold oxide. The characteristic peaks around 0.12 V and 0.22 V in the H_{des} region correspond to the desorption of H atoms from polycrystalline Pt samples[33].

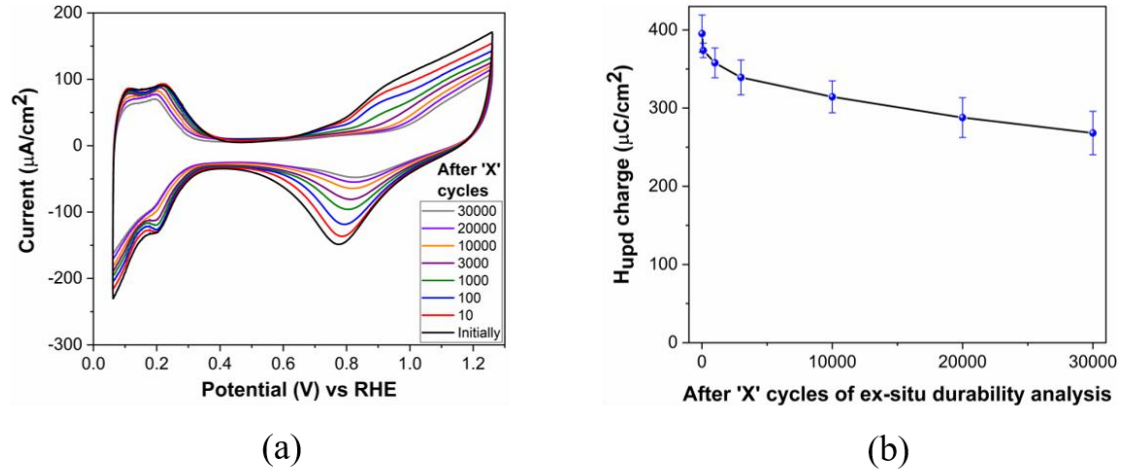


Figure 4.5: (a) Representative CV curves in 0.1M HClO₄ obtained intermittently during ex-situ durability test for 30,000 cycles (b) H_{upd} variation with number of load cycles during ex-situ durability analysis

However, the ECSA for platinum thin films is substantially lower ($4.71 \pm 0.34 \text{ m}^2 \text{ g}_{\text{Pt}}^{-1}$) than that of the commercial Pt/C catalyst ($65 \pm 2 \text{ m}^2 \text{ g}_{\text{Pt}}^{-1}$) [58] because of having an RMS surface roughness of 1.32 nm for evaporated gold (Figure 4.6), which is practically a flat surface, leading to low surface area enhancement compared to the nanostructured substrate. Gold incorporation is also reported to enhance the durability of platinum by stabilization effect[59]–[61] by raising the oxidation potential, which suppresses the platinum dissolution[62]. Several groups have reported enhancement in the activity upon gold addition in platinum electrocatalyst, which is attributed to the reduction in the bond strength of adsorbed oxygen intermediates[63] and allowing better electronic coupling between platinum and gold[64].

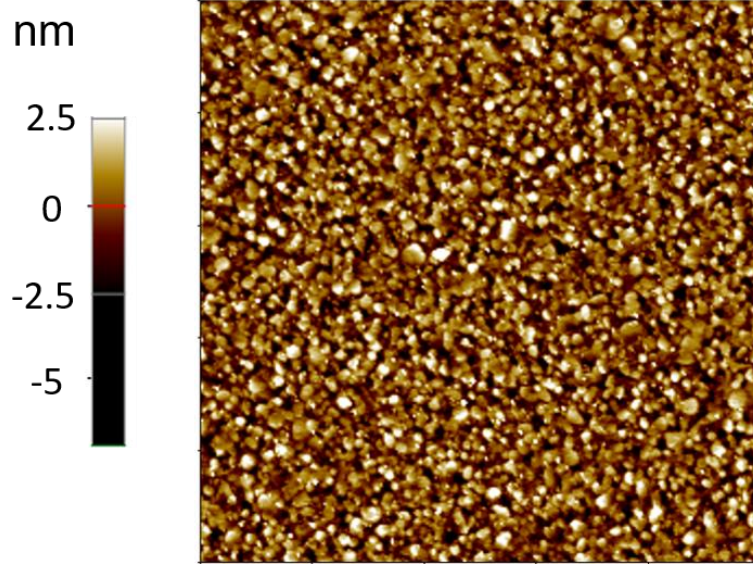


Figure 4.6: AFM of e-beam evaporated Au surface

EDS characterization of the as-synthesized samples confirms the presence of Pt. Table 4.1 presents the elemental analysis from five different randomly chosen spots. The average volumetric ratio of Au/Pt is determined to be 31.47 ± 4.76 (atomic ratio normalized with atomic density). Since the Au layer nominal thickness is 150 nm, the average Pt overlayer thickness is estimated to be 4.86 ± 0.78 nm. This value corresponds well with the thickness expected (~ 4.6 nm) for 20 atomic layers with Pt(111) d-spacing.

Table 4.1: Elemental analysis (atom %) based on EDS spectra from five different spots

Elements	Spot 1	Spot 2	Spot 3	Spot 4	Spot 5	Average
Si K	38.92	38.74	38.89	39.43	39.81	39.16 ± 0.45
Ti K	1.40	1.75	1.48	2.17	1.31	1.62 ± 0.35
Pt M	1.76	1.92	2.27	2.44	1.79	2.04 ± 0.30
Au M	57.93	57.59	57.35	55.95	57.09	57.18 ± 0.76
The volumetric ratio of Au/Pt (atomic ratio scaled with atomic density)	36.21	33.01	27.80	25.23	35.10	31.47 ± 4.76

The morphological evolution of platinum overlayers is shown in Figure 4.7. E-beam evaporated gold has boulder morphology (see Figure 4.7(a)). After platinum deposition, the underlying surface morphology partially mimics the structure of gold but is covered with platinum clusters fusing into each other (see Figure 4.7(b)). After ex-situ durability analysis, the platinum dissolution can be seen from the ruptured surface film with holes, as seen in Figure 4.7(c). The uniformity of platinum deposition was checked with the EDS elemental mapping analysis for 20 cycles of platinum (before durability analysis, Figure 4.8), which reflected uniform platinum distribution.

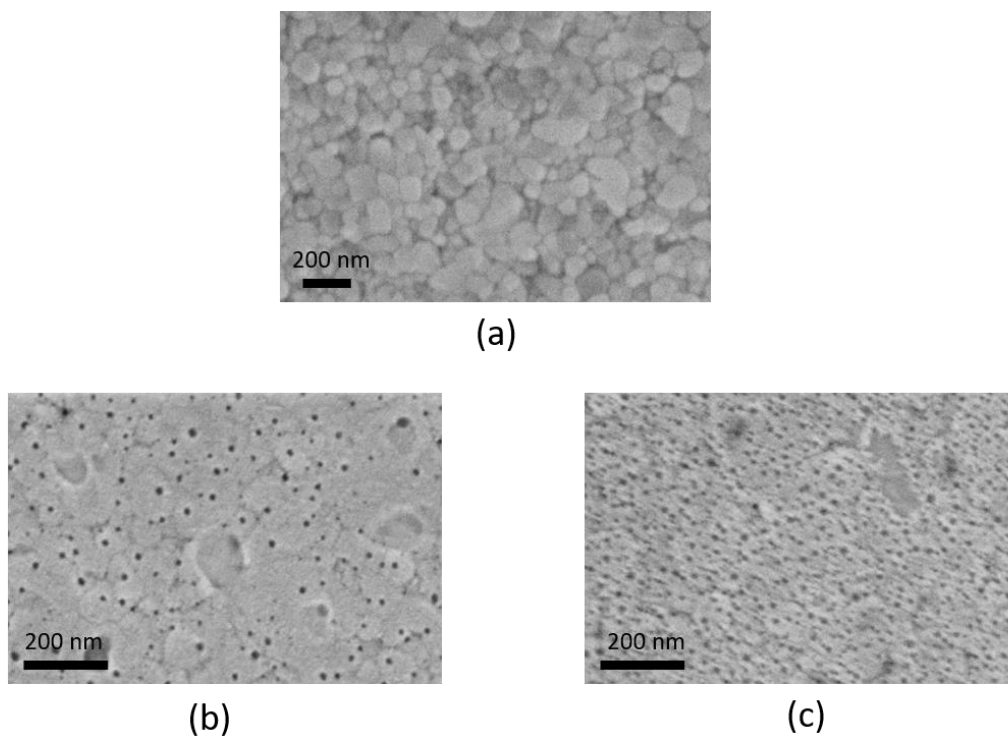


Figure 4.7: Surface morphology of (a) e-beam evaporated gold substrate (b) 20 cycles of platinum deposited on gold (before durability) (c) 20 cycles of platinum deposited on gold (after durability)

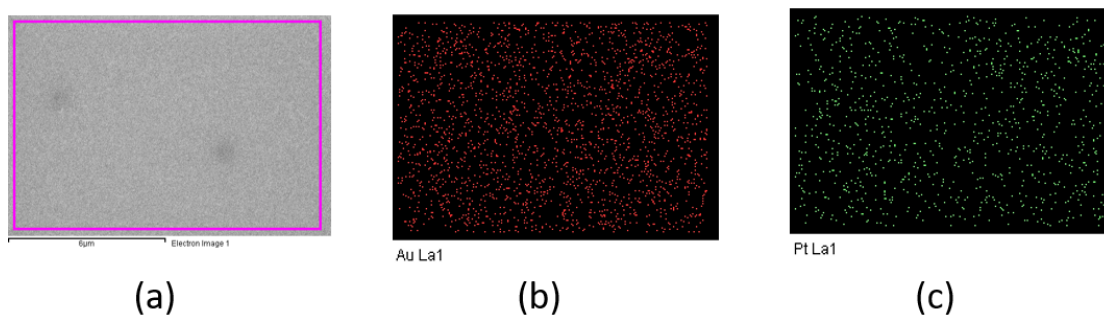


Figure 4.8: Elemental mapping of a sample with 20 cycles of Pt deposited on Au (before durability analysis) (b) Au distribution (c) Pt distribution

XPS characterization confirms the presence of Pt on the surface, as the Pt signal is much higher in magnitude than the Au signal (Figure 4.9). Such Pt surface enrichment is expected for overlayer deposition. The presence of Pt 4f_{7/2} peak and Pt 4f_{5/2} peaks at 70.84 eV and 74.19 eV, respectively, confirm that Pt is present mainly in the Pt(0) state. The thickness of the Pt overlayers was approximated from the XPS signal using a simple homogeneous overlayer model derived from the Beer-Lambert law applied to the straight-line attenuation as described earlier ([34],[35]). The computed value of the thickness is 5.08 ± 0.25 nm (from three different samples), which lies within 5% of the value estimated by EDS (five different spots within a sample).

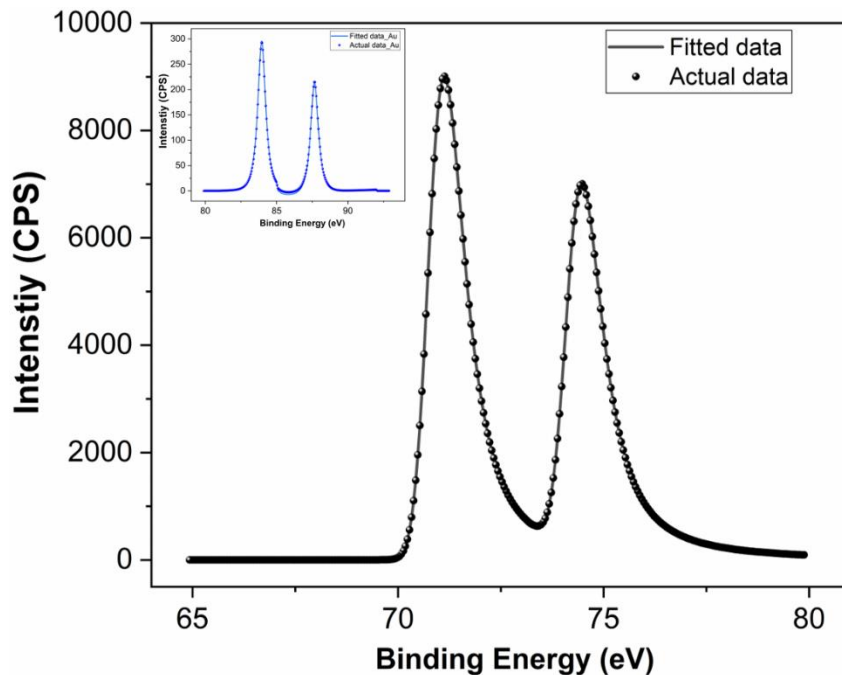


Figure 4.9: XPS spectra of Pt4f region for samples synthesized using 20 cycles of STED. The inset shows signal from Au4f region

Summary

Twenty atomic layers of Pt were electrodeposited using the STED technique on an e-beam evaporated Au substrate. The chronoamperometric currents corresponding to Pt reduction show an increase with the number of cycles, indicating increasing coverage. The measured Pt loading using ICP OES ($41.94 \pm 8.18 \text{ } \mu\text{g}/\text{cm}^2$) matches closely with that calculated from the area under the Pt reduction peaks in the chronoamperometry curve ($39.99 \pm 0.84 \text{ } \mu\text{g}/\text{cm}^2$). The estimated thickness of the Pt overlayer using EDS ($4.86 \pm 0.78 \text{ nm}$) and XPS ($5.08 \pm 0.25 \text{ nm}$) closely matches the expected thickness equivalent to 20 atomic layers of Pt with Pt(111) d spacing. These results *in toto* suggest that the initial cycles have less than complete monolayer coverage, and the deposition in subsequent cycles fills these voids. A systematic study to unravel this issue is currently underway. The samples show excellent repeatability in terms of electrochemical performance for H_{upd} activity. The samples retain $62.9 \pm 4.9\%$ of their initial ECSA after 30,000 ex-situ durability cycles, fulfilling the US DOE criterion for $<40\%$ loss in ECSA.

References:

- [1] M. K. Debe, "Electrocatalyst approaches and challenges for automotive fuel cells," *Nature*, vol. 486, no. 7401, pp. 43–51, Jun. 2012, doi: 10.1038/nature11115.
- [2] A. L.-L. Henning Lohse-Busch, M. Duoba, K. Stutenberg, S. Iliev, M. Kern, B. Richards, and M. Christenson, "Toyota Mirai, Report ANL/ESD-18/12. Technology Assessment of a Fuel Cell Vehicle: 2017, 10. IL -, " 2018.
- [3] M. K. Debe, "Novel catalysts, catalysts support and catalysts coated membrane methods," in *Handbook of Fuel Cells*, Chichester, UK: John Wiley & Sons, Ltd, 2010, pp. 1–14.
- [4] J. Rossmeisl *et al.*, "Bifunctional anode catalysts for direct methanol fuel cells," *Energy Environ. Sci.*, vol. 5, no. 8, pp. 8335–8342, 2012, doi: 10.1039/c2ee21455e.
- [5] S.-M. Hwang, J. E. Bonevich, J. J. Kim, and T. P. Moffat, "Electrodeposition of Pt₁₀₀–xPb_x Metastable Alloys and Intermetallics," *Journal of The Electrochemical Society*, vol. 158, no. 6. p. D307, 2011, doi: 10.1149/1.3572049.
- [6] Y. Liu, C. M. Hangarter, D. Garcia, and T. P. Moffat, "Self-terminating electrodeposition of ultrathin Pt films on Ni: An active, low-cost electrode for H₂ production," *Surf. Sci.*, vol. 631, pp. 141–154, Jan. 2015, doi: 10.1016/j.susc.2014.06.002.
- [7] J. Byun, S. H. Ahn, and J. J. Kim, "Self-terminated electrodeposition of platinum on titanium nitride for methanol oxidation reaction in acidic electrolyte," *Int. J. Hydrogen Energy*, vol. 45, no. 16, pp. 9603–9611, Mar. 2020, doi: 10.1016/j.ijhydene.2020.01.204.
- [8] H. Park *et al.*, "Direct fabrication of gas diffusion cathode by pulse electrodeposition for proton exchange membrane water electrolysis," *Appl. Surf. Sci.*, vol. 444, pp. 303–311, 2018, doi: 10.1016/j.apsusc.2018.03.071.
- [9] N. Dimitrov, I. Achari, and S. Ambrozik, "Palladium ultrathin film growth by surface-limited redox replacement of Cu and H UPD monolayers: Approaches, pros, cons, and comparison," *Electrochem. Soc. Interface*, vol. 27, no. 2, pp. 65–69, 2018, doi: 10.1149/2.f06182if.

- [10] Y. Liu, D. Gokcen, U. Bertocci, and T. P. Moffat, "Self-Terminating Growth of Platinum Films by Electrochemical Deposition," *Science*, vol. 338, no. 6112, pp. 1327–1330, Dec. 2012, doi: 10.1126/science.1228925.
- [11] M. Liu, Z. Lyu, Y. Zhang, R. Chen, M. Xie, and Y. Xia, "Twin-Directed Deposition of Pt on Pd Icosahedral Nanocrystals for Catalysts with Enhanced Activity and Durability toward Oxygen Reduction," *Nano Lett.*, vol. 21, no. 5, pp. 2248–2254, Mar. 2021, doi: 10.1021/acs.nanolett.1c00007.
- [12] S. Brimaud and R. J. Behm, "Electrodeposition of a Pt Monolayer Film: Using Kinetic Limitations for Atomic Layer Epitaxy," *J. Am. Chem. Soc.*, vol. 135, no. 32, pp. 11716–11719, Aug. 2013, doi: 10.1021/ja4051795.
- [13] M. Li, Q. Ma, W. Zi, X. Liu, X. Zhu, and S. Liu, "Pt monolayer coating on complex network substrate with high catalytic activity for the hydrogen evolution reaction," *Sci. Adv.*, vol. 1, no. 8, pp. e1400268–e1400268, 2015, doi: 10.1126/sciadv.1400268.
- [14] L. Pang *et al.*, "Controlled Pt Monolayer Fabrication on Complex Carbon Fiber Structures for Superior Catalytic Applications," *Electrochim. Acta*, vol. 222, pp. 1522–1527, 2016, doi: 10.1016/j.electacta.2016.11.134.
- [15] L. Pang, Y. Zhang, and S. (Frank) Liu, "Monolayer-by-monolayer growth of platinum films on complex carbon fiber paper structure," *Appl. Surf. Sci.*, vol. 407, pp. 386–390, 2017, doi: 10.1016/j.apsusc.2017.02.144.
- [16] H. Kim, J. Kim, G. H. Han, H. W. Jang, S. Y. Kim, and S. H. Ahn, "Hydrogen evolving electrode with low Pt loading fabricated by repeated pulse electrodeposition," *Korean J. Chem. Eng.*, vol. 37, no. 8, pp. 1340–1345, 2020, doi: 10.1007/s11814-020-0617-z.
- [17] H. Kim, S. Choe, H. Park, J. H. Jang, S. H. Ahn, and S. K. Kim, "An extremely low Pt loading cathode for a highly efficient proton exchange membrane water electrolyzer," *Nanoscale*, vol. 9, no. 48, pp. 19045–19049, 2017, doi: 10.1039/c7nr07224d.
- [18] Y. Liu, H. You, Y. C. Kimmel, D. V Esposito, J. G. Chen, and T. P. Moffat, "Self-terminating electrodeposition of Pt on WC electrocatalysts," *Appl. Surf. Sci.*, vol. 504, no. June 2019, p. 144472, Feb. 2020, doi: 10.1016/j.apsusc.2019.144472.

- [19] Y.-J. Deng, V. Tripkovic, J. Rossmeisl, and M. Arenz, "Oxygen Reduction Reaction on Pt Overlayers Deposited onto a Gold Film: Ligand, Strain, and Ensemble Effect," *ACS Catal.*, vol. 6, no. 2, pp. 671–676, Feb. 2016, doi: 10.1021/acscatal.5b02409.
- [20] S. H. Ahn, Y. Liu, and T. P. Moffat, "Ultrathin Platinum Films for Methanol and Formic Acid Oxidation: Activity as a Function of Film Thickness and Coverage," *ACS Catal.*, vol. 5, no. 4, pp. 2124–2136, Apr. 2015, doi: 10.1021/cs501228j.
- [21] A. S. Lapp and R. M. Crooks, "Multilayer electrodeposition of Pt onto 1–2 nm Au nanoparticles using a hydride-termination approach," *Nanoscale*, vol. 12, no. 20, pp. 11026–11039, 2020, doi: 10.1039/D0NR02929G.
- [22] D. K. Kim *et al.*, "Performance enhancement of high-temperature polymer electrolyte membrane fuel cells using Pt pulse electrodeposition," *J. Power Sources*, vol. 438, no. November 2018, p. 227022, 2019, doi: 10.1016/j.jpowsour.2019.227022.
- [23] E. Lee, M. Sung, Y. Wang, and J. Kim, "Atomic Layer Electrodeposition of Pt on Nanoporous Au and its Application in pH Sensing," *Electroanalysis*, vol. 30, no. 9, pp. 2028–2034, 2018, doi: 10.1002/elan.201800252.
- [24] G. Jerkiewicz, "Standard and Reversible Hydrogen Electrodes: Theory, Design, Operation, and Applications," *ACS Catal.*, vol. 10, no. 15, pp. 8409–8417, Aug. 2020, doi: 10.1021/acscatal.0c02046.
- [25] K. Agrawal, A. A. Naik, S. Chaudhary, D. Parvatalu, and V. Santhanam, "Prudent Practices in ex situ Durability Analysis Using Cyclic Voltammetry for Platinum-based Electrocatalysts," *Chem. – An Asian J.*, vol. 16, no. 21, pp. 3311–3325, Nov. 2021, doi: 10.1002/asia.202100746.
- [26] S. Proch, S. Yoshino, K. Kitazumi, J. Seki, K. Kodama, and Y. Morimoto, "Over-Potential Deposited Hydrogen (Hopd) as Terminating Agent for Platinum and Gold Electro(co)Deposition," *Electrocatalysis*, vol. 10, no. 6, pp. 591–603, Nov. 2019, doi: 10.1007/s12678-019-00551-4.
- [27] Y. Liu, C. M. Hangarter, D. Garcia, and T. P. Moffat, "Self-terminating electrodeposition of ultrathin Pt films on Ni: An active, low-cost electrode for H₂ production," *Surf. Sci.*, vol. 631, pp. 141–154, 2015, doi: 10.1016/j.susc.2014.06.002.

- [28] J. Kim, J. Lee, S. Kim, Y.-R. Kim, and C. K. Rhee, “Contrasting Electrochemical Behavior of CO, Hydrogen, and Ethanol on Single-Layered and Multiple-Layered Pt Islands on Au Surfaces,” *J. Phys. Chem. C*, vol. 118, no. 42, pp. 24425–24436, Oct. 2014, doi: 10.1021/jp5062557.
- [29] J. Snyder *et al.*, “Thin film approach to single crystalline electrochemistry,” *J. Phys. Chem. C*, vol. 117, no. 45, pp. 23790–23796, 2013, doi: 10.1021/jp4078272.
- [30] I. Takahashi and S. S. Kocha, “Examination of the activity and durability of PEMFC catalysts in liquid electrolytes,” *J. Power Sources*, vol. 195, no. 19, pp. 6312–6322, Oct. 2010, doi: 10.1016/j.jpowsour.2010.04.052.
- [31] V. Parrondo, J., Han, T., Niangar, E., Wang, C., Dale, N., Adjemian, K., and Ramani, “Platinum supported on titanium-ruthenium oxide is a remarkably stable electrocatalyst for hydrogen fuel cell vehicles,” *Proc. Natl. Acad. Sci.*, vol. 111, no. 1, pp. 45–50, Jan. 2014, doi: 10.1073/pnas.1319663111.
- [32] J. Lobato, H. Zamora, J. Plaza, and M. A. Rodrigo, “Composite Titanium Silicon Carbide as a Promising Catalyst Support for High-Temperature Proton-Exchange Membrane Fuel Cell Electrodes,” *ChemCatChem*, vol. 8, no. 4, pp. 848–854, 2016, doi: 10.1002/cctc.201501152.
- [33] García-Cruz, M. Leticia, and V. and Solla-Gullón, “Shape-controlled metal nanoparticles for electrocatalytic applications,” *Phys. Sci. Rev.*, vol. 4(1), pp. 1–34, 2018, doi: 10.1515/psr-2017-0124.
- [34] Y. Liu, C. M. Hangarter, D. Garcia, and T. P. Moffat, “Self-terminating electrodeposition of ultrathin Pt films on Ni: An active, low-cost electrode for H₂ production,” *Surf. Sci.*, vol. 631, pp. 141–154, Jan. 2015, doi: 10.1016/j.susc.2014.06.002.
- [35] S. H. Ahn, Y. Liu, and T. P. Moffat, “Ultrathin Platinum Films for Methanol and Formic Acid Oxidation: Activity as a Function of Film Thickness and Coverage,” *ACS Catal.*, vol. 5, no. 4, pp. 2124–2136, Apr. 2015, doi: 10.1021/cs501228j.

Chapter 5

Platinum atomic overlayer deposition on silver, gold and silver-gold alloy thin film

5.1 Introduction

Pt-coated Ag nanowires are of particular interest in electrocatalysis due to the following reason: First, silver is one of the best electric conductors[1]. Second, using silver helps in the electronic coupling and selective dissolution of an acidic medium[2]. Our goal was to combine the platinum overlayer deposition through STED with the inkjet-printed silver nanostructures to leverage their high conductivity, high surface area and ease of synthesis. To carry forward the learnings of platinum deposition on evaporated gold and avoid the complications associated with the nanostructure instability, we have initially studied platinum deposition on a relatively flat substrate, which is evaporated silver.

5.2 Experimental

5.2.1 Platinum deposition on e-beam evaporated silver

The silver (100 nm) was evaporated in a thermal evaporator (VR Technologies), with a 10 nm adhesive layer of chromium. To confirm the stability of evaporated silver thin film, it was dipped in the platinum solution. The evaporated silver thin film delaminated within a few seconds. To circumvent this issue, we took commercially available gold and silver thin films (nominal thickness of 20 nm,

purchased from H.M.Warakhwala, Ahmedabad, India) and did the platinum deposition studies. The working electrode was prepared by picking the thin film onto the double-sided tape stuck on a strip of PET sheet.

5.2.2 Platinum deposition on commercial gold and silver thin film

As a transition in moving towards thin films, we did preliminary experiments to understand the effect of film thinness by comparing the performance loss for 12 and 20 cycles of platinum on evaporated gold (nominal thickness ~ 150 nm) and commercially purchased gold thin films (thickness ~ 20 nm). As discussed in the previous chapter, the required number of platinum overlayers were deposited by cycling the potential for STED.

The samples were subjected to ex-situ durability analysis to test their activity retention. The ECSA retention (for triangular wave potential load cycling, as described in the previous chapter) found for Pt on evaporated gold was 62.9 ± 4.9 % and 68.2 ± 2.1 % for 20 and 12 cycles of Pt, while that of the commercial gold thin film was 72.5 % and 80.7 %, respectively when performed for one sample of each (as shown in Figure 5.1(a) and Figure 5.1(b) respectively). These initial results confirm that platinum on thin films can give durable platinum overlayers with similar loadings to the evaporated thin film.

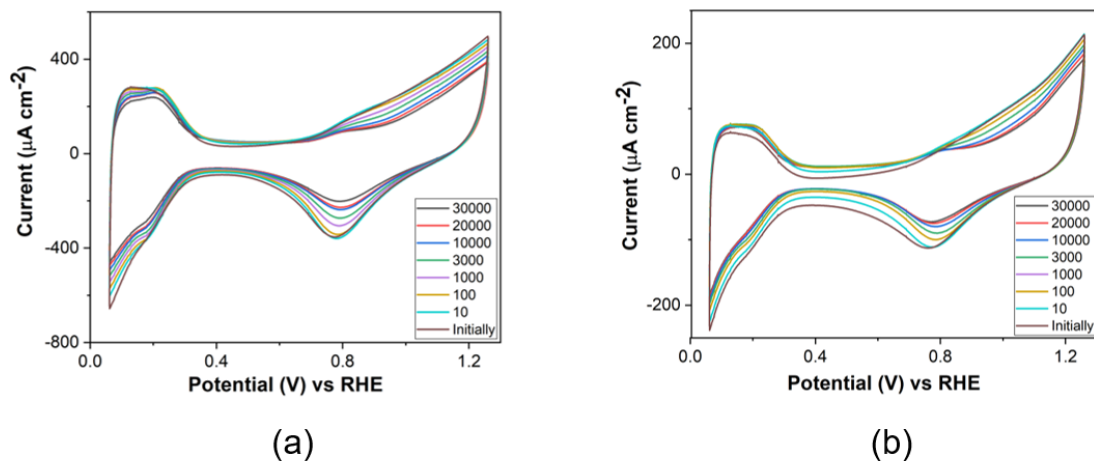


Figure 5.1: Ex-situ durability analysis for (a) 12 cycles (b) 20 cycles of platinum on gold thin films. The CVs were conducted in 0.1M HClO₄ at 50 mV s⁻¹

The amount of platinum deposited on gold thin films from the area under the chronoamperometry curves was $14.87 \pm 2.83 \mu\text{g cm}^{-2}$, while that measured using ICP-OES was $5.2 \pm 4.0 \mu\text{g cm}^{-2}$. The measured platinum loading on e-beam evaporated gold was $5.65 \pm 1.49 \mu\text{g cm}^{-2}$, confirming a similar level of platinum loadings on a commercial gold film. The platinum overlays on gold thin film corresponding to eight STED cycles couldn't be detected in EDS after platinum deposition or durability analysis.

The oxidation state of platinum was checked with the help of XPS, which confirmed the oxidation state of platinum remains in the metallic state from deposition to post durability analysis, as shown in Figure 5.2(a) to Figure 5.2(c).

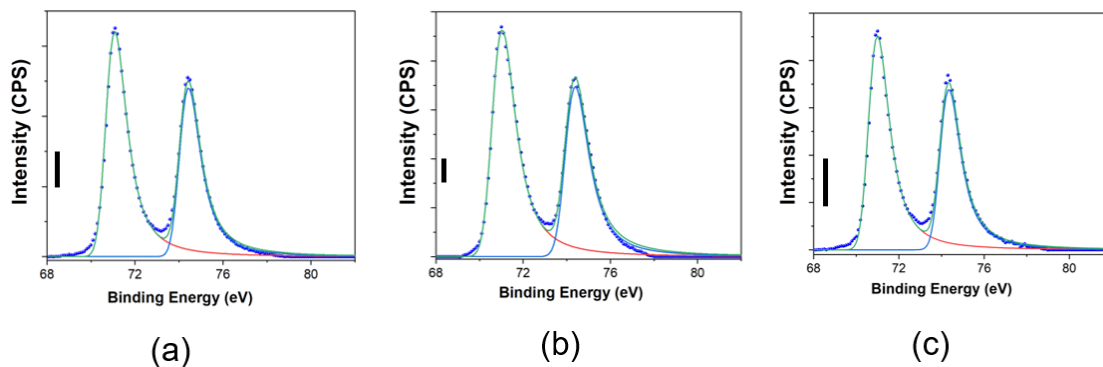


Figure 5.2: XPS spectra for of Pt4f regions (a) After 8 cycles of platinum deposition, (b) after activation (c) after ex-situ durability analysis. The scale bar indicates 500 counts of intensity

After achieving equivalent results on commercial gold thin film as on e-beam evaporated gold, we further studied the ex-situ durability of platinum atomic overlayers on commercial silver thin film. Silver is a reacting electrode; unlike gold, it can undergo corrosion, dissolution and oxide formation, as shown in the pourbaix diagram (Figure 5.3). Therefore, a modified potential deposition scheme is required to prevent the galvanic displacement of the silver substrates by the Pt^{2+} electrolyte, which could otherwise happen at open circuit potential conditions.

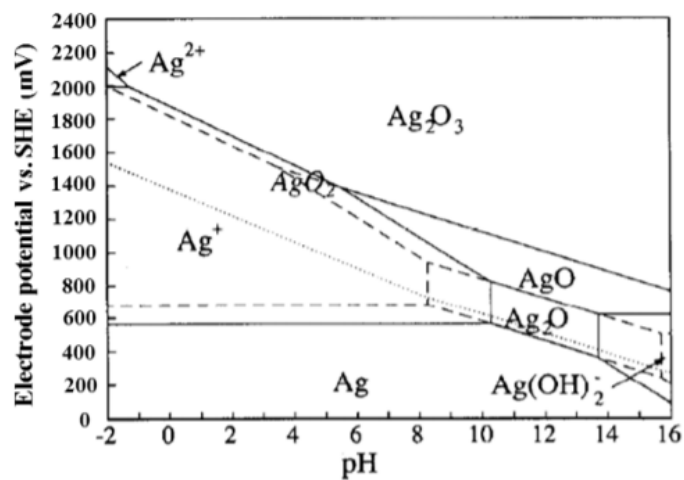


Figure 5.3: Pourbaix diagram of silver[5]

The potential profile of platinum deposition on silver thin film was studied by linear sweep voltammetry. The potential was scanned at 2 mV/s from 0.76 V to -0.64 V in 3 mM K₂PtCl₄ + 0.5 M KCl. The peak at around 0.35 V represent AgCl formation (see Figure 5.4(a)). As the potential is continued, the similar-

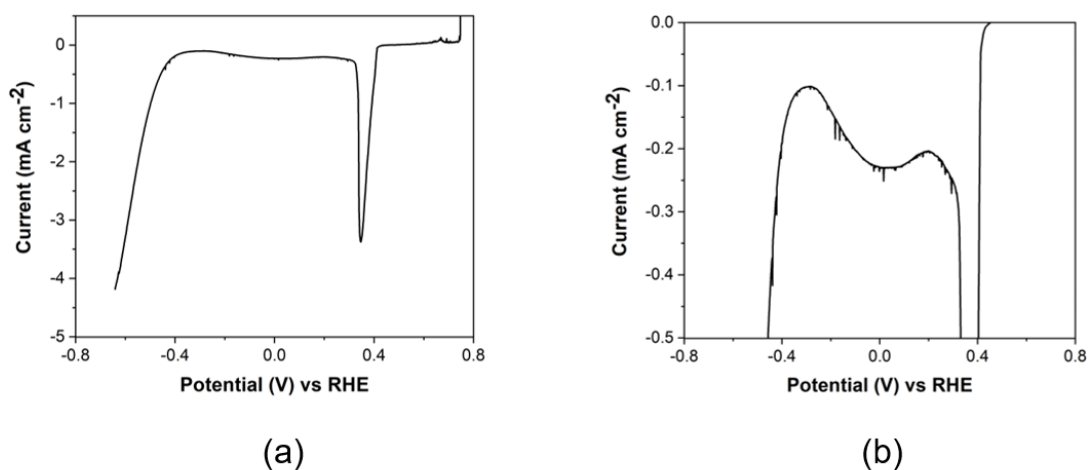


Figure 5.4: (a) Linear sweep voltammetry of platinum electrodeposition on silver thin film at 2 mV/s scanrate and in 3 mM K₂PtCl₄ + 0.5 M KCl(b) zoomed in graph of the same

looking self-terminating behavior like that of in the case of evaporated gold is seen at around -0.3 V (see Figure 5.4(b)).

In the modified deposition, the specimen is immersed at a fixed potential of -0.33 V, where self-terminating deposition occurs. Immediately after the deposition. The sample was then rinsed with DI water to remove the clinging PtCl_4^{2-} electrolyte meniscus. This was necessary to avoid extra platinum deposition that would otherwise deposit as the open circuit potential drifts through the regime where conventional platinum overpotential deposition happens. In the case of gold, this risk is circumvented by stepping the potential to 0.87, while for the silver substrate, the additional risk of localized pitting corrosion in the chloride-rich electrolyte limits the possibility of stepping the electrode to such positive potential values. More so, the possibility of galvanic displacement between PtCl_4^{2-} and the silver substrate must be avoided, and therefore the samples were rinsed as soon as the potential control was released.

As described in the previous chapter, we got durable platinum overlayers with eight cycles of platinum deposition on the evaporated gold substrate. So, we started our studies of platinum on a silver thin film with eight pulses. The adsorbed K_2PtCl_4 was removed by rinsing the sample with DI water immediately after taking the sample out of the electrochemical cell. The platinum loading calculated from the area under the chronoamperometry curve was $54.83 \pm 5.52 \text{ } \mu\text{g cm}^{-2}$, while that measured from ICP-OES was $52.1 \pm 3.7 \text{ } \mu\text{g cm}^{-2}$.

The platinum deposited silver thin film has silver in excess, which is prone to leach. This excess silver was gotten rid of by sequentially increasing the right side of the potential limit during CV for 10 cycles each. As the maximum potential limit is increased from 0.55 V to 0.95 V, there was an increase in the

current due to silver dissolution. The leaching reduced sequentially with increased max potential limit, as the excess silver kept getting dissolved. Further, the platinum CV signature could be obtained when the maximum potential limit was kept at 1.25 V, as shown in Figure 5.5.

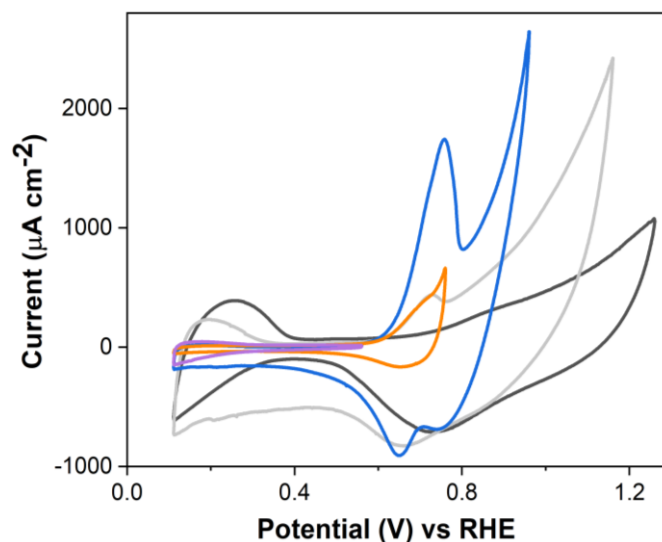


Figure 5.5: Sequential activation of platinum overlayers on silver thin film

The activated sample was subjected to the ex-situ durability analysis by subjecting them to triangular wave potential load cycling. Their performance in the CV and ECSA retention as a function of the number of durability cycles is shown in Figures 5.6(a) and(b). The increase in ECSA initially represents an increase in activity due to activation. The activated platinum thin film was durable in the triangular load cycling waves with no activity degradation.

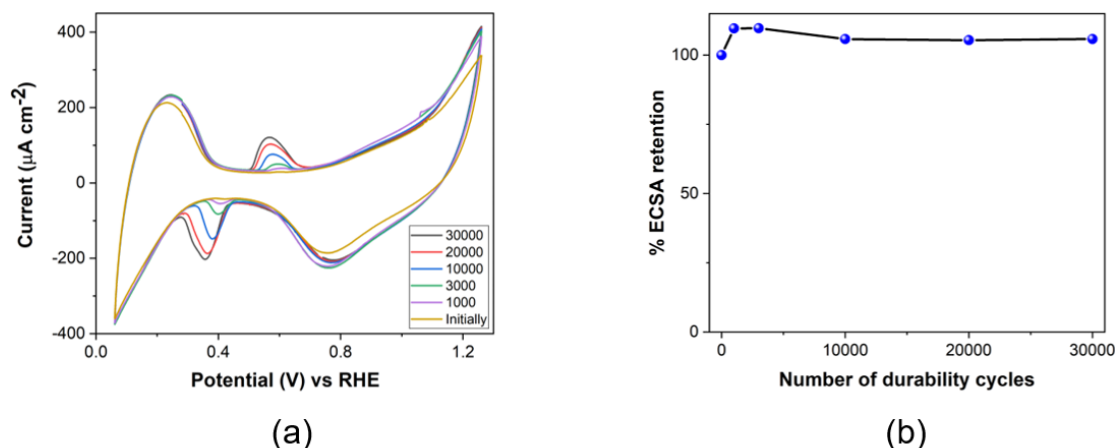


Figure 5.6: (a) CV performance of platinum overlayers on silver thin film (b) its performance as a function of number of durability cycles

These samples were further subjected to more stringent potential load cycling with square wave potentials[3], which consisted of a square potential wave between 0.6V to 0.95 for 3 s each and represents a harsher environment for degradation. The activity retention for such square wave load cycling is shown after 30k durability cycles are 81.5%, with the ECSA of $4.65 \text{ m}^2/\text{gPt}$ (Figure 5.7(a)), which was well above the DOE target of $>60\%$ initial retention. The relatively low ECSA value can be attributed to the flat nature of the silver thin film. The extra set of peaks in the silver thin film substrate case is related to the formation of AgCl [4]. Similarly, we subjected the eight cycled platinum overlayers on a gold thin film to the ex-situ durability analysis in square wave potential load cycles. The sample showed an initial ECSA of $2.37 \text{ m}^2/\text{gPt}$, with 53.1% of ECSA retention at the end of 30k durability cycles. Its performance retention is shown in Figure 5.7(b).

The sheet resistance for eight pulses of platinum overlayers on silver thin film increased by magnitude after each step, as shown in Table 5.1. By the time it completes the durability analysis, the resistance is ~ 2000 ohms/sq. The sheet resistance reduces after platinum deposition for eight pulses of platinum overlayers on gold thin film. This could be because more conductive channels yield a better conducting path. However, beyond platinum deposition, the sheet resistance increases slightly but remains within the same order of magnitude, i.e., < 10 ohms/sq. (see Table 5.1). This indicated that platinum overlayers on silver thin film give good ECSA retention, while gold thin film provides good conductivity retention.

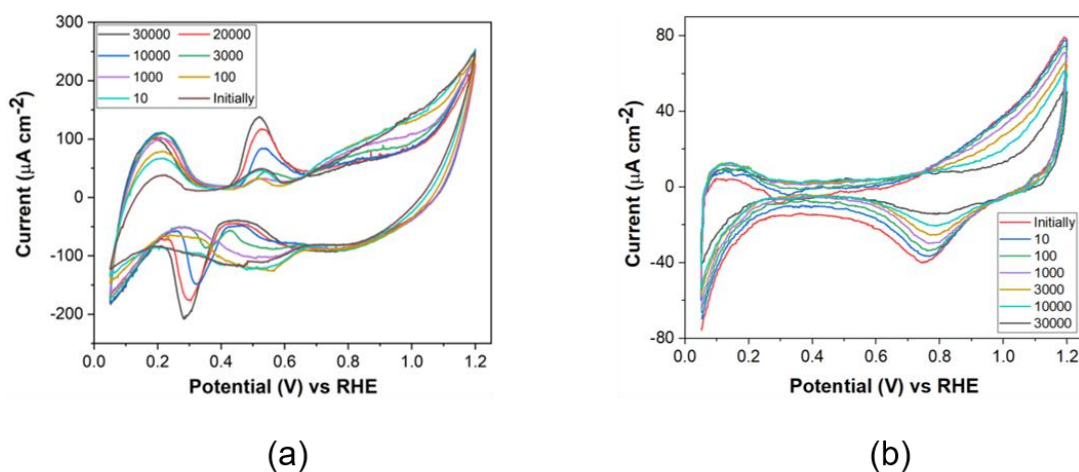


Figure 5.7: Ex-situ durability analysis for eight pulses of platinum overlayers on (a) silver thin film, at 50 mV s^{-1} scan rate in 0.1 M HClO_4 (b) gold thin film, at 20 mV s^{-1} scan rate in 0.1 M HClO_4

Table 5.1: Sheet resistance measurement for platinum overlayers on silver and gold thin films

Sample description	State of the sample	Sheet resistance (ohms/sq.)
Platinum overlayers on silver thin films	Silver thin film	0.94
	After platinum deposition	10.98
	After activation	1078.38
	After durability	~ 2000
Platinum overlayers on gold thin films	Gold thin film	11.10
	After platinum deposition	2.02
	After activation	2.17
	After durability	5.58

For platinum overlayers on silver thin films, the measured platinum loading was $48.1 \pm 4.7 \text{ } \mu\text{g cm}^{-2}$ after activation, while after square wave ex-situ durability analysis, it was $27.7 \pm 4.3 \text{ } \mu\text{g cm}^{-2}$. The % mass retention of platinum after durability analysis was $53.2 \pm 9.7\%$. The platinum dissolution was also characterized in EDS, where the Pt/Ag elemental ratio increased from 0.13 ± 0.04 after synthesis to 0.51 ± 0.29 after activation. It further increased to 1.47 ± 0.18 after durability analysis, proving the subsequent leaching during the durability analysis.

The platinum deposition on silver thin film was characterized through the SEM-EDS. The pristine silver thin film surface morphology is shown in Figure 5.8(a). At the same time, after platinum deposition, it forms bulgy structures of platinum, leaving some holes, which dissolve the underlying silver (Figure 5.8(b)). The bulgy morphology of platinum increases after durability analysis, along with the leaching of the underlying silver base (Figure 5.8(c)).

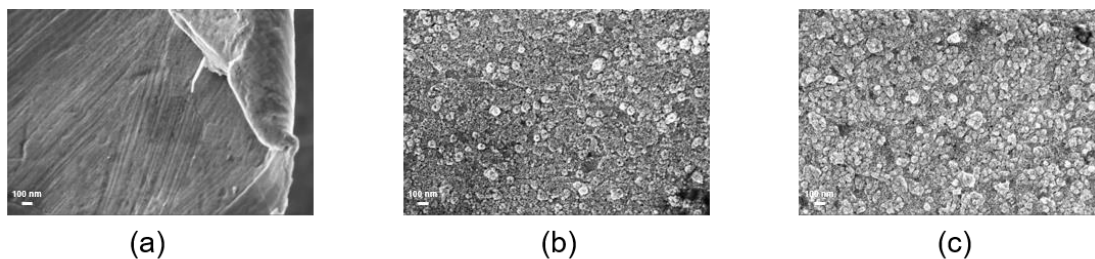


Figure 5.8: Surface morphology of (a) silver thin film (b) platinum deposited on silver thin film (c) after durability analysis

The platinum content at different stages in the sample was measured using EDS, as shown in Table 5.2. The element% of silver reduces drastically from platinum deposition to activation due to silver leaching, which probably also takes platinum along. However, a small fraction of platinum dissolution (73.2% retention for spot 1 and 88.1% retention for spot 2 compared to Pt% after activation) matches closely with that %ECSA retention.

Table 5.2: Elemental analysis for platinum deposition on silver thin film

	Element% after platinum deposition		Element% after activation		Element% after ex-situ durability analysis	
Element	Spot 1	Spot 2	Spot 1	Spot 2	Spot 1	Spot 2
Ag	89.82	89.50	2.32	2.47	0.60	0.61
Pt	10.18	9.26	1.64	1.26	1.20 (73.2% of 1.64)	1.11(88.2% of 1.26)
Ag/Pt	8.82	9.67	1.41	1.96	0.50	0.55
Pt/Ag	0.11	0.10	0.71	0.51	2.00	1.82

XPS confirmed the oxidation state of the deposited platinum at different stages. As shown in Figure 5.9(a), a platinum-rich top surface is formed after platinum deposition, with Ag/Pt3d_{5/2} peak at 368.8 eV and Ag3d_{5/2} peak at 368.1 eV.

After activation (see Figure 5.9(b)), a significant portion of Ag is oxidized to Ag(+1), and both of their presence were detected with Ag3d_{5/2} peak at 368.2 eV and Ag(+1)3d_{5/2} peak at 367.8 eV. After ex-situ durability analysis, all the silver has oxidized to Ag(+1), with its 3d_{7/2} peaks at 367.7 eV and 367.9 eV, respectively(see Figure 5.9(c)). However, platinum remains in the metallic state throughout the experiment (see Figure 5.9(d) to (see Figure 5.9(f)). The ratio of area under the curve for Ag to Pt XPS peaks was 0.08, much less than that detected using EDS (See Table 5.2). This could be due to more platinum height than XPS's penetration depth. Because the EDS could penetrate to micron level thickness, it detects more platinum. However, after the ex-situ durability analysis, the ratio of area under Ag to Pt in XPS is 0.50, which matches quite closely to that detected in EDS, indicating a very thin platinum film (<10 nm) on silver would have formed.

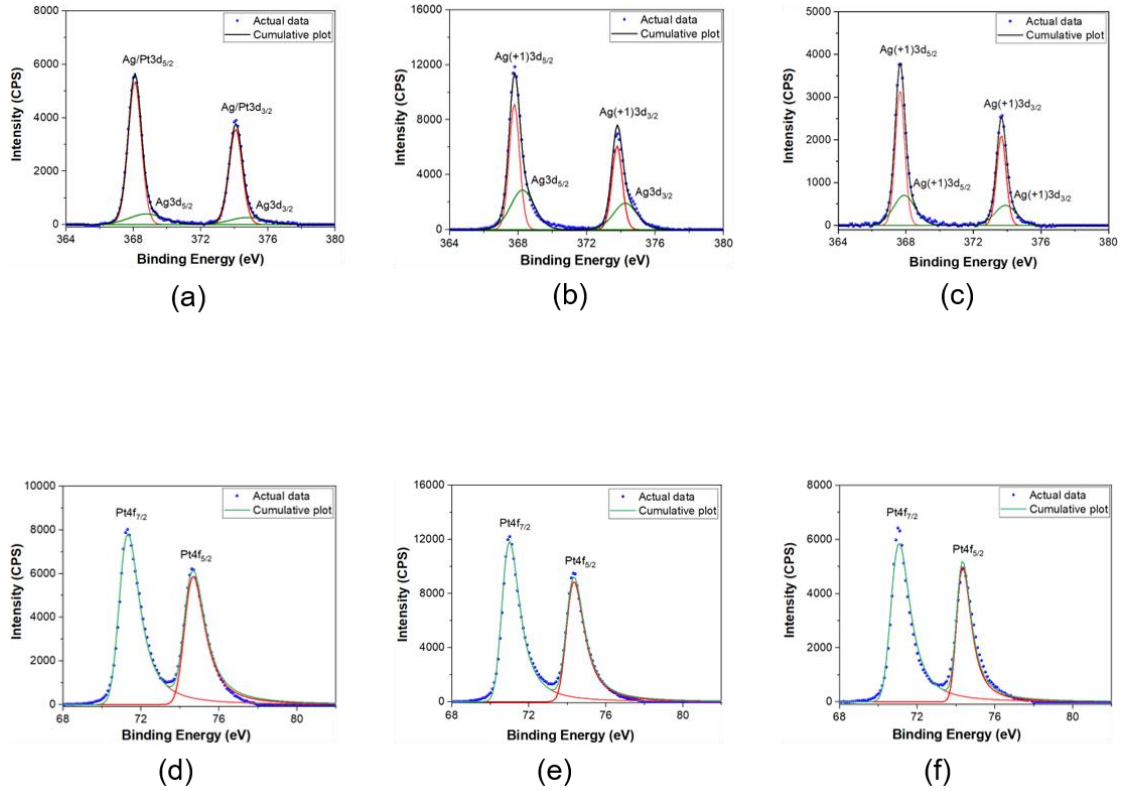


Figure 5.9: XPS for platinum overlayers on silver thin film (a) $\text{Ag}3d_{5/2}$ and $\text{Ag}3d_{3/2}$ after platinum deposition (b) $\text{Ag}3d_{5/2}$ and $\text{Ag}3d_{3/2}$ after activation (c) $\text{Ag}3d_{5/2}$ and $\text{Ag}3d_{3/2}$ after ex-situ durability analysis (d) $\text{Pt}4f_{7/2}$ and $\text{Pt}4f_{5/2}$ after platinum deposition (e) $\text{Pt}4f_{7/2}$ and $\text{Pt}4f_{5/2}$ after activation (f) $\text{Pt}4f_{7/2}$ and $\text{Pt}4f_{5/2}$ after ex-situ durability analysis

The possibility of galvanic displacement of silver thin film by platinum was studied by immersing them in the platinum solution at the open circuit condition for 400 s. The total time for galvanic displacement was kept similar to that of 8 pulses of platinum deposition of 50 s of each pulse. As seen in Figure 5.10(in comparison to the pristine silver thin film in Figure 5.8(a)), the surface morphology of the silver thin film appears to be changed, perhaps due to pitting corrosion from the Cl^- rich environment of K_2PtCl_4 . The galvanically displaced platinum particles are also in smaller sizes than for the sample where platinum was deposited using STED(Figure 5.8(b) for comparison).

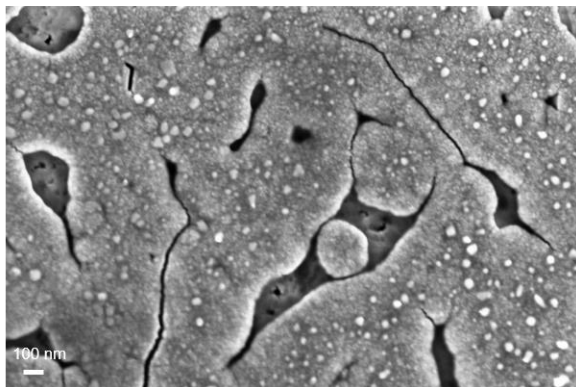


Figure 5.10: Surface morphology of silver thin film after immersing in 3mM K_2PtCl_4 + 0.5M KCl for 400 s at OCP

The amount of platinum deposited was compared by galvanic displacement for two spots, shown in Table 5.3. Compared to platinum deposition using STED, where the Pt/Ag ratio is 0.10 and 0.11 at two different spots, the platinum deposition without any potential application has a lower Pt/Ag ratio value, which was 0.04 at both spots. Assuming no silver leaching happens during the galvanic displacement, the galvanic displacement contributes $\sim 40\%$ of the platinum deposition compared to STED. The 400 s time was needed to give a 40% contribution of platinum. So, if it is assumed that before and after the potential control in each potential deposition pulse, 2 s of time lapses, then also eight pulses would take 32 s, which would be only $\sim 3.2\%$ of the platinum deposited with the potential pulsing.

The oxidation state of the silver was checked by the XPS, where the peak corresponding to $\text{Ag}3d_{5/2}$ comes at 368.2 eV, corresponding to the metallic silver after galvanic displacement. This indicates that the oxidation of the silver would happen due to potential cycling. The $\text{Pt}4f_{7/2}$ peak was at 70.5 eV, corresponding to the metallic state, eliminating the possibility of adsorbed K_2PtCl_4 manifesting in XPS. The ratio of area under the curve in XPS for Pt to Ag is 0.10, which

indicates that the deposited platinum thickness is more than the penetration depth of XPS signals.

Table 5.3: Element % of silver and platinum after galvanic displacement

Element	Element% after galvanic displacement	
	Spot 1	Spot 2
Ag	50.76	93.46
Pt	2.06	3.54
Pt/Ag	0.04	0.04

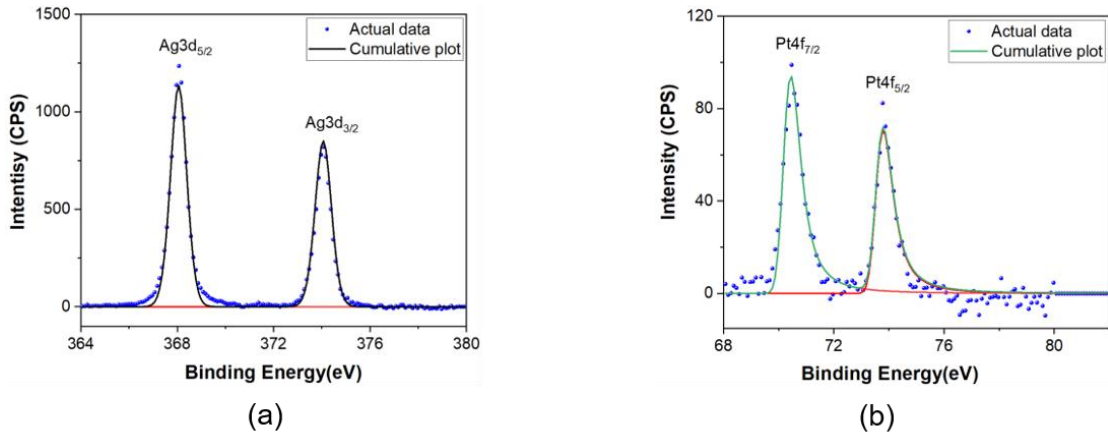


Figure 5.11: XPS spectra of (a) $\text{Ag}3d_{5/2}$ and $\text{Ag}3d_{3/2}$ (b) $\text{Pt}4f_{7/2}$ and $\text{Pt}4f_{5/2}$ after galvanic displacement

The platinum overlayers on silver thin films were also characterized using XRD. The scan rate was kept at 0.2 degrees per minute, and the angle was scanned from 25 to 50 degrees in grazing incidence mode at a 0.5-degree grazing angle. As shown in Figure 5.12(a), the sample has peaked at 38.2° and 44.3° , which

correspond to Ag(111) and Ag(200), respectively (JCPDS #00-087-0720).

Whereas, the

Pt(111) peak at 39.2° is shifted towards Ag(JCPDS #00-004-0802). After the durability analysis (Figure 5.12(b)), the peaks at 27.8° , 32.2° and 46.2° corresponds to AgCl(111), AgCl(200) and AgCl(220) (JCPDS #00-031-1238) arise. So, the AgCl redox peaks found during CVs of ex-situ durability analysis were also characterized by XRD here.

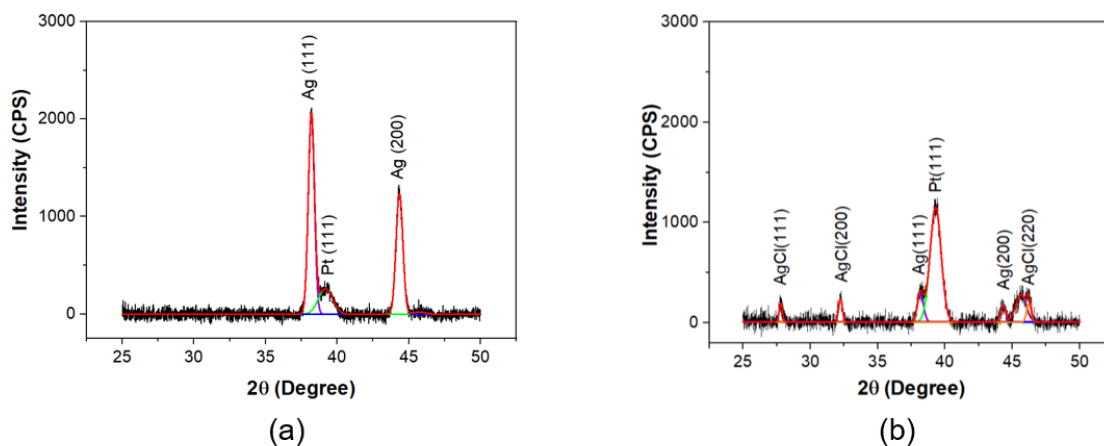


Figure 5.12: XRD of platinum overlayers on silver thin films (a) after platinum deposition (b) after ex-situ durability analysis

5.3 Summary

The preliminary experiments with e-beam evaporated silver showed delamination of silver thin film, to avoid which platinum deposition studies were done on commercial silver thin films. The equivalency of the thin films to that of e-beam evaporated substrate was checked by comparing the %ECSA lost during the potential triangular cycles for 20 and 12 cycles of platinum and

platinum loading calculated from ICP-OES for eight cycles on gold thin films with that of for 20, 12 and 8 cycles of platinum overlayers on e-beam evaporated gold. The silver substrate also shows a similar potential deposition profile and self-termination to the gold substrate. The STED protocol was appropriately modified for platinum deposition to avoid galvanic displacement and pitting corrosion of the silver substrate. The excess silver was leached by potential cycling to achieve platinum thin film on silver, which was exceptionally durable in the triangular potential cycle.

Further, we applied harsher durability potential cycling for 12 and 20 cycles of platinum overlayers on gold thin film. We found that the %ECSA retention was lower with the square wave potential cycling and more with triangular wave potential cycling. At the end of the ex-situ durability analysis, the entire silver was converted to Ag(+1), while the platinum maintained its metallic state. The XRD also confirms Ag(+1) after durability analysis and has peaks for AgCl. The platinum deposition without potential application is ~40% more than that of platinum deposition with the potential application. Interestingly, all the silver and platinum remain metallic throughout the galvanic displacement experiment, proving that no silver oxidizes without application of potential cycling or no adsorbed K₂PtCl₄ remains. The platinum deposition before the potential starts and after the platinum sample is taken out of the electrochemical cell after losing the potential control was negligible (~3.2% of the platinum deposited during potential deposition). The silver thin film had an excellent ECSA retention, while the gold thin film had excellent conductivity retention.

5.4 References

- [1] J. Perelaer, R. Jani, M. Grouchko, A. Kamyshny, S. Magdassi, and U. S. Schubert, “Plasma and microwave flash sintering of a tailored silver nanoparticle ink, yielding 60% bulk conductivity on cost-effective polymer foils,” *Adv. Mater.*, vol. 24, no. 29, pp. 3993–3998, 2012, doi: 10.1002/adma.201200899.
- [2] X. Cao *et al.*, “PtAg bimetallic nanowires: Facile synthesis and their use as excellent electrocatalysts toward low-cost fuel cells,” *Nano Energy*, vol. 12, pp. 105–114, Mar. 2015, doi: 10.1016/j.nanoen.2014.12.020.
- [3] M. Uchimura and S. S. Kocha, “The Impact of Cycle Profile on PEMFC Durability,” *ECS Trans.*, vol. 11, no. 1, pp. 1215–1226, Sep. 2007, doi: 10.1149/1.2781035.
- [4] B. J. Plowman, B. Sidhureddy, S. V. Sokolov, N. P. Young, A. Chen, and R. G. Compton, “Electrochemical Behavior of Gold-Silver Alloy Nanoparticles,” *ChemElectroChem*, vol. 3, no. 7, pp. 1039–1043, Jul. 2016, doi: 10.1002/celec.201600212.
- [5] P. Delahay, M. Pourbaix, and P. Van Rysselberghe, “Potential-pH Diagram of Silver Construction of the Diagram—Its Applications to the Study of the Properties of the Metal, its Compounds, and its Corrosion,” *J. Electrochem. Soc.*, vol. 98, no. 2, p. 65, 1951, doi: 10.1149/1.2778107.

Chapter 6

Platinum atomic overlayer deposition on silver nanostructures

6.1 Introduction

In PEMFCs, the conventional electrocatalyst is an amalgamation of Nafion solution, platinum nanoparticles and carbon base. Conventionally, this catalyst is hot pressed onto the Nafion membrane and sandwiched between the gas diffusion layer (GDL). Techniques like doctor blade deposition, screen printing and brush painting are used to prepare the catalyst layer. Despite being low-cost and straightforward to implement, these techniques suffer from several problems, including lack of uniformity over the large scale, lengthy processing times, or requirement for iterations of steps like painting, drying and massing [1]. The advanced versions of these deposition techniques, like spray painting, lead to more uniformity of catalyst deposition than brush painting. Still, it can prove to be a costly technique because of the clogging of the catalyst in feed lines, leading to aggregate deposition. So, there exists a good scope for simplifying the present catalyst coating system of PEMFC.

The fabrication process and microstructure of electrodes govern the efficiency of the Platinum electrocatalyst in PEMFC. There have been approaches other than the conventional methods like screen printing, spray painting and brush painting. These approaches include ion-beam assisted deposition [2], sputtering [3]–[5], pulsed laser deposition [6], electrospraying or electrospinning of ultralow Platinum ([7], [8]) to synthesize electrodes with 0.05-0.4 mg/cm² platinum

loading [9]. There were several attempts made in the direction of decreasing mass transfer resistance in the fuel cell by redesigning the gas diffusion layer (GDL) by sputtering a metal mesh as a GDL [10], electroactive 3-D membrane [11] and utilizing a porous metal foam for transporting oxygen [12]. Debe et al. [13] have developed NSTF electrodes by vacuum deposition of platinum onto a nanostructured organic layer, formed by sublimation and deposition of an organic precursor. The requirement of vacuum equipment for the 3M processes of fabricating NSTF allows scope for further improvement.

Inkjet printing is an attractive additive process for fabricating NSTFs. It has a drop-on-demand (DOD) technology, where ink droplets are ejected from a small hole in the printhead, owing to pressure developed from the electronic signal to a printhead. This process offers adaptability to various substrates, high precision, excellent resolution, accuracy and a small footprint. As such, inkjet printing has been studied by several groups ([1], [14]). But, most use complicated ink-formulation or post-synthesis steps like sintering for fabricating conductive structures.

Contrary to this, inkjet printing of metal salts provides a straightforward and robust way to have the controlled synthesis of conductive metal substrates on flexible substrates like paper [15], PET [16] and cloth fabric [17]. This method avoids the need for expensive colloidal catalyst ink formulation or post-processing. Our group has developed a simple process for fabricating nanostructured metallic thin films on paper and plastic substrates using a simple desktop inkjet printer ([Media Highlight-Science Monitor, DD Rajya Sabha TV, 08/08/2015](#)). The process chemistry is based on the well-developed silver halide chemistry used in the field of photography([15], [18]) and is capable of synthesizing silver nanostructures with less than 1 μm thickness. So,

considerable scope exists for this method to be utilized for the in-situ synthesis of silver nanostructures on Nafion membrane, which could be used as a conductive, porous base to deposit platinum overlayers.

6.2 Inkjet printing of silver nanostructures on Nafion membrane

6.2.1 Nafion membrane structure

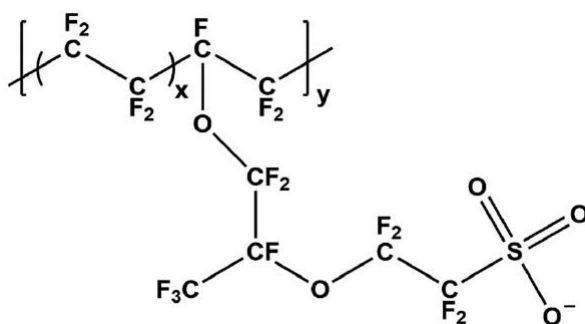


Figure 6.1: Chemical structure of Nafion membrane [19]

Nafion membrane is the most common proton exchange membrane used in PEMFC. It allows only protons to pass through from anode to cathode while forcing the electrons to flow through the external circuit. Nafion membrane can hold water, which makes sulphonic acid groups hydrated, and the hydrated protons can move within the Nafion, making it an excellent proton conductor[19]. As shown in Figure 6.1, Nafion has sulphonic acid functionalized end groups, which makes it a super acid with proton conductivity up to 0.1 S cm⁻¹. This structure is highly stable (Figure 6.1) and resistant to acid attack

due to the presence of CF_2 groups, which leads to an increased lifetime of the PEMFC.

6.2.2 Preparation of Nafion membrane substrate

Nafion[™] NR211 membrane was received from National Chemical Laboratory (NCL), Pune, India. Nafion membrane does not exhibit sufficient hydrophilicity for directly spreading metal salt solutions via inkjet printing. Preliminary experiments were attempted to render the Nafion 211 membrane hydrophilic enough for the salt solution to spread on top of it. In the successful approach, it was pre-treated with a plasma exposure (Harrick plasma PDC-32G-2 230V). Plasma treatment activates the surface. To leverage the activated surface after plasma cleaning, the plasma-treated Nafion membrane pieces were dipped in polyelectrolyte solutions to form a hydrophilic layer. Wang et al. [20] and Cheng et al. [21] have also shown that the layer-by-layer (LBL) assembly of polyelectrolyte (PEL) films can improve the adhesion of the metal lines fabricated by inkjet printing. These PEL films can be applied via simple methods like dip-coating, spray coating, and spin coating [22]. The polyelectrolyte dissociates in water and produces charged species. Layer by layer deposition of polyelectrolyte multilayers (PEMs) was performed by alternatively coating plasma-treated Nafion membrane with the positive and the negative polyelectrolyte. During each PEL deposition, polymer chains are adsorbed on the substrate, and the surface charge is reversed. Thus, an electrostatically crossed film is built up. To make the film porous enough for the passage of reactants and products, 1.5M NaCl was added to the polycationic and the polyanionic solution. The addition of salt helps in charge

screening and leads to thicker PEL films than PEL films formed without salt addition [23]. PEL film morphology changes with different pH of the polyelectrolyte solution because of pH-dependent ionization. Application of catalyst layer for fuel cell needs sustainability in the highly acidic environment and firm adherence of the nanostructured film on the Nafion membrane. So, Polycation - [poly (diallyl dimethyl ammonium chloride)] PDDA and Polyanionic [poly (sodium styrene sulfonate)] PSS, being strong electrolyte with no pH-dependence, were chosen for coating onto plasma-treated Nafion membrane. The optimization of number of PEL layers and platinum loading was done by ensuring no leaching, as detailed in Appendix A.

6.2.3 Inkjet printing

Inkjet printing is frequently used for producing conductive structures on different substrates. Most of these attempts use dimatix(material) printers, where a silicon needle is used for dispensing colloidal particles ([2], [14]), but it is quite costly. Furthermore, most reports on using inkjet printing require the formulation of the ink for inkjet printing by adjusting their viscosity and surface tension as well as the addition of the external bonding agent ([16], [17], [1], [24], [20]), which is a time consuming and a tedious process. Instead, metal salt solutions can be directly printed ([15], [25]) to yield conductive patterns avoiding the need for additives or extra steps. Therefore, an attempt was made to directly adapt the “print-expose-develop” technique for the In-situ synthesis of silver nanostructures on the Nafion membrane so that the traditional decal transfer method can be eliminated the catalyst layer can be directly printed onto the Nafion membrane.

All solutions were prepared in DI water (MilliQ system, a resistance of 18.2 M Ω .cm @ 25°C). The molar ratio of AgNO₃: KX was kept as 1:2 so complete silver halide conversion could occur. To enhance photosensitivity, 5% potassium iodide (KI) is mixed with 95% potassium bromide (KBr) [26]. Silver halide is formed by the reaction between printed silver nitrate and potassium halide. A halogen lamp (Crompton Greaves - Model # J240V, 500 W, R7S, 9500 Lumens) was used to reduce the as-printed silver halide. For developing the silver clusters, the D-76 developer was used. D-76 developer is made by dissolving 100 g sodium sulphite, 2 g metol, 5 g hydroquinone and 2 g of borax in 1000 ml of DI water.

An HP Deskjet 1112 printer (cost \sim 2000 INR) was used for printing salt solutions sequentially. Separate HP 803 cartridges (cost \sim 700 INR) were used for printing AgNO₃ and KX. The cartridges were emptied, and their black ink was washed entirely with the tap water. They were printed on blank paper until all the residues of the black ink were removed from the cartridge. Salt solutions of silver nitrate and potassium halide were successively printed to make silver halide. It was subsequently kept under a halogen lamp at 50 cm for 15 minutes to reduce the silver halide to form “latent” silver clusters. Photons from the halogen light eject electrons from the halide, which initiates the reduction reaction to produce a permanent image by building latent image centres (a group of 4-5 silver nuclei). Finally, the exposed sample was placed in the developer solution for 15 minutes to reduce silver salt to form nanostructures completely*. The sample was washed in water for 15-20 minutes to clean the silver nanowire sample. The reactions are as shown in equations (6.1) and (6.2),

* For Nafion membrane substrate; care should be taken while developing the silver nanowire sample by placing developer drop by drop; otherwise, the uniform film will not form.

respectively (where X refers to halide, either bromide or iodide), and the schematic of the "print-expose-develop" process is shown in Figure 6.2.

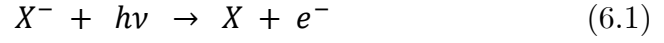


Figure 6.2: "Print-expose-develop" technique for the In-situ synthesis of silver nanowire [15]

The digital photograph of the developed silver nanowire on the Nafion membrane is shown in Figure 6.3(a). FESEM images (using Zeiss Ultra 55 FESEM) were obtained to check the surface morphology of the silver printed Nafion membrane. As shown in Figure 6.3(b), uniform coverage of nanowires on the entire surface with diameters in the 70-160 nm range was obtained. The percolating network of silver nanowires is the reason behind the excellent conductivity of the sample. The presence of silver was confirmed by the EDS analysis.

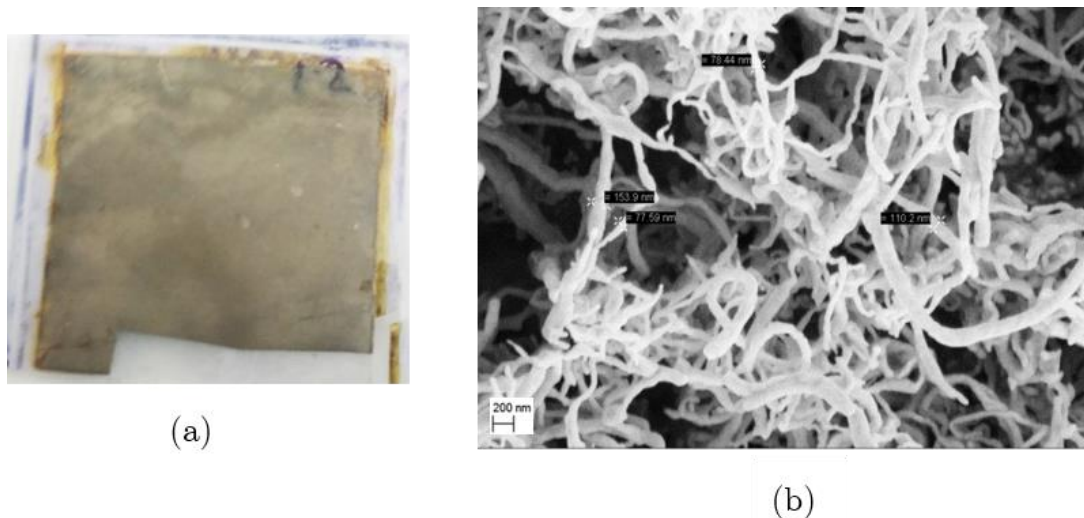


Figure 6.3: (a) Digital photograph of silver nanowire on Nafion membrane (b) FESEM image of silver nanowire on Nafion membrane (conductivity < 5 ohm/sq.)

6.3 Platinum overlayer deposition using STED on Ag nanowire

The modified platinum deposition protocol was used to deposit overlayers of platinum on silver nanowire structures (silver loading of 2 mg cm^{-2} , substrate chromatography paper). 8 pulses of platinum were deposited using STED on the silver nanowire. Unlike the case of silver foil or evaporated gold case, the area under the chronoamperometry peaks is relatively high ($17.64 \text{ } \mu\text{g cm}^{-2}$ per pulse), which can be because of either having more platinum deposition due to increased surface area or due to some unwanted reactions happening from the residual salts during development step. However, we need to back this with the loading measurement from ICP-OES. The as-synthesized sample was subjected to ex-situ durability analysis, which was found to be durable only for 1000 cycles (Figure 6.4). The area under the H_{upd} desorption peak was $1403.1 \text{ } \mu\text{C cm}^{-2}$, and the corresponding ECSA was $4.73 \text{ m}^2 \text{ g}_{\text{Pt}}^{-1}$.

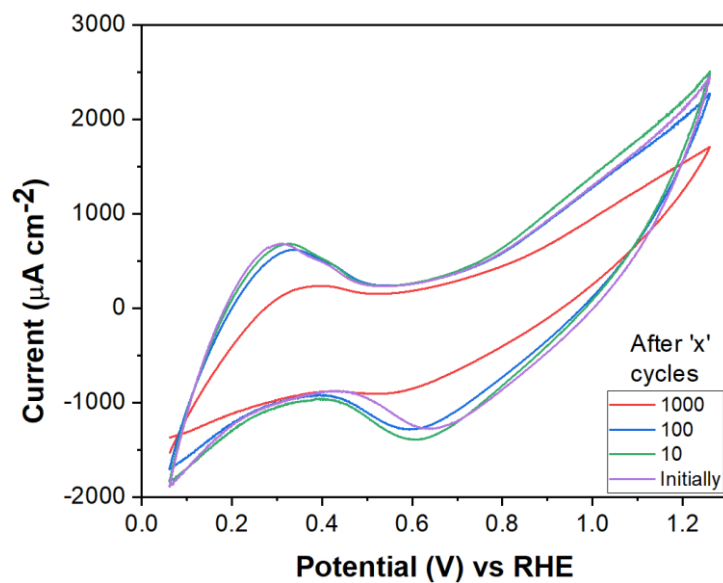


Figure 6.5: The cyclic voltammetry of platinum overlayers coated on silver nanowire on chromatography paper

The effect of silver loading was understood by observing the CV signatures of the platinum overlayers with different silver loading. As shown in Figure 6.5, the platinum overlayer gives better CV signatures for 2 mg cm^{-2} silver loading than that with 1 mg cm^{-2} loading as the conductive backbone.

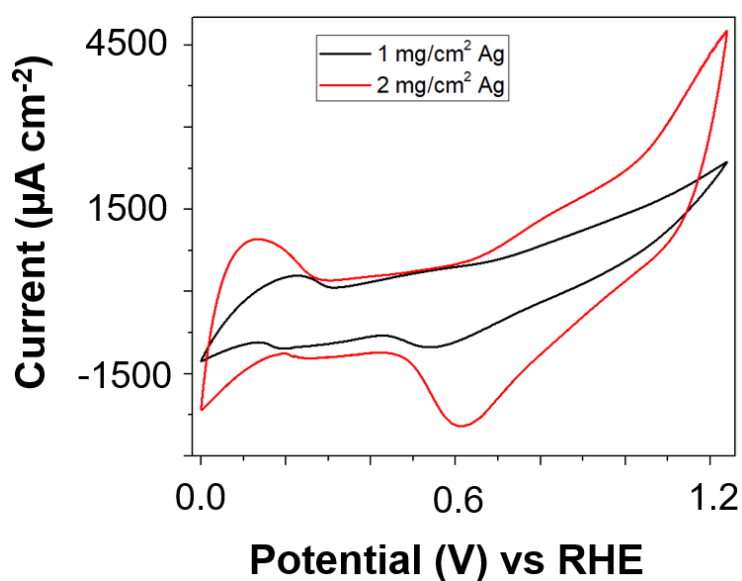


Figure 6.4: Effect of silver loading on platinum overlayer performance

We have also tried preliminary experiments with platinum overlayers on the Nafion membrane. We could successfully deposit platinum (detected using EDS); however, it was not electrochemically active (Figure 6.6). The atomic % of platinum after deposition and after the CV was measured in EDS and documented in Table 6.1. The Pt/Ag atomic% ratio reduces after the CV, indicating the leaching of the silver.

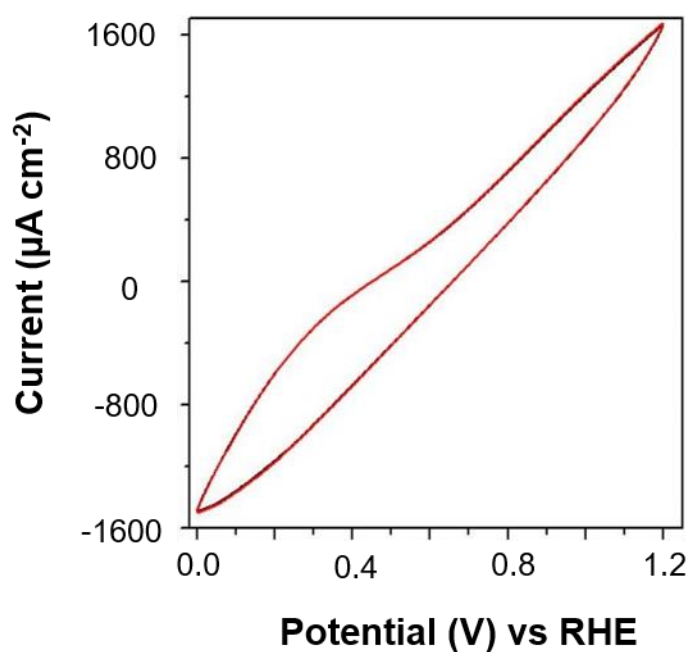


Figure 6.6: CV of platinum overlayers on silver nanowire on Nafion at 50 mV s⁻¹ in 0.1M HClO₄

Table 6.1: Atomic% of elements after platinum deposition and after CV

Element	Atomic% (After platinum deposition)	Atomic% (After CV)
Cl K	0.87	1.76
Ag L	88.09	78.42
Pt M	7.79	16.26
Au M	3.24	3.55
Ag/Pt	11.31	4.82

To understand the reason for inactive silver, we observed its surface morphology change at different stages, i.e. before platinum deposition, after platinum deposition and after cyclic voltammetry. As seen in Figure 6.7(a) to Figure 6.7(c), after platinum deposition, the nanowire structure breaks to some extent, while after the CV analysis, it ultimately makes bulges. The four probe conductivity measurements for two similarly processed samples at different stages are documented in Table 6.2. The resistance does not change much after platinum deposition; however, it varies by order of magnitude after the CV analysis due to the leaching of the silver substrate.

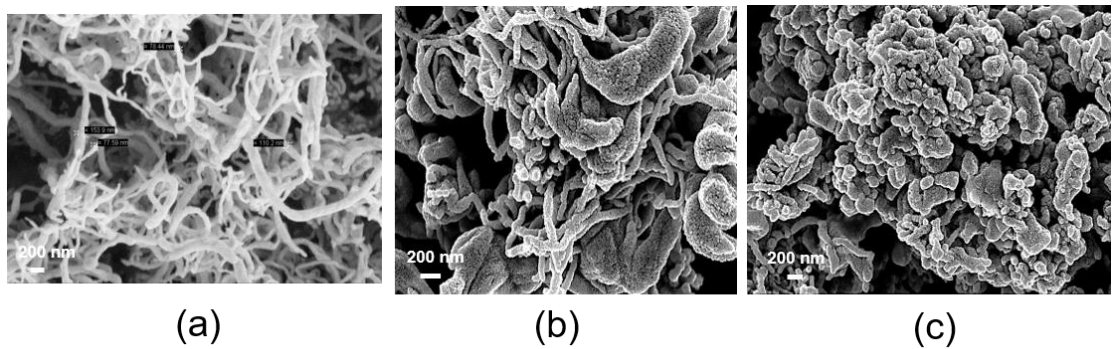


Figure 6.7: Surface morphology evolution of platinum overlayers on silver nanowire (developed on Nafion membrane). (a) before platinum deposition (b) after platinum deposition (c) after CV analysis

Table 6.2: Conductivity of platinum overlayers at different stages

Element	Resistance(ohms/sq.)	
	Sample-1	Sample-2
Before platinum deposition	3.48	3.49
After platinum deposition	13.41	13.55
After CV	552.60	484.74

The stability of developed platinum overlayer coated silver nanowires on the Nafion membrane in acidic solution was checked to eliminate the leaching possibility due to the acidic solution. The samples were dipped in 0.1 M HClO_4 for one hour at OCP and were observed for conductivity changes. However, there was no apparent change in the conductivity (Table 6.3), indicating that the potential cycling distorts the structure and not the acidic environment.

Table 6.3: Resistance variation before and after acid dip for 1 hour in 0.1 M HClO_4 at OCP

	Resistance(ohms/sq.)	
	Sample-1	Sample-2
Before acid dip	3.1	4.4
After acid dip	3.0	4.3

6.4 Summary

Print-expose-develop technique was successfully adapted to the Nafion membrane with appropriate surface modifications. The platinum loading calculated from the area under the chronoamperometry analysis was more than that found for platinum on silver foil or evaporated gold substrate. Despite getting detected in the EDS, the platinum overlayers are not electrochemically

active and form bulged structures. The resistance of these structures increases by order of magnitude after the CV, indicating the leaching of the silver conducting backbone. The leaching of the silver was also characterized using EDS, where Ag/Pt ratio was found to reduce after the cyclic voltammetry. The acid stability analysis at OCP indicated that the silver leaching was related to the potential cycling and not merely due to the acidic environment.

6.5 References:

- [1] A. D. Taylor, E. Y. Kim, V. P. Humes, J. Kizuka, and L. T. Thompson, "Inkjet printing of carbon supported platinum 3-D catalyst layers for use in fuel cells," *J. Power Sources*, vol. 171, no. 1, pp. 101–106, 2007, doi: 10.1016/j.jpowsour.2007.01.024.
- [2] M. S. Saha, D. Malevich, E. Halliop, J. G. Pharoah, B. A. Peppley, and K. Karan, "Electrochemical Activity and Catalyst Utilization of Low Pt and Thickness Controlled Membrane Electrode Assemblies," *J. Electrochem. Soc.*, vol. 158, no. 5, p. B562, 2011, doi: 10.1149/1.3559188.
- [3] S. Mukerjee, S. Srinivasan, and A. J. Appleby, "Effect of sputtered film of platinum on low platinum loading electrodes on electrode kinetics of oxygen reduction in proton exchange membrane fuel cells," *Electrochim. Acta*, vol. 38, no. 12, pp. 1661–1669, Aug. 1993, doi: 10.1016/0013-4686(93)85056-5.
- [4] S. Hirano, J. Kim, and S. Srinivasan, "High performance proton exchange membrane fuel cells with sputter-deposited Pt layer electrodes," *Electrochim. Acta*, vol. 42, no. 10, pp. 1587–1593, 1997, doi: 10.1016/S0013-4686(96)00320-9.
- [5] R. O'hayre, S. J. Lee, S. W. Cha, and F. B. Prinz, "A sharp peak in the performance of sputtered platinum fuel cells at ultra-low platinum loading," *J. Power Sources*, vol. 109, no. 2, pp. 483–493, 2002, doi: 10.1016/S0378-7753(02)00238-0.
- [6] N. Cunningham, E. Irissou, M. Lefèvre, M.-C. Denis, D. Guay, and J.-P. Dodelet, "PEMFC Anode with Very Low Pt Loadings Using Pulsed Laser Deposition," *Electrochem. Solid-State Lett.*, vol. 6, no. 7, p. A125, 2003, doi: 10.1149/1.1574232.

- [7] S. Tada *et al.*, “Long-term durability of Ni/TiO₂ and Ru-Ni/TiO₂ catalysts for selective CO methanation,” *J. Power Sources*, vol. 264, pp. 59–66, 2014, doi: 10.1016/j.jpowsour.2014.04.052.
- [8] S. Martin, P. L. Garcia-Ybarra, and J. L. Castillo, “Electrospray deposition of catalyst layers with ultra-low Pt loadings for PEM fuel cells cathodes,” *J. Power Sources*, vol. 195, no. 9, pp. 2443–2449, May 2010, doi: 10.1016/j.jpowsour.2009.11.092.
- [9] B. Millington, V. Whipple, and B. G. Pollet, “A novel method for preparing proton exchange membrane fuel cell electrodes by the ultrasonic-spray technique,” *J. Power Sources*, vol. 196, no. 20, pp. 8500–8508, 2011, doi: 10.1016/j.jpowsour.2011.06.024.
- [10] B. Dawoud, E. Amer, and D. Gross, “Experimental investigation of an adsorptive thermal energy storage,” *Int. J. energy Res.*, vol. 31, no. August 2007, pp. 135–147, 2007, doi: 10.1002/er.
- [11] F. N. Crespilho, F. C. Nart, O. N. Oliveira, and C. M. A. Brett, “Oxygen reduction and diffusion in electroactive nanostructured membranes (ENM) using a layer-by-layer dendrimer-gold nanoparticle approach,” *Electrochim. Acta*, vol. 52, no. 14, pp. 4649–4653, 2007, doi: 10.1016/j.electacta.2007.01.048.
- [12] R. Chen and T. S. Zhao, “A novel electrode architecture for passive direct methanol fuel cells,” *Electrochem. commun.*, vol. 9, no. 4, pp. 718–724, 2007, doi: 10.1016/j.elecom.2006.11.004.
- [13] M. K. Debe, “Novel catalysts, catalysts support and catalysts coated membrane methods,” in *Handbook of Fuel Cells*, Chichester, UK: John Wiley & Sons, Ltd, 2010, pp. 1–14.
- [14] S. Shukla, D. Stanier, M. S. Saha, J. Stumper, and M. Secanell, “Analysis of Inkjet Printed PEFC Electrodes with Varying Platinum Loading,” *J. Electrochem. Soc.*, vol. 163, no. 7, pp. F677–F687, 2016, doi: 10.1149/2.1111607jes.
- [15] S. K. Parmar and V. Santhanam, “In situ formation of silver nanowire networks on paper,” *Curr. Sci.*, vol. 107, no. 2, pp. 262–268, 2014.
- [16] X. Nie, H. Wang, and J. Zou, “Inkjet printing of silver citrate conductive ink on PET substrate,” *Appl. Surf. Sci.*, vol. 261, pp. 554–560, 2012, doi:

10.1016/j.apsusc.2012.08.054.

- [17] P. Chen, H. Chen, J. Qiu, and C. Zhou, "Inkjet printing of single-walled carbon nanotube/RuO₂ nanowire supercapacitors on cloth fabrics and flexible substrates," *Nano Res.*, vol. 3, no. 8, pp. 594–603, 2010, doi: 10.1007/s12274-010-0020-x.
- [18] P. Joshi and V. Santhanam, "Inkjet-Based Fabrication Process with Control over the Morphology of SERS-Active Silver Nanostructures," *Ind. Eng. Chem. Res.*, vol. 57, no. 15, pp. 5250–5258, Apr. 2018, doi: 10.1021/acs.iecr.7b04663.
- [19] W. S. and L. A. Baker, "Imaging heterogeneity and transport of degraded Nafion membranes," *RSC Adv.*, vol. 5, no. 120, pp. 99284–99290, 2015, doi: 10.1039/c5ra20291d.
- [20] T. C. Wang, B. Chen, M. F. Rubner, and R. E. Cohen, "Selective electroless nickel plating on polyelectrolyte multilayer platforms," *Langmuir*, vol. 17, no. 21, pp. 6610–6615, 2001, doi: 10.1021/la010755z.
- [21] K. Cheng *et al.*, "Ink-jet printing, self-assembled polyelectrolytes, and electroless plating: Low cost fabrication of circuits on a flexible substrate at room temperature," *Macromol. Rapid Commun.*, vol. 26, no. 4, pp. 247–264, 2005, doi: 10.1002/marc.200400462.
- [22] R. A. McAloney, M. Sinyor, V. Dudnik, and M. Cynthia Goh, "Atomic force microscopy studies of salt effects on polyelectrolyte multilayer film morphology," *Langmuir*, vol. 17, no. 21, pp. 6655–6663, 2001, doi: 10.1021/la010136q.
- [23] K. T. Adjemian *et al.*, "Function and Characterization of Metal Oxide–Nafion Composite Membranes for Elevated-Temperature H₂/O₂ PEM Fuel Cells," *Chem. Mater.*, vol. 18, no. 9, pp. 2238–2248, 2006, doi: 10.1021/cm051781b.
- [24] A. Kamyshny, "Metal-based Inkjet Inks for Printed Electronics," *Open Appl. Phys. J.*, vol. 4, no. 1, pp. 19–36, 2011, doi: 10.2174/1874183501104010019.
- [25] P. Joshi and V. Santhanam, "Paper-based SERS active substrates on demand," *RSC Adv.*, vol. 6, no. 72, pp. 68545–68552, 2016, doi: 10.1039/C6RA07280A.

- [26] J. F. Hamilton, *Advances in Physics The silver halide photographic process The silver halide photographic process*, vol. 374, no. 4. 1988.

Appendix A: Fuel Cell station operation

These characterization protocols were performed on commercially obtained catalyst membranes (Nafion 212, 5 cm², Anode catalyst Pt/C (20%) loading of 0.03 mg/cm²) majorly to get used to the equipment capabilities and gain a deeper understanding of the techniques involved.

Safety modifications:

Additions have been made to the test setup with regards to improving the safety aspect. Steel piping has been used for all connections of Oxygen, Hydrogen and Air. Orifice and needle valves, coiled piping has been added to the piping network to prevent high pressure surge affecting the test setup. The Figure A.1 summarizes it.

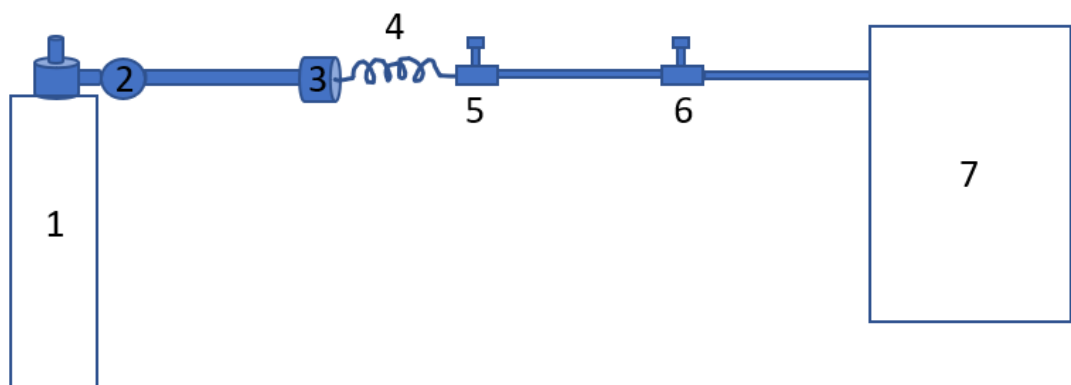


Figure A.1: Setup for fuel cell station in accordance with the safety guidelines

- 1 – Gas Cylinder: The H₂ and O₂ cylinders have to be at least 6 m apart
- 2 - Valve and regulator: The regulator has to be leak proof (one can use the soap bubble test to check its integrity)
- 3 - Size connector: Connector between 6.5 mm steel pipe and 3.5 mm steel pipe
- 4 - Pipe coil to prevent suspension due to sudden pressure surges
- 5 - Orifice valve - If the pressure exceeds a certain value, the cap in the valve comes out, releasing the gas into the atmosphere.
- 6 - Needle valve – provides control over gas flow rate without needing the regulator all the time
- 7 – Fuel cell station setup

These are some major points to keep in mind while operating the test station

1) Start-up –

This includes starting the instrument, setting the gas flows and temperature input.

- After starting the instrument, always wait for 10 minutes before initializing the software. This is to ensure all the interface controls are stabilized. Then set the flow rates as required in the panel and open the cylinders. Always ensure the H₂ detector is on when the system is in operation.
- Temperature control has to be set in a way such that the humidifier temperature is always less than (at least 5⁰ Celsius) the cell temperature and line heater temperature. This is to ensure condensation and flooding inside the cell does not happen initially. It is advisable to let N₂ flow

through both channels during this process to ensure to remove the H₂-O₂ interface arising from the trapped air in shutdown mode.

- Before starting the experiments, always check whether the temperature and flow rates have reached stable points.

2) Shutting down –

While shutting down, always close down the H₂ and O₂ cylinders first. Ensure the N₂ gas passes through the cell to purge the remnant gases and waste (at least 45 minutes). Slowly bring down the cell and anode-cathode temperatures to room, and in the process ensure humidifier temperature is always less than cell temperature to prevent flooding issues.

The following tests were performed on the commercial MEAs.

A) VIRMR Test – We perform VIRMR test in order to obtain the polarization curve (steady state). To perform this test initial conditions were kept as follows:

- Cell temperature = 80 °C
- Anode humidifier temperature = 70 °C
- Cathode humidifier temperature = 70 °C
- Anode preheater temperature = 75 °C
- Cathode preheater temperature = 75 °C
- Flow rate of H₂/O₂ = 50 SCCM/100 SCCM.

Steps are as follows:

- 1) Refer to the video file (VIRMR test folder -- Running VIRMR test).

Note: In the video, delay time is kept as 10 sec for each point but according to the literature it should be kept as 900 seconds. Video gives the general idea about ways of performing VIRMR test. Values of parameters would differ depending on the testing protocols.

- 2) After saving the data as shown in the above video, curve fit the data using Matlab curve fitting tool (for this purpose you can refer to word files with name (VIRMR test folder - a) equations and b) parameters).
- 3) The generated polarization curves are fitted to the given equations to determine the individual losses using Matlab.

$$f(x) = A*\log(x) + B*\log(1/1-(x/J)) + C*x + D.$$

From the above equation (A, B, C, D, J) values are predicted, which are then used to determine the following potential losses –

- Concentration potential: $B*\log(j_l/j_l - x)$
- Activation potential: $a + b*\log(j)$
- $b = -A$ and $a = E_{\text{thermo}} - D$
- J – Limiting current density

- 4) After finding the parameters (A,B,C,D), you can obtain values of different resistances separately.

Important Points:

- If the cell membrane is used after a long duration or if it is a new catalyst, activation and wetting up protocols have to be followed. This is also known as conditioning protocol.
- While changing the cell catalyst, ensure there are no alignment issues. This can be done using a N₂ cylinder to ensure all the flow channels are working properly. While tightening the cell assembly, follow the star pattern in order for the bolts. This is so there are no residual stresses present in the cell, and ensures the torque does not exceed 10 N-m.

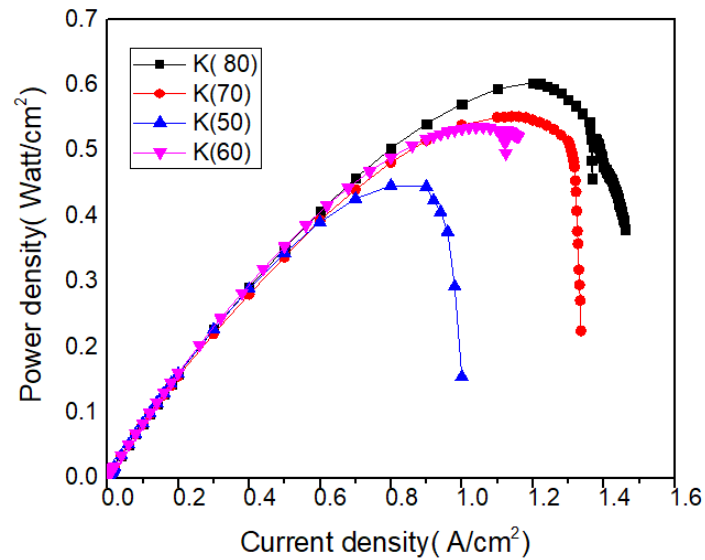


Figure A.2: Polarization curve of commercial Pt/C catalyst

- 3 Impedance – Another method to characterize the losses in the cell is to model the responsible loss mechanisms in terms of similar electrical components. These mechanisms can be represented by their impedance values which are gained upon application of alternating current.

The applications of EIS in PEM fuel cell studies include the following [1]:

- (1) To provide microscopic information about the fuel cell system, which can then help in fuel cell structure optimization and the selection of the most appropriate operating conditions;
- (2) To allow modelling of the system with an appropriate equivalent circuit (EC), and consequently to obtain the electrochemical parameters of the system;
- (3) To differentiate the individual contributions of each component, such as the membrane and the gas diffusion electrode, to fuel cell performance, which can assist in identifying problems within the fuel cell components;
- (4) To identify individual contributions to the total impedance of a PEM fuel cell from different electrode processes such as interfacial charge transfer and mass transport in both the catalyst layer and the backing diffusion layer

I have used this test to specifically calculate the ohmic resistance. Also, start performing this test only after the system reaches equilibrium (it takes 15minutes for system to reach equilibrium).

To perform this test initial conditions were kept as follows:

- Cell temperature = 80 °C
- Anode humidifier temperature = 70 °C
- Cathode humidifier temperature = 70 °C
- Anode preheater temperature = 75 °C
- Cathode preheater temperature = 75 °C
- Current (main panel) = 1 A
- Flow rate of H₂/O₂ = 50 SCCM/100 SCCM

To perform this test, steps are as follows:

1. Watch the video file under the (EIS folder – Impedance)
2. According to literature, amplitude of input (current sinusoidal) wave is generally kept as 5% of the input DC current (for us, this is the current value shown in the main pane ‘station-1’) [1].
3. Ohmic resistance can be found by pulling the red line to the point where curve intersects x-axis (point near to origin, since its high frequency) [This is shown in the video EIS folder – Impedance, at time 19:00]
4. The value obtained above is R_{ohmic} . The intercept in Figure A.3 reflects the same ($R_{ohmic} = 0.285 \text{ k}\Omega \text{ cm}^2$)

3.) Stability – These tests are important to determine the life time of a cell and drop in performances with time. These tests were done to test the capability of the fuel cell test station to perform lengthy stability test in *In-situ* mode with

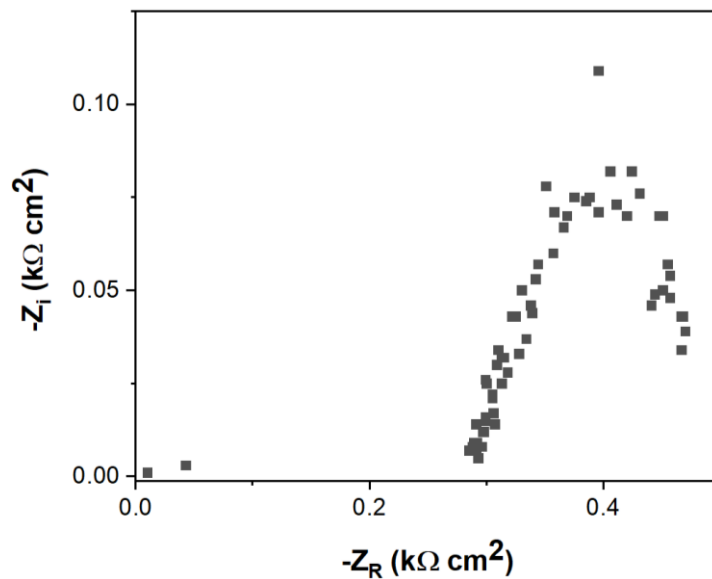


Figure A.3: Electrochemical Impedance spectroscopy (EIS) of an MEA in fuel cell test station

high pressure gases. However, because an old MEA was used as a trial, the results don't follow a particular trend.

Two types of stabilities were determined as per the DOE protocols – the first one was stability with humidity cycling, while the second one was performance evaluation of cell membrane under drive cycle load conditions.

- i. Humidity cycling (H_2 | N_2 @ 80^0 C) – Involves rapid change of the membrane environment via the change of the humidity. Because N_2 is used here on cathode side during potential cycles, the fuel cell is not in operating mode. This test is used to characterize the effect of rapid change of membrane environment on MEA performance (see Figure A.4).

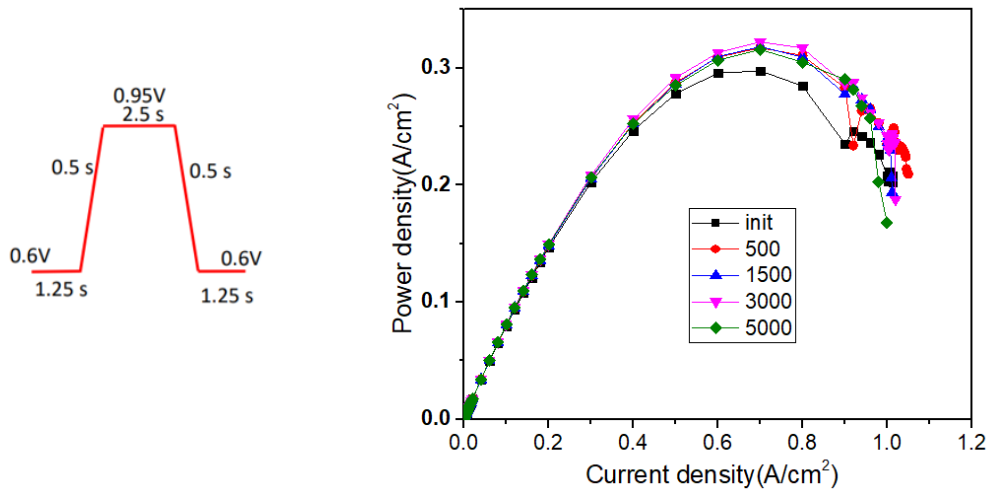
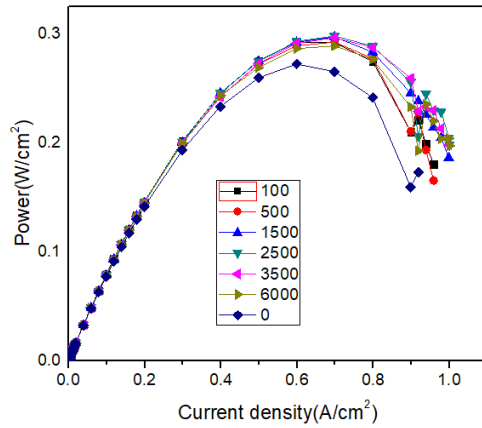


Figure A.4: Stability of an MEA for 5000 potential cycles in humidity cycling mode

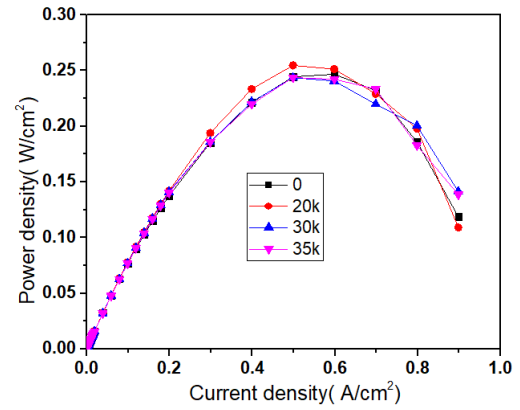
Polarization curves were generated after the specified cycles. The dwell point in the polarization curve for these curves is 1 minute.

- i. Load cycling (H_2 | O_2 @ 80^0 C) – The potential of the cell is rapidly changed to mimic startup and shutdown conditions of a fuel cell vehicle. As shown in Figure A.5, we could successfully run the fuel cell test station till 35k cycles

(with increased dwell time of 10 minutes), though we couldn't automate the load cycle and polarization curves measurement.



(a)



(b)

Figure A.5: Stability of an MEA for (a) 6000 potential cycles (b) 35000 potential cycles in load cycling mode

Appendix B: Inkjet printing of Ag nanowire network on plastic substrate with different bilayers of PEL coating:

In this section, we discuss the optimization of the polyelectrolyte bilayer coating from two different methods, the first one being shaking in Incubator and the second one is manually mixing. To avoid the costly Nafion substrate, these preliminary experiments were done on plastic substrate (OHP sheet).

B.1 Methodology -1: shaking in an incubator

In this experiment different bilayer coatings starting from 1 to 5 bilayers with varied loadings of 1mg, 2mg and 3mg of Ag each consisting of 2 samples is prepared.

Starting with the plasma cleaning process the samples are proceeded with PEL treatment for bilayer coating and the treated samples are left in the shaker for 10minutes as shown in Figure B.2. These steps are continued on for all 35 samples of OHP sheet (7 samples per batch equating to 5 batches i.e., 5 bilayers). Now to continue on the treated samples are struck on another OHP sheet and the printing process is proceeded with different Ag loading starting from 1mg, 2 mg and 3mg. The Print-Expose-Develop Process was continued further and the findings are as below.

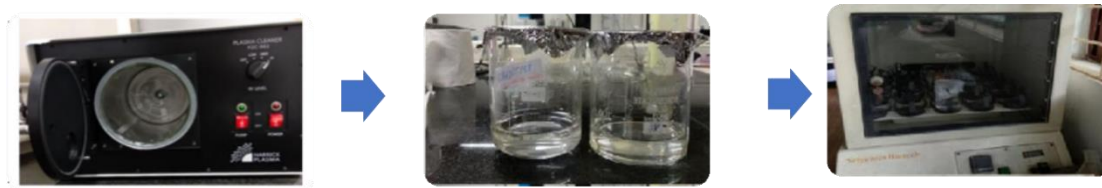


Figure B.2: Setup for bilayer with shaking incubator

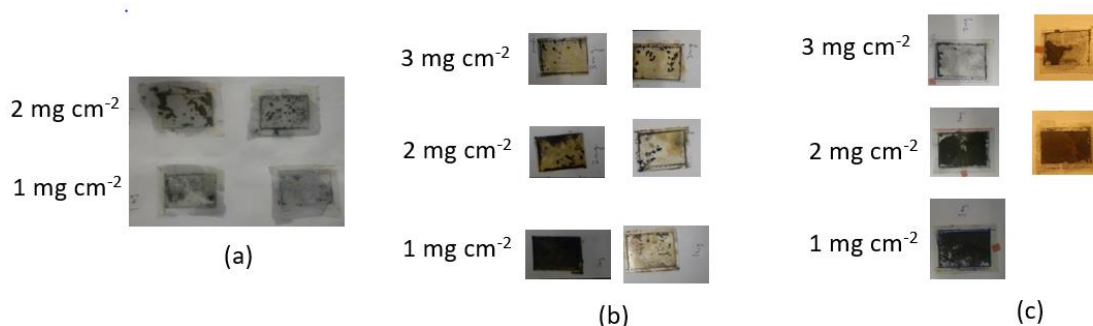


Figure B.1: Print-expose-develop samples on OHP sheet using methodology-1 for bilayer treatment (a) 1 bilayer (b) 2 bilayers (c) 3 bilayers. The images corresponding to 4 and 5 bilayers are not available due to inadvertent circumstances

From, Figure B.1 it can be seen that with shaking inside incubator, we couldn't get uniform conductive structures on the plastic substrate, leading to broken films of Ag. The sample loadings and contact angles were measured to find the cause of loss in uniformity (Figure B.3), which arose due to PEL coating has not been applied uniformly. The expectation of monotonic decrease in the contact angle couldn't be fulfilled, perhaps because the samples would have stacked one on top of each other, leading to inefficient coating of PEL bilayers. Though the methodology 1 works well for PEL coating for low Ag loading (1 mg cm^{-2}), it fails to deliver the similar effect for higher Ag loading (3 mg cm^{-2}).

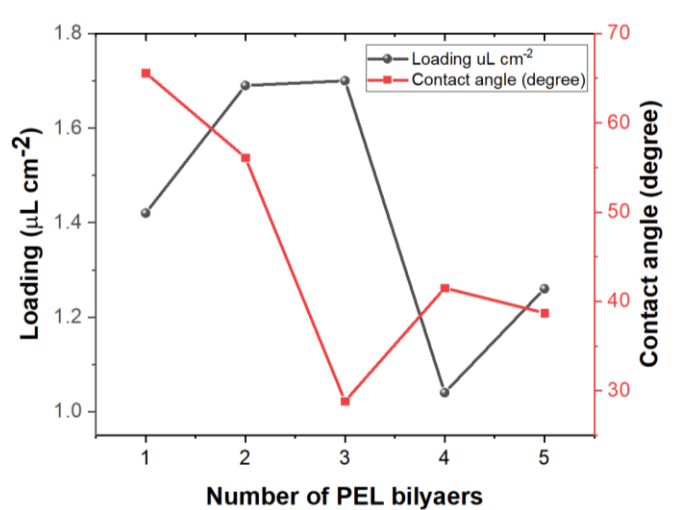


Figure B.3: Variation in loading and contact angle as a function of number of PEL bilayers with shaking in incubator for PEL bilayer deposition (methodology-1)

B.2 Methodology -2: Manual shaking

In this experiment different bilayer coatings starting from 1 to 5 bilayers with varied loadings of 1 mg cm^{-2} , 2 mg cm^{-2} and 3 mg cm^{-2} of Ag each consisting of two samples is prepared, same as before but the methodology adopted for coating is changed.



Figure B.4: PEL bilayer treatment process, with plasma cleaning, with manual shaking

After the plasma cleaning process, the samples were PEL treated to obtain different bilayers by the method shown in Figure B.4, where the trays were filled with PDDA and the petri dishes with PSS and the samples were dipped in these solutions 5 minutes each sides for even treatment. All 35 samples of OHP sheet (7 samples per batch equating to 5 batches i.e. 5 bilayers) can be treated in a single go unlike methodology 1. The rest of the steps were continued as before. The Print-Expose-Develop Process is continued.

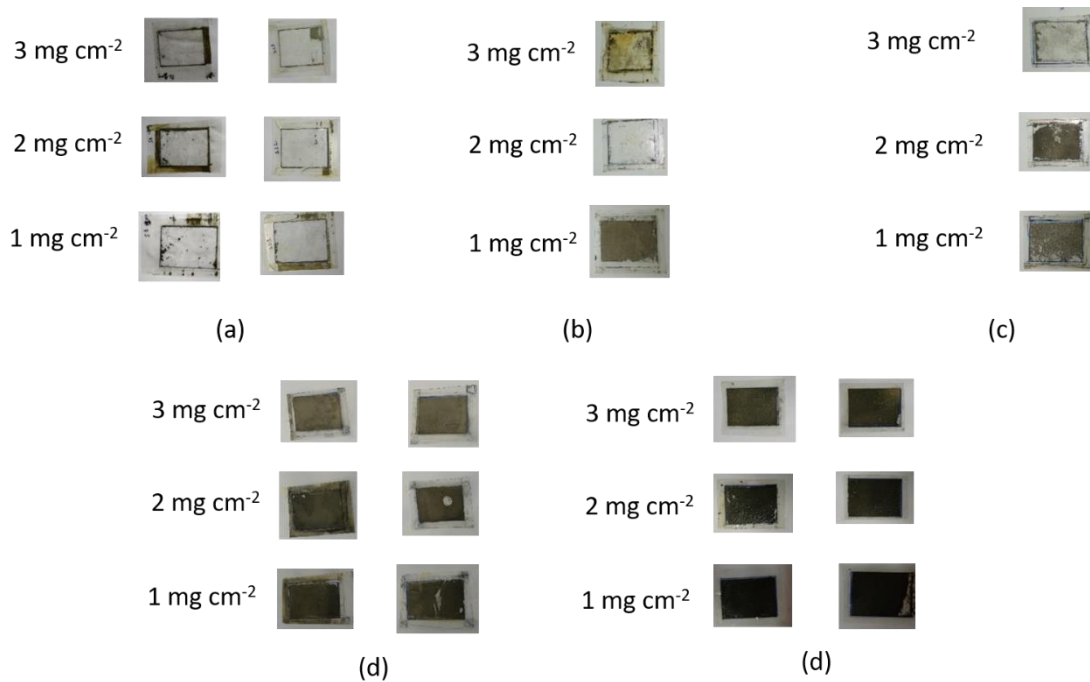


Figure B.5: Print-expose-develop samples on OHP sheet using methodology-2 for bilayer treatment (a) 1 bilayer (b) 2 bilayers (c) 3 bilayers (d) 4 bilayers (e) 5 bilayers

From, Figure B.5, it can be seen that there is a formation of uniform conductive structure for 3rd, 4th and 5th Bilayer. It is also apparent that at a higher loading for less PEL coated (less adhesive) surface it becomes prone to leaching. The samples were characterized for contact angle and loading for better

understanding. The contact angle in methodology-2 reduced monotonically with the increasing number of PEL bilayer treatment as shown in Figure B.6, while loading is also significantly high than the methodology-1, indicating better PEL treatment than methodology-1.

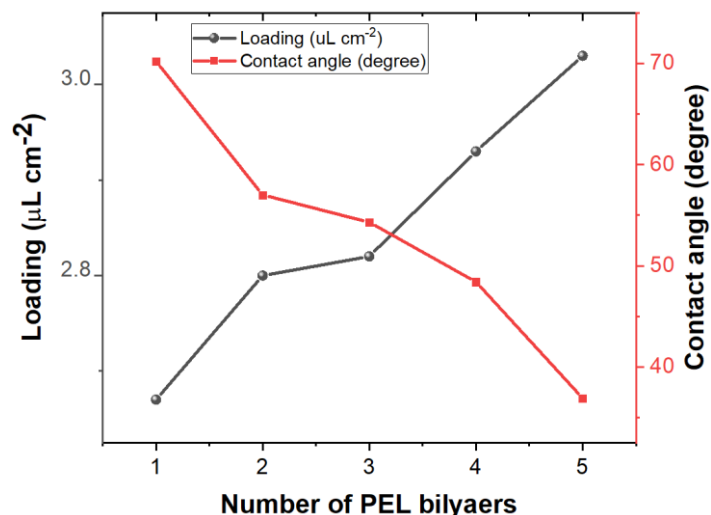


Figure B.6: Variation in loading and contact angle as a function of number of PEL bilayers with manual shaking for PEL bilayer deposition (methodology-2)

Essentially, we find PEL bilayer coating to be more uniform using methodology 2, than methodology 1. We also observed that a maximum loading of 3mg cm^{-2} leaches immediately if the adhesion was not good enough. So, to increase the loading, the bilayer coating has to be increased. Therefore, methodology-2 was adopted for PEL coating on Nafion membrane.

The optimum number of bilayers were determined by subjecting the developed silver nanostructured film to acid stability test with 3mg cm^{-2} silver loading and 3, 4 and 5 bilayers respectively. The samples were dipped for 1 hr in 0.1 M HClO_4 . The samples with 3 and 4 bilayers of PEL got leached with time, while

the sample with 5 bilayers sustained. Therefore, 5 bilayers with 3 mg cm^{-2} loading was chosen for conducting substrate for platinum deposition.